Tectonic Geomorphology and Paleoseismology of The Humps Fault Zone, North Culverden Basin

A thesis submitted in partial fulfilment of the requirements for the

Degree of Master of Science in Geology

By Thomas Brough

University of Canterbury

2019

Abstract

The November 2016 M_W 7.8 Kaikōura Earthquake initiated beneath the North Culverden basin on The Humps fault and propagated north-eastwards, rupturing at least 17 faults along a cumulative length of ~180 km. The geomorphic expression of The Humps Fault across the Emu Plains, along the NW margin of Culverden basin, comprises a series of near-parallel strands separated by up to 3 km across strike. The various strands strike east to east-northeast and have been projected to mainly dip steeply to the south in seismic data (~80°). In this area, the fault predominantly accommodates right-lateral slip, with uplift and subsidence confined to releasing and restraining bends and step-overs at a range of scales. The Kaikōura event ruptured pre-existing fault scarps along the Emu Plains, which had been partly identified prior to the earthquake.

Geomorphology and faulting expression of The Humps Fault on The Emu Plains was mapped, along with faulting related structures which did not rupture in the 2016 earthquake. Fault ruptures strands are combined into sections and the kinematic deformation of sections analysed to provide a moment tensor fault plane solution. This fault plane solution is consistent with the regional principal horizontal shortening direction (PHS) of ~115°, similar to seismic focal mechanism solutions of some of the nearby aftershocks of the Kaikōura earthquake, and similar to the adjacent Hope Fault.

To constrain the timing of paleoseismic events, a trench was excavated across the fault where it crossed a late Quaternary alluvial fan. Mapping of stratigraphy exposed in the trench walls, and dating of variably deformed strata, constrains the pre-historic earthquake event history at the trench site. The available data provides evidence for at least three paleo-earthquakes within the last 15.1 ka, with a possible fourth (penultimate) event. These events are estimated to have occurred at 7.7-10.3 ka, 10.3-14.8 ka, and one or more events that are older than ~15.1 ka. Some evidence suggests an additional penultimate event between 1850 C.E and 7.7 ka. Time-integrated slip-rates at three locations on the fault are measured using paleo-channels as piercing points. These sites give horizontal slip rates of 0.57 ± 0.1 mm/year, 0.49 ± 0.1 mm/year and one site constrains a minimum of between 0.1 - 0.4 mm/year. Two vertical slip-rates are calculated to be constrained to a maximum of 0.2 ± 0.02 mm/year at one site and between 0.02 and 0.1 mm/year at another site.

Prior to this study, The Humps fault had only been partially documented in reconnaissance level mapping in the district, and no previous paleoseismic or slip rate data had been reported. This project has provided a detailed fault zone tectonic geomorphic map and established new slip-rate and paleoseismic data. The results highlight that The Humps fault plays an important role in regional seismicity and in accommodating plate boundary deformation across the North Canterbury region.

Acknowledgements

Profuse thanks and gratitude must be given to the people of the district of Waiau, whose farms I have trod, and cups of tea I drank. Not a single gate was locked before me, every farmer and landowner welcomed me to help myself, and to let them know how much gold I had found. Despite what must be an especially difficult and trying time, the rural community shows its true form. Without access to the land, a geologist I am not. A huge thank-you to Don Mclean and his family for allowing me to trench his land, and his patience with infilling the result.

The McLean's trenching team of 2018 must be acknowledged, Dan Clark, Rob Langridge, Narges Khajavi, Kate Pedley, Andy Nicol, Jarg Pettinga and Tim Stahl. I owe much to Russ Van Dissen who kept me company in a muddy trench and taught me so much in a crash course of field trenching.

The earthquake response team that went out in the weeks following the earthquake produced a fantastic resource which is certain to continue to produce results, it is a dataset to be proud of, and invaluable in its breadth. A huge number of people went into its making from the department, thank you all. When I talked to those same landowners a year later after the earthquakes, it was the good relationships that you had left behind when you first visited those people that allowed me back onto the land.

Fieldwork is always uncertain and difficult, thanks to Janina Gillies, Dale Cusack and Tamiko Watson for accompanying me on the long drive to Waiau and the inevitable pie at Culverden. To office colleagues in 466, thanks for being there for me when I needed it.

Gratitude to my supervisory team; Jarg Pettinga and Tim Stahl, for taking time out of your busy lives and for your dedication.

Thank you to the EQC and GNS Science, who's funding made this MSc possible. The support lets us concentrate on the science.

Table of Contents

List of Figures

List of Tables

Chapter 1. Introduction and Literature Review

1.1 Background of the Kaikōura Earthquake

At 00:03am NZDT the 14th November 2016, the South Island of New Zealand was struck by a M_W 7.8 earthquake (Kaiser *et al*., 2017). The epicentre of the earthquake was located in rural North Canterbury and was characterised as an oblique thrust mechanism based on the Global Centroid Moment Tensor (Kaiser *et al*., 2017) (Fig 1.0). The earthquake initiated at a depth of 15 km, with the epicentre 4 km southwest of the small town of Waiau in North Canterbury. The surface rupture produced offsets up to 12 m laterally and 10 m vertically across a network of more than 20 crustal faults and along a total rupture length of approximately 180 km (Hamling *et al.,* 2017; Stirling *et al.,* 2017; Litchfield *et al.,* 2018; Langridge *et al*., 2018; Kearse *et al.,* 2018; Nicol *et al.,* 2018) (Fig. 1.0).

An estimated >10,000 landslides were triggered by ground shaking, rendering State Highway 1 and the main trunk rail line between Blenheim and Christchurch inoperable (Massey & Allstadt, 2018). Access to Kaikōura via state Highway 1 land routes was severed for several months after the event and recovery of the transport links is still ongoing. Building damage was recorded up to 200 km away from the epicentre in the Wellington region where liquefaction caused differential settlement of port facilities in Wellington Harbour (Cubrinovski *et al*., 2018). The estimated earthquake damage rebuild cost to transport infrastructure was $(2016)NZ 3 billion in addition to the residential and commercial estimate of $(2016)NZ 5 billion (Ministry of Transport, 2017).

The scale and damage of the Kaikōura earthquake has raised important questions regarding the specific nature of the faults involved; How have these faults behaved in the past? What did past ruptures on these faults look like, were they similar in magnitude and geometry, or was this one special? Where do these new faults fit into the active tectonics model of the South Island? These questions bear significant importance to the scientific community and the communities who live within the plate boundary.

1.2 Objectives of this Thesis

The large number and structural complexity of the faults ruptured makes the Kaikōura earthquake particularly significant for understanding how multi-fault earthquakes occur in New Zealand. The paleoseismic record of the faults involved could constrain how often a Kaikōura style event may have

occurred in the past, or whether it was a “one off” event. The faults south of the Hope Fault which ruptured during the Kaikōura earthquake, and in particular the hypocentral Humps fault (Fig. 1.0), do not have paleoseismic investigations published in the literature.

The paleoseismic results and slip-rate analysis from this thesis will provide some of first detailed rupture history from the faults involved in the southern ruptures. When ongoing paleoseismic studies conclude on other faults in the Southern Ruptures of the Kaikōura earthquake, the results will help refine its relationship within the region, and any co-interactions between these very closely linked faults (Fig. 1.0).

1.3 Structure of this thesis

This thesis is focused on providing a new, detailed paleoseismic record for The Humps fault, and therefore is organised with a straightforward structure. The remainder of Chapter 1 provides context and the geological background to the study area and Kaikōura earthquake. Chapter 2 investigates and documents the 2016 surface rupture morphology of The Humps Fault on the Emu Plains, within the context of geomorphological mapping. Chapter 3 investigates the paleoseismicity and slip-rate at selected sites on The Humps Fault, using material derived from Chapter 2 as a guide. This streamlined structure is justified in that the material in Chapter 3 is proposed as a standalone piece of work, with planned submission for peer reviewed publication within the next year. The remainder of this chapter will briefly outline general geologic background for Chapters 2 and 3.

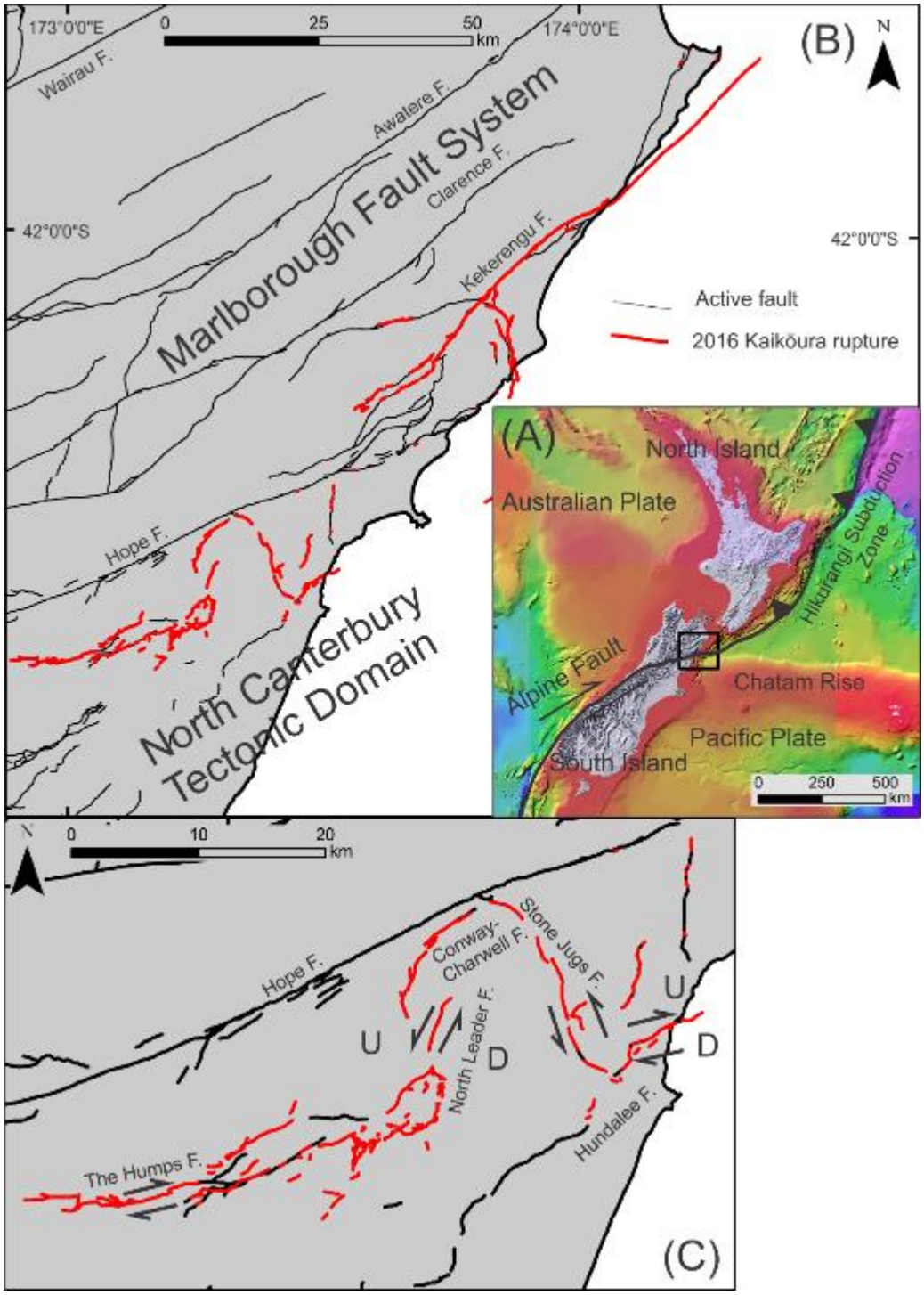

Figure 1.0: 2016 Kaikōura Earthquake setting and ruptures. (A) The location of the earthquake (black square) relative to the plate boundary in New Zealand. (B) Expanded view of all surface ruptures produced by the Kaikōura earthquake. Active faults sourced from New Zealand Active Faults Database (Langridge, 2016), 2016 Kaikōura Earthquake fault ruptures in red from (Litchfield, 2018).

1.4 Tectonic setting of the Kaikōura earthquake

New Zealand straddles the obliquely-convergent Australia-Pacific plate boundary. The northern sector is characterised by subduction of the 15 – 23 km thick (Timm *et al.* 2014) oceanic plate beneath the continental crust of the North Island along the Hikurangi subduction margin (Holt & Haines, 1995; Barnes *et al*., 1998; Pondard & Barnes, 2010; Wallace *et al*., 2012). Further south, the oceanic crust transitions to the thin (23-26 km) continental crust of the Chatham Rise; here, the oblique convergence of continental crust produces the uplift of the Southern Alps of New Zealand within the central South Island. The North Canterbury Tectonic Domain (NCD) straddles the transitional zone between plate subduction occurring in the North, to the oblique continental collision of the Southern Alps (Litchfield 2014). This transitional zone in the NCD is characterised by crustal shortening and thickening accommodated primarily through NE-SW striking dextral reverse faults with associated asymmetrical folding (Pettinga *et al.* 2001, Cox *et al.,* 2012). Several of these north-easterly striking faults within the NCD have been interpreted as reactivated Cretaceous normal faults (Nicol & Wise 1992, Nicol 1993). This reactivation of the North Canterbury faults has occurred relatively recently, within the last 1 Ma, as a response to a southward migration of the plate boundary deformation zone (Nicol *et al*., 1994, Pettinga *et al*., 2001).

Geologic slip rates of faults within the NCD in the vicinity of the Kaikōura earthquake sequence have been estimated between 0.1 - 0.6 mm/yr. with the majority of faults in the area having return periods in the range of 1 – 10 ka (Cowan 1990; Armstrong 2000; Pettinga *et al.,* 2001; Rattenbury 2006; Barrell & Townsend 2012). Because of the relatively lengthy recurrence periods on the faults in this domain, several faults that ruptured in the Kaikōura earthquake were previously unknown or poorly characterised.

To the north of the NCD lies the Marlborough Fault System (MFS), which comprises a series of parallel dextral faults. These faults include (from south to north) the Hope Fault, the Jordan-Kekerengu Fault, the Clarence Fault, the Awatere fault and the Wairau Fault. Late Quaternary slip-rates within the MFS range from 3.4 mm/yr. on the Wairau fault up to 23± 4 mm/yr. (Langridge et al. 2003) on the Hope Fault.

1.5 Surface rupture characteristics of the Kaikōura earthquake

The 2016 Mw 7.8 Kaikōura earthquake initiated beneath the North Culverden Basin, within the NCD on The Humps Fault (Fig. 1.0). The Humps Fault is a primarily dextral E-W striking fault, with a series of stepovers and linking sinistral-slip segments (Chapter 2). Moving towards the northeast, The Humps

Fault appears to have transferred motion onto the Leader Fault (Nicol *et al.* 2018), which strikes N-S, producing predominantly reverse-sisnistral displacements, inducing uplift on the Mt. Stewart range (Nicol *et al.* 2018). The rupture propagated onto the Conway-Charwell, Stone Jug and the Hundalee Faults within the NCD (Fig. 1.0). A small section of the Hope Fault ruptured, triggering a 30 cm thrust wedge on the seaward section of the fault on the Kaikōura Plain. Fault ruptures within the NCD can be characterised as a complex array of dextral to oblique reverse slip movements, segmented by bends, gaps and step-overs. North of the Hope Fault, within the MFS, fault displacements are much higher, with net displacements of up to approximately 12 m on the Kekerengu Fault (e.g., Kearse et al., 2018; Langridge et al., 2018; Litchfield et al., 2018).

1.6 The Humps Fault

The Humps Fault was the hypocentral fault of the Kaikōura earthquake and was the southernmost structure that ruptured during the event (Nicol *et al.* 2018). The fault measures 36 km in length from a free tip in the west to where it meets the Leader Fault in the east (Fig. 1.0). The fault passes through The Emu Plains, an area of extensive Late Quaternary alluvial fans, before continuing into the Mt. Stewart Range. The fault ranges in strike from approximately 090° to 050° and dips steeply to the south at 80° (Nicol *et al.* 2018). The fault displayed primarily right lateral strike slip with a reverse component. Cumulative horizontal displacements of up to 4 ± 0.3 m and vertical displacements of up to 3.5 ± 0.5 m were recorded following the 2016 earthquake (Nicol *et al.* 2018). Vertical and horizontal displacements generally increase towards the east along the fault.

1.7 Previous work

Geological work focussed within the North Culverden Basin began with Buchannan (1868) and his early exploration of North Canterbury. Authors contributing to the understanding of the area include Speight (1918), Mason (1949), Wilson (1963), Gregg (1965) and Clayton (1968). Due perhaps in part to the lower slip-rate of faults in the NCD relative to the MFS, few active fault studies were conducted in North Canterbury prior to the 1980s. Notable exceptions to this, as well as recent active faulting studies in the vicinity of the North Culverden Basin have focussed on the Hope Fault, the major structure in the area (Fig. 1.0) (e.g. Mckay 1888; Freund 1971; Cowan 1989; McMorran 1991; Khajavi *et al.*, 2018). Studies on active faults in the basin itself include Mould (1992) Armstrong (2000) and Noble (2011).

The Humps Fault was first described and named by Barrell and Townsend (2012) as part of a reconnaissance report of active faults within the Hurunui region of North Canterbury. This report

identified The Humps Fault as having a total length of 15 km (2 km mapped as 'definite' and 13 km as 'possibly active') based on air-photo interpretation of deformed river terraces. The estimated vertical slip-rate was given as 0.2 mm/yr., and a recurrence interval was estimated at 13 ka (Barrell and Townsend 2012).

After the Kaikōura earthquake of November 2016, a large group of researchers led by the University of Canterbury spent several weeks documenting and measuring offsets on The Humps Fault and other faults involved in the southern ruptures of the earthquake. The results of the work contributed to the current understanding of the fault, its offsets and structure, and are summarised in Nicol *et al.* (2018).

Chapter 2: Structural style and geomorphic expression of faulting on The Humps Fault.

2.1 Introduction

Surface rupture records from paleoseismic site investigations must be founded on a general understanding of the Quaternary geology. This chapter will examine the near-surface structure of The Humps Fault and the geomorphology of the Emu Plains. In doing so, it will achieve the following objectives:

- Map the geomorphology of the Emu Plains, including fault scarps of The Humps Fault
- Determine and summarise the evidence for a past earthquakes on The Humps Fault from its surface expression
- Discuss the evidence and potential causes for variable surface rupture patterns on The Humps Fault

The Humps Fault within the Emu Plains can be divided into sections (Fig, 2.0) which can be demarcated based on their geometry, geomorphic expression across late Quaternary geomorphic surface, and displacements. Nicol *et al.* (2018) delineates five separate sections of fault on The Humps Fault within the Emu Plains area. In this study, a further zone is added between sections 1 and 2 of Nicol *et al.* (2018) as well as other areas of the fault which did not rupture during the 2016 earthquake. The remainder of this chapter discusses the various late Quaternary surfaces of the Emu Plains and each of these fault sections individually.

2.2 Methods

2.2.1 Fault mapping

I used a multi-disciplinary approach to mapping the tectonic geomorphology of the Humps Fault and Emu Plains. Mapping was conducted using pre- and post-earthquake LiDAR interpretation, pre-earthquake aerial photography, and field-based mapping.

Post-earthquake LiDAR was sourced from a Land Information New Zealand (LINZ) commissioned fixed-wing LiDAR survey. The survey was flown between the 3rd of December 2016 and the 6th of January 2017 which took in all fault ruptures associated with the Kaikōura Earthquake. The initial point cloud had an average shot point density of 10.1 m^{-2} and was processed into a Digital Elevation Model (DEM) with a 1 m^2 resolution. Pre-earthquake LiDAR was flown in May 2012 for Environment Canterbury

Regional Council (ECAN) with an average shot point density of 1.24 m^{-2} and was reprocessed into a 1 m^2 DEM. Pre-earthquake aerial imagery was commissioned by Environment Canterbury at a 0.75 m resolution during 2004 – 2010 with a final spatial accuracy of ± 3 m. Historical black and white aerial photos also aided in identification of potential anthropogenic modification of geomorphic features. These images are sourced from NZ Aerial Mapping Ltd and were acquired under Government contract in August 1950. The image set includes reference line 1801 numbers 19-36.

Differential LiDAR was produced by subtracting the 2013 ECAN DEM from the 2016 LINZ DEM for available overlapping areas. The resulting model indicates vertical displacement of topography but cannot track changes in horizontal displacement. This results in horizontal displacement of pre-existing vertical topography appearing as vertical displacement. For instance, terrace edges which were not displaced vertically during the earthquake, appear in the differential images to have been vertically displaced depending on their aspect and sense of slip experienced (e.g., a stream bank facing east, being displaced to toward the east, appears as a net positive vertical displacement in the differential images). Despite this shortcoming, differential images revealed centimetre-scale vertical displacements faults.

Field mapping and surveying of faults were conducted in the weeks following the 2016 Kaikōura earthquake by a team of geologists including staff and students from the University of Canterbury. The group mapped fault ruptures south of the Hope Fault as part of a collaborative response effort with GNS and other New Zealand universities to document the earthquake. Data on fault displacements, orientations and field interpretations have been used in this thesis. Additional field mapping was conducted for this thesis in 2018 to confirm surface ruptures and features identified in LiDAR and aerial photos. Field mapping was conducted at a scale of 1:10,000.

Fault displacement data was collected on offset cultural features which primarily included fence lines, roads, farm tracks, buildings and cropping lines. Offsets were measured with tape measure and locations recorded with handheld GPS units. Uncertainty estimations were made in the field and are generally recorded at < ± 20%. Field photographs and selected site locations are mapped in figure 2.0.

2.2.2 Quaternary geology and geomorphological mapping

Quaternary deposits within the Emu Plains were first mapped by Gregg (1965), with the interpretations becoming the base of the QMAP in the region. Gregg (1965) used the NZ Aerial Mapping Ltd 1950 black and white aerial photographs to propose the boundaries of 3 quaternary cover units (Table 2.0).

Clayton (1968) built on the work of Gregg (1965) using elevation calculation methods (aneroid barometer) to compare relative heights of river terraces in the Waiau area in elevational profiles, with an error margin of tens of meters. Clayton presented 4 units within the area (Table 2.0).

Toward the primary objective of characterising fault traces and their paleoseismology, I propose seven distinct stratigraphic groupings for alluvial surfaces on the Emu Plains (Table 2.1). These surfaces are correlated across the field area using high resolution contour maps derived from the 2016 LINZ LiDAR dataset and defined by significant differences in local relief, changes in surface morphology and changes in surface aspect.

Surfaces of equivalent elevation and morphology, and thus relative age, are given a sub-letter e.g. S3a, S3b to distinguish independent catchment areas. For instance, in the western section of the Emu Plains, where very wide (between 2-4 km) S4 fans interfinger with each other seamlessly, fans show very similar surface morphology; however, these fans can be traced to different catchments in the Amuri Ranges (Fig. 2.0), therefore have an inferred equivalent age, but are distinct surfaces from a geomorphic standpoint.

Table 2.1: Comparison of previous studies surface naming conventions and stratigraphic order on the Emu Plains. Q-Map ages from Rattenbury *et al.* (2006)

Surface in this study	Gregg (1965)	Clayton (1968)	Q-MAP
S1	Woodlands Fmtn	Not covered	Q6a
S2	Hororata Fmtn	Bluffs	Q6a
S3	Woodlands Fmtn	Te Mara	Q4a
S4	Woodlands Fmtn	Te Mara	Q2a
S5	Burnham Fmtn	Post-Leslie Hills	Q1a
S6	Burnham Fmtn	Bewdley	Q1a
S7	Burnham Fmtn	Post-Leslie Hills	Q1a

The boundaries and stratigraphic order of units in this study do not significantly differ from previous work. However more units can be differentiated due to the increased resolution of aerial imagery and topographical data (i.e. LiDAR).

2.3 Geomorphology and fault mapping results

Surfaces S1, S4 and S5 are interpreted to be alluvial fans sourced directly from the Amuri Ranges above the Emu Plain to the north (Fig. 2.0). The S1 fans are characteristically heavily eroded and exhibit dendritic channelization throughout their surfaces. They show an eroded edge to the fan surface and are prominently higher on the plains than other surfaces, relative to local stream levels. S4 fans make up the largest area of the eastern Emu Plains, with large interlocking fans and relatively smooth surfaces compared to the S1 surface. The S5 surface sits above the S4 surface but has an even and poorly demarcated transition onto the S4 surface compared to the S1 fans. Its morphology has a smoother surface, with little sign of erosion and has been interpreted as being deposited atop the S4 surface.

Surfaces S2, S3, S6 and S7 are interpreted to be sourced from the Mason and Lottery Rivers. The S2 surface sits the highest above the confluence of the two rivers and can be regarded as the oldest surface in the eastern Emu Plains but is not as heavily dissected as the S1 surface in the west. The S3 surface sits above the modern Lottery and Mason Rivers, which have incised younger cut-in-fill terraces into the aggradational surface (Fig 2.0). Paleochannels on the S3 surface are readily visible on the surface in LiDAR, and in places fault offsets can be seen across these channels (Fig. 2.0). The S3 surface is much higher than the S4 surface, with Dog Brook separating the two (Fig. 2.0). Remnants of the S3 surface can be correlated across Dog Brook with the S4 surface lying below it, which implies an older stratigraphic age for S3 than S4. At the Lottery River, S6 sits below S3, and is only 2 m above the river in places. S7 is the lowest surface above the Mason River, situated less than 1 m above the active floodplain in some places.

Based on this mapping, the surfaces of the Emu Plains largely comprise a suite of basin fill ranging from alluvial fans, to aggradational river terraces, with some degradational cut-in-fill and strath terraces near streams. The western fans of the plains (S1, S4, and S5) have material directly eroded from the Amuri Range, which consists primarily of the Cretaceous well bedded sandstone-mudstone Pahau terrane (Rattenbury *et al.* 2006). Locally within these fans, material may be derived from the outcropping remnants in the Amuri Ranges of the basaltic pillow lavas of the Cookson's Volcanics Group, and the calcareous silty mudstone of the Waima Formation (Gregg 1965, Rattenbury *et al.* 2006).

Geomorphologic and 2016 Surface Rupture Map of The Humps Fault within the Emu Plains

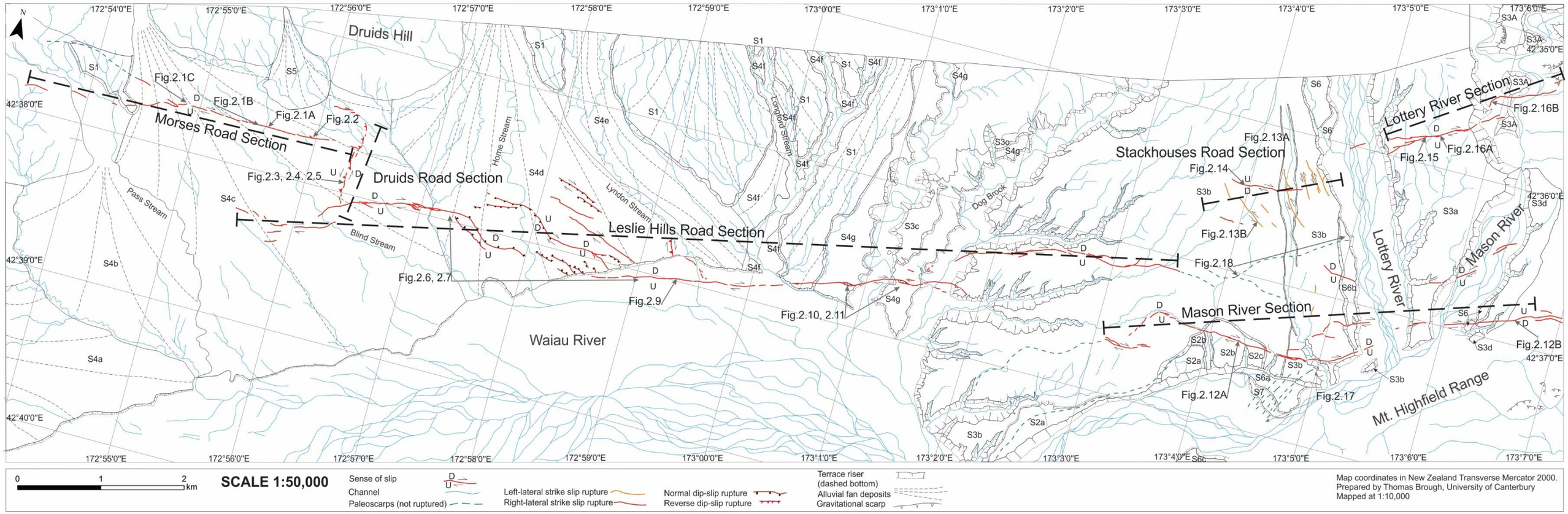

Figure 2.0: Map of geomorphic surfaces and The Humps Fault rupture expressions on the Emu Plains. Figure locations and fault sections for Chapter 2 are indicated as shown.

2.3.1 Morses Road Section

The Morses Road section of The Humps Fault begins in the foothills of the Amuri Range and is the westernmost expression of the fault rupture expression (2.0). In 2016, this 4.1 km section of fault produced a right-lateral strike slip rupture, with an average strike of 088°. On-fault displacements ranged from 0.1 m right-lateral strike-slip on the western tip, to 1 m on the eastern most end. Vertical displacements on the section ranged between 0 - 0.2 m of displacement. In the field, surface deformation is expressed as a single, predominantly continuous trace with little deviation in strike or sense of slip (Fig. 2.1). Within the easternmost strand of the fault section, the fault is expressed in small valleys as a south dipping fault plane. Approximately 2.5 km east of the Morses section boundary in the west, a 300 m long right lateral splay meets the fault, striking at 095° (Fig. 2.0). The 2016 earthquake on this section of the fault ruptured through the S4 and S1 surface of figure 2.0.

Prior to the 2016 rupture, aerial photography provides only ambiguous evidence for pre-existing fault scarps. Small lineaments are visible in pre-earthquake Environment Canterbury imagery, revealed as changes in vegetation density (Fig. 2.2). Pre-earthquake LiDAR is not available for this section, which limits the identification of the morphology of the fault prior to 2016.

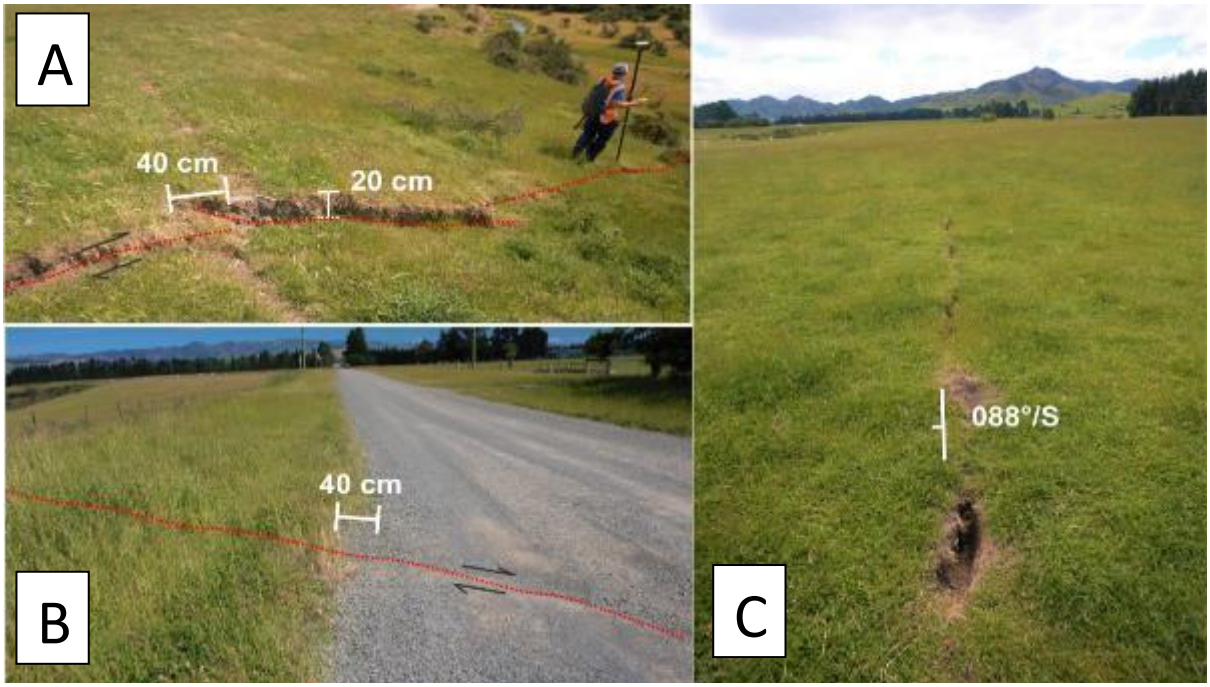

Figure 2.1: Surface ruptures of the Morses Road section, showing variable vertical displacements. Locations on figure X.XX (A) fault scarp entering a stream cut riser. (B) Right lateral displacement of Morses Road, with sub centimetre vertical displacement. (C) Typical linear rupture expression, with a small vertical component and extensional gashes along the fault trace. Photographs courtesy of Kate Pedley.

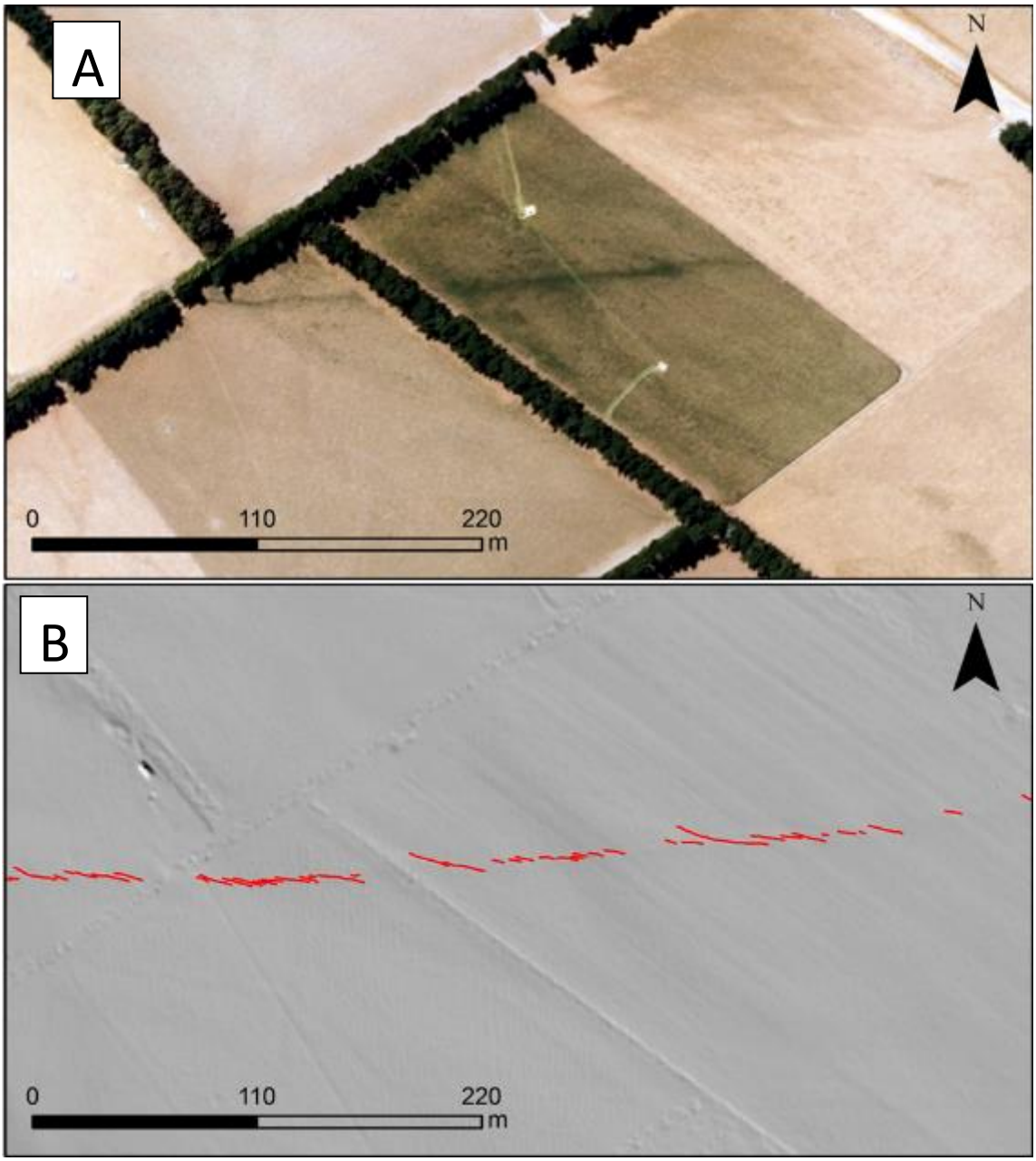

Figure 2.2: A pre-existing fault trace on the Morses Road section, revealed by a difference in grass density and health, possibly due to a varying soil depth across the fault. (A) Pre-earthquake aerial photograph, taken by Environment Canterbury between 2004 - 2010 with an apparent fault trace centred. (B) LiDAR hillshade image of the same extent as above, taken post-earthquake with the fault rupture highlighted in red.

2.3.2 Druids Road Section

The Druids Road section is distinguished by its near right angle to the Leslie Hills Road and Morses Road sections, striking at 175°/W (Fig. 2.0). The section runs a kilometre in length and accommodated left-lateral reverse slip during the 2016 earthquake (Fig. 2.3). Horizontal and vertical displacements ranged from 0.20 to 0.45 m (Fig. 2.4) and between 0.3 and 0.4 m respectively. The 2016 rupture is characterised by 20 m-long right-stepping reverse fault traces, themselves made up of right stepping Riedel shears (Fig. 2.3). The Druids Road section is fully contained within the S4c fan of the Emu Plains (see Fig. 2.0).

A pre-existing fold scarp of 1.1 m existed on the trace of the 2016 ruptures (Fig. 2.5). The fold scarp in the 2013 ECAN LiDAR is up to 50 m wide in places (Fig. 2.4, 2.5), which may explain why it was not resolved prior to 2016.

Figure 2.3: Surfaces ruptures of the Druids Road section. (A) Right stepping Riedel shears (white dotted lines) within the fault, looking north. (B) Left-lateral offset on a fence on the section. Photographs courtesy of Kate Pedley.

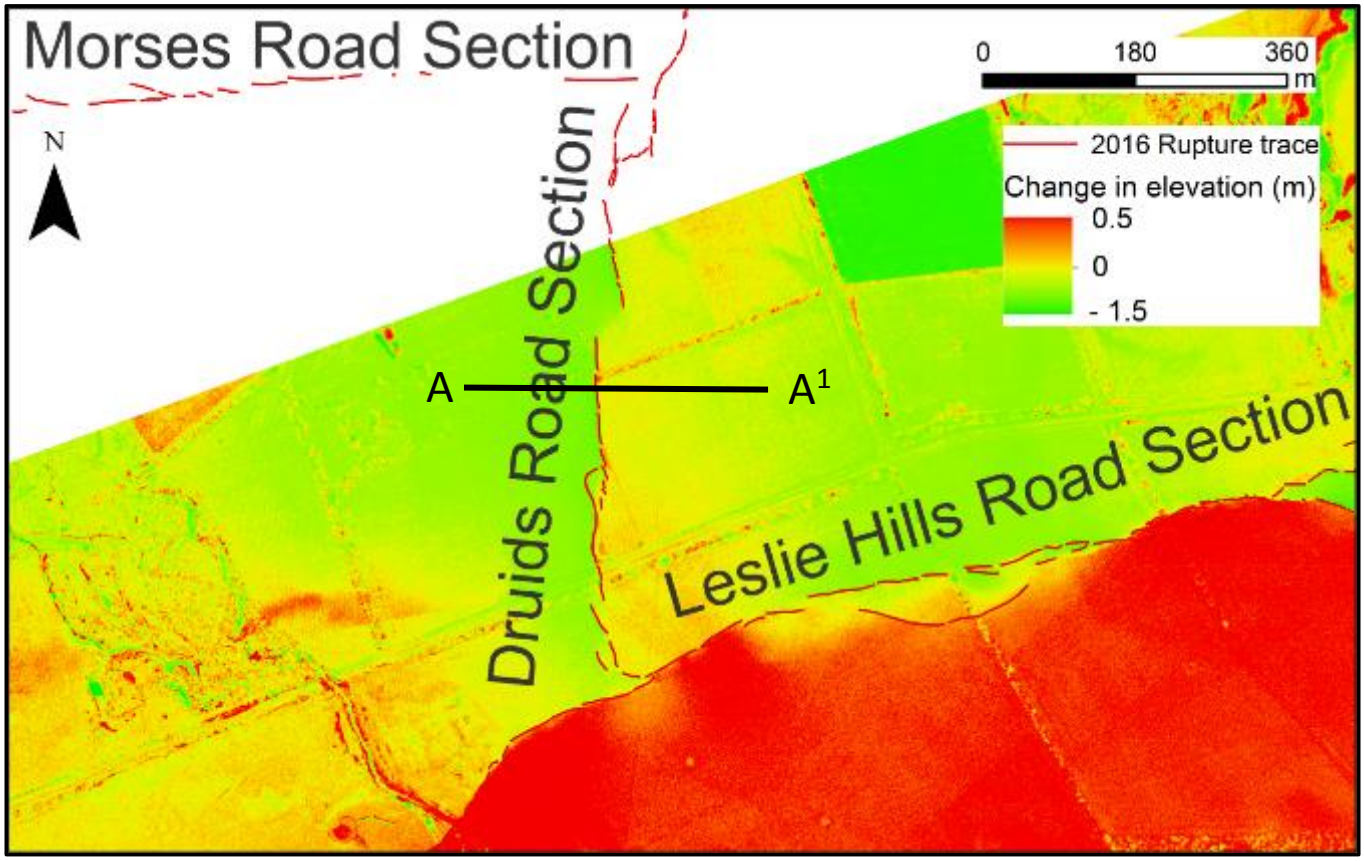

Figure 2.4: Differential LiDAR image of the Druids Road section, showing the vertical displacement interaction between the Druids Road section and the Leslie Hills Road section of fault. Transect from A- A1 indicates extent of the transect in Figure 2.5.

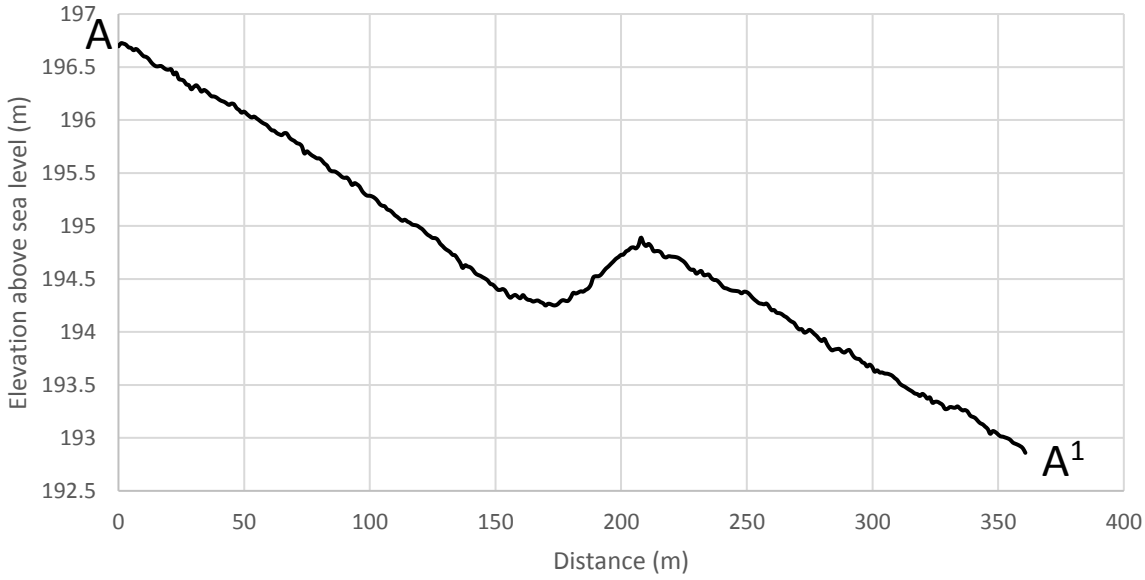

Figure 2.5: Cross-section of topography taken from the 2013 ECAN LiDAR, showing a pre-existing fault scarp on the Druids Road fault section. Location of the transect is shown on Figure 2.4.

2.3.4 Leslie Hills Road Section

The central and longest section of The Humps Fault within the Emu Plains, the 11 km Leslie Hills Road section is a predominantly right-lateral fault with an average strike of 077° (Fig. 2.0). Displacements were highly variable over the section in the 2016 earthquake, with right-lateral displacements ranging from 0.6 to 2 m, and vertical displacements between 0 – 2 m. Styles of deformation along the section were varied: the section begins in the east with several disconnected parallel strands and becomes a single strand near the Druids Road section intersection. The section ruptured over three different surfaces on the Emu Plains; S4, S3 and the modern floodplain of the Waiau River (Fig. 2.0).

A major structural feature, here named the Home Stream stepover, sits 3 km from the western end of the fault section (Fig. 2.0). The feature is a releasing stepover bounded by normal faults with a length of 2 km and width of 500 m (Fig. 2.6). The structure represents a right stepover of 500 m between two splays of the Leslie Hills Road section, with the orientations of the splays change from a strike of 088° west of the stepover to a strike of 075° east of the stepover (Fig. 2.6). The majority of displacement is contained between two faults of the stepover, however to the north of the stepover, several parallel strike slip faults up to 650 m away also carry right lateral displacement and a small vertical component (Fig. 2.7). In contrast, the fault displacement on the south of the main fault trace of the stepover is much more compact, with a single subsidiary rupture 100 m away from the primary trace (Fig. 2.7).

Pre-2016 fault scarps can clearly be seen in LiDAR and aerial photography within the Home Stream stepover. When compared to the surface ruptures produced by the 2016 earthquake, the surface ruptures and pre-existing scarps are almost identical, with the 2016 surface rupture re-rupturing the majority of fault scarps present in 2013 (Fig. 2.6). These surface ruptures have produced normal faults within the stepover to accommodate extension (Fig. 2.8).

East of the Home Stream Stepover, the section leaves the S4 surface of the Emu Plains and crosses over what is interpreted to be the modern floodplain of the Waiau River (Fig. 2.0). Within the floodplain, the fault produced large scale liquefaction and ponding on the fault rupture, with a large length of the Leslie Hills Road rendered inaccessible (Fig. 2.9). The floodplain does not reveal any evidence of a pre-existing scarp on the 2013 ECAN LiDAR.

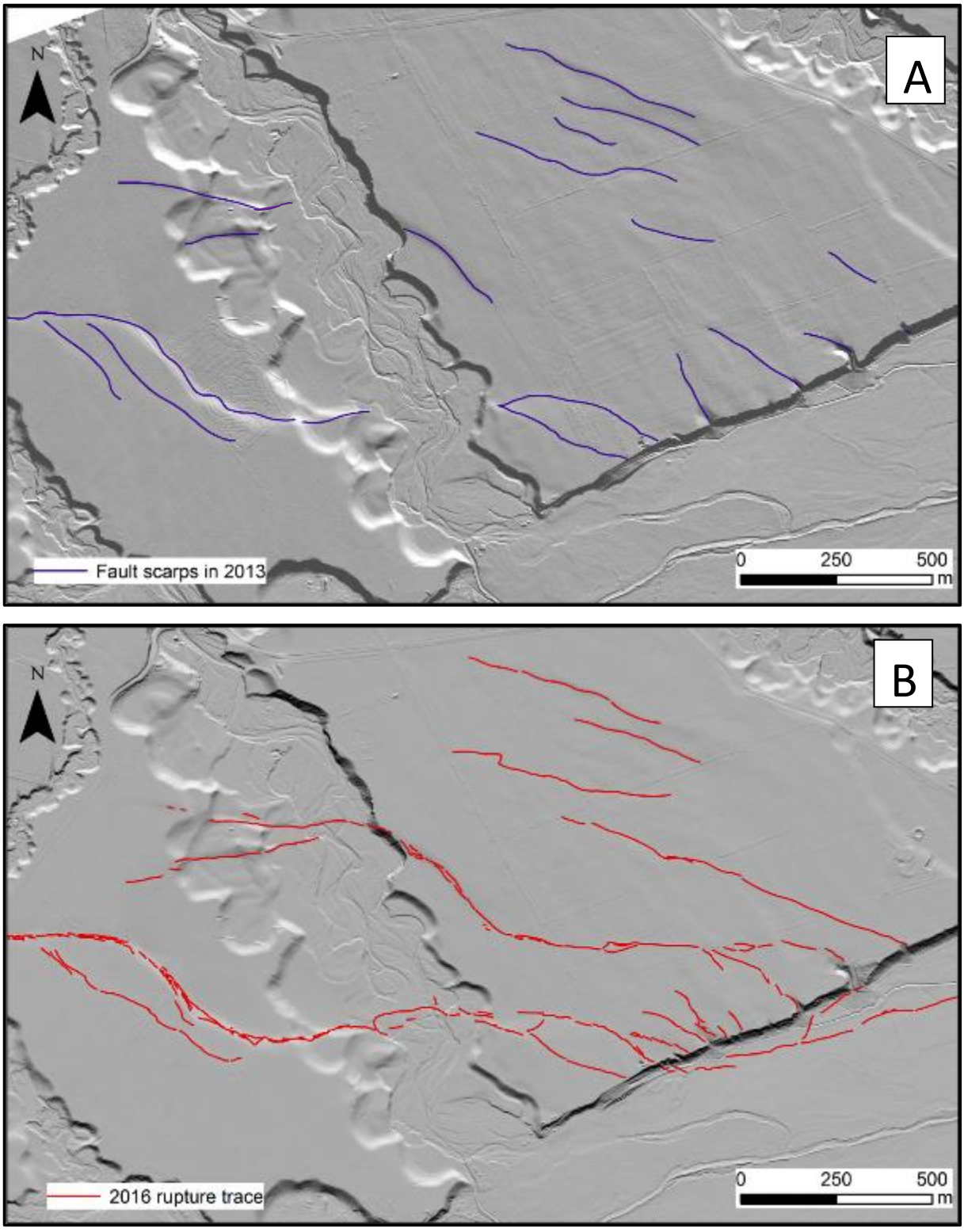

Figure 2.6: Hillshade images of the Home Stream stepover, where the 2016 rupture re-occupied a significant portion of the pre-existing fault scarp. (A) Pre-earthquake hillshade with visible fault scarps interpreted in blue. (B) Post-earthquake hillshade image of the same area, with fault ruptures annotated in red.

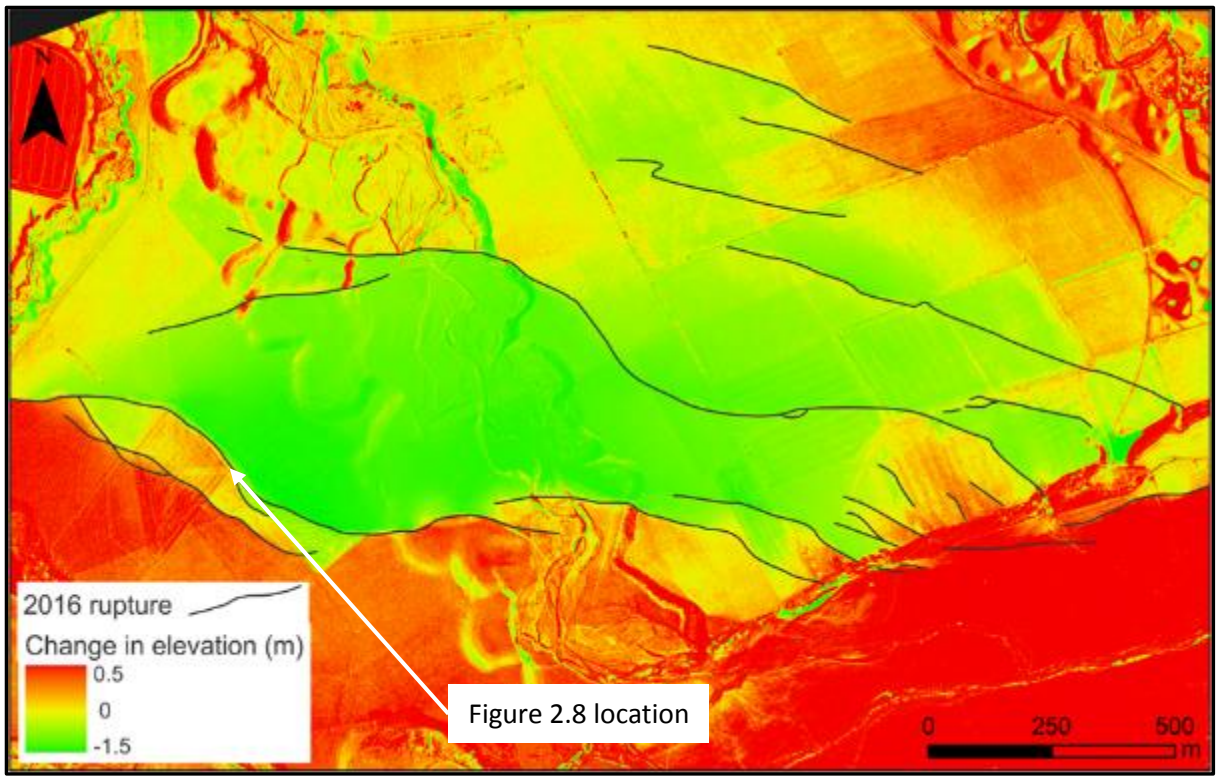

Figure 2.7: Differential LiDAR raster of the Home Stream stepover, with the heat map indicating vertical displacement. Displacement is widely spread to the north of the fault zone (up to 600m from the main displacement ruptures), while south of the fault zone displacement is tightly controlled.

Figure 2.8: Normal faulting on the Home Stream Stepover, accommodating an accumulative 1.5 m of vertical deformation on a well-established fault scarp. Location shown in figure 2.7.

Figure 2.9: Surface rupture on the Leslie Hills Road section. (A) Liquefaction and rafting of Leslie Hills Road. (B) Right Lateral offset of Leslie Hills Road and ponding in the paddock nearby against the fault rupture. Photographs courtesy of Kate Pedley.

Where the section exits the floodplain of the Waiau River, the fault re-crosses the S4 surface of the Emu Plains (Fig. 2.0). Pre-existing fault scarps here are much higher here than elsewhere on the section, some with up to 5 m in relief. Two prominent sag ponds lie on this splay of the fault (Fig. 2.10), with the fault stepping to the right on both sag ponds to form structural depressions, much in a similar fashion to the Home Stream Stepover. In these depressions, up to 1.5 m of negative vertical displacement occurred in the 2016 ruptures (Fig. 2.10). These sag ponds are highly visible in pre-earthquake LiDAR, with the 2016 rupture closely matching the pre-existing fault scarp geometry (Fig. 2.11).

Where the fault re-enters the S4 surface, single point horizontal displacements are among the highest recorded in the Emu Plains, at between 1.8 – 2 m. The fault branches at Dog Brook and enters an older surface S3, running for 700 m before becoming indistinct, after which the main trace steps 300 m to the northwest, normal to the fault's strike (077°) (Fig. 2.0). Along this northern segment, horizontal displacements reduce to around 0.35 m and progressively reduce in magnitude until the fault becomes indistinct.

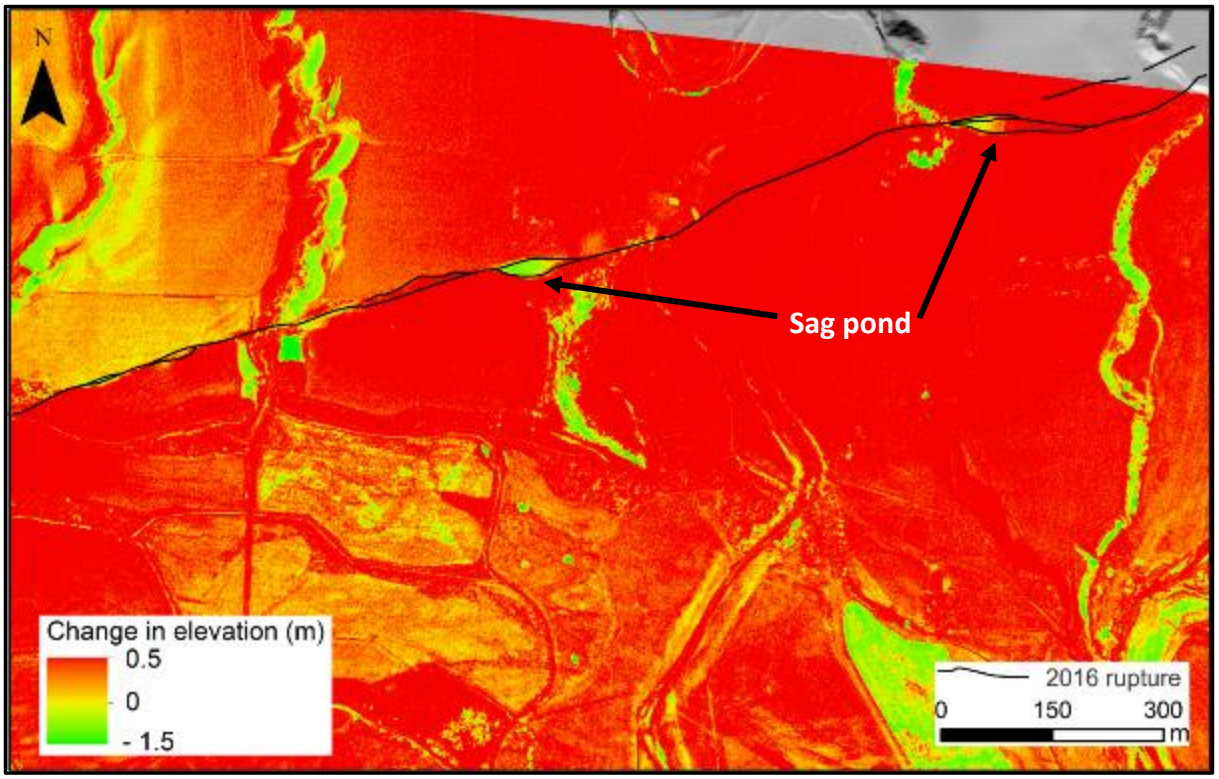

Figure 2.10: Differential LiDAR image of a central strand of the Leslie Hills Road section showing the vertical displacements of the ground surface. Sag ponds bounded by faults experienced up to 1.5 m of negative vertical displacement during the 2016 earthquake. Note artefacts of apparent negative (green) displacement on terrace risers orientated north-south, an effect caused by the horizontal translation of topography.

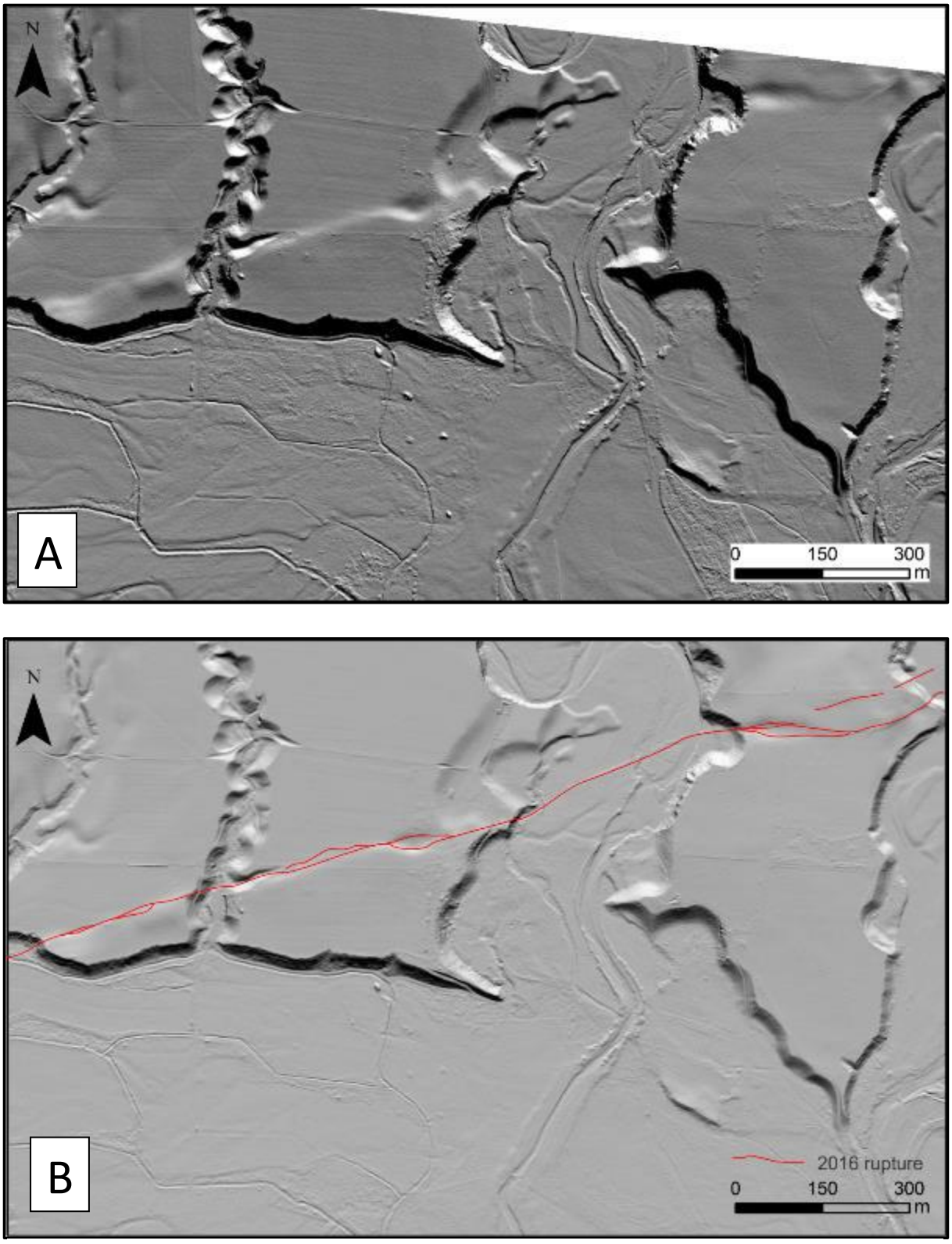

Figure 2.11: Small sag ponds within the Leslie Hills Road section. (A) Pre-earthquake hillshade image of the fault section taken in 2013. (B) Post earthquake hillshade image of the same section of fault, with fault rupture marked. The 2016 rupture has re-occupied the pre-2016 fault scarp with a high degree of precision.

2.3.5 Mason Section

The Mason Section consists of a dextral rupture striking at 070° extending over 5.5 km through some of the oldest surfaces in the Emu Plains, S2 and S3 (Fig. 2.0). The sense of vertical slip on this section of the fault is difficult to ascertain in the field, with poor control on the fault dip at the near surface. The fault ruptures on the western tip of the section overlap with ruptures on the Leslie Hills section, and have an average horizontal offset of 0.7 m and vertical offsets between 0.3 – 0.4 m (Fig. 2.12).

Where the fault enters the higher S2 surface, terrace risers with pre-2016 displacements are visible, although anthropomorphic contouring and drainage work have reduced the potential of the sites as paleo slip-rate markers. Fault scarps on the S2 surface are up to 6 m high, cumulative with the 2016 rupture. Where the fault crosses both the Mason and Lottery Rivers, intersecting the S3a surface, a 3 m high pre-earthquake fault scarp is present, and was originally mapped by Barrel & Townsend (2012).

Two parallel strands 500 m apart cross the Mason River. The northern strand shows lower displacements in LiDAR, with a vertical displacement of 0.2 m compared to 0.4 m on the southern strand. East of the Mason River, the Mason Section continues beyond the eastern extent of the field area, climbing out of the Emu Plains and into the Highfield Range (Fig. 2.12).

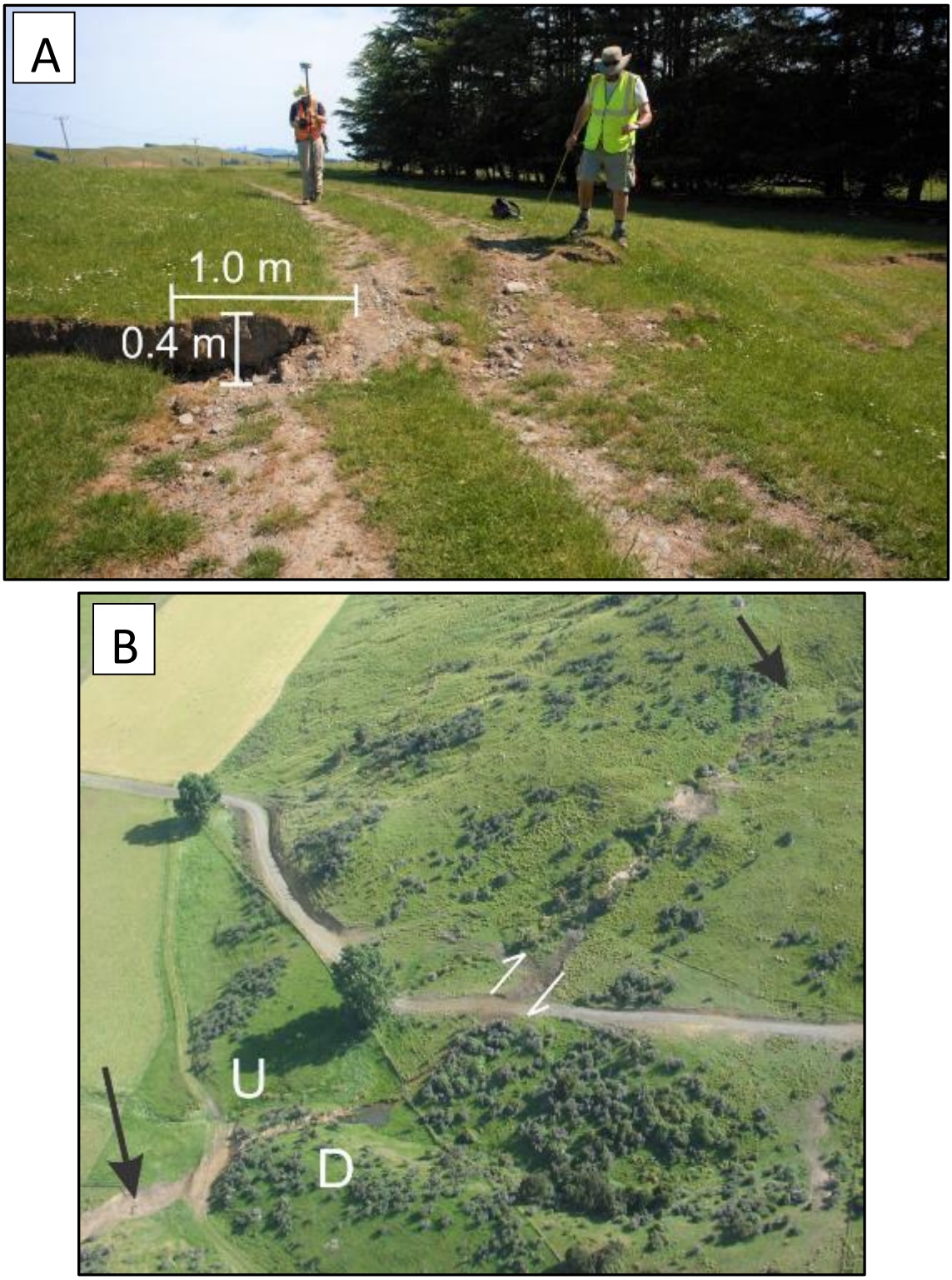

Figure 2.12: Ground ruptures on the Mason section. (A) Ground displacement from the 2016 rupture on a vehicle track on the S2c surface. (B) The Humps Fault exiting the Emu Plains above the Mason River on the toe of the Highfield range. Photographs courtesy of Kate Pedley and Jarg Pettinga.

2.3.6 Stackhouses Section

The Stackhouses section is a complex zone of left lateral segments cross-cutting a right lateral section of fault within the S3b surface above the Lottery River (Fig. 2.0, Fig. 2.13). The right lateral segment strikes at 080° S, while left lateral segments have a northwest-southeast trend between 145°- 120°. Left lateral segments have an average vertical displacement between 0 – 0.1 m, and a strike-slip component of 0.1 - 0.5 m. The right lateral segment has a vertical displacement of 0.5 m, and a horizontal component of 0.7 m. Left lateral sections of fault are separated by between 100 – 400 m and have varying lengths between 200 – 700 m (Figure 2.0).

ECAN pre-earthquake aerial photography reveals evidence for a fault scarp on the Stackhouses section (Fig. 2.14). This scarp is approximately 2 m high in the field, including the 2016 rupture. The left lateral strands of fault are not visible in any of the available pre-earthquake imagery.

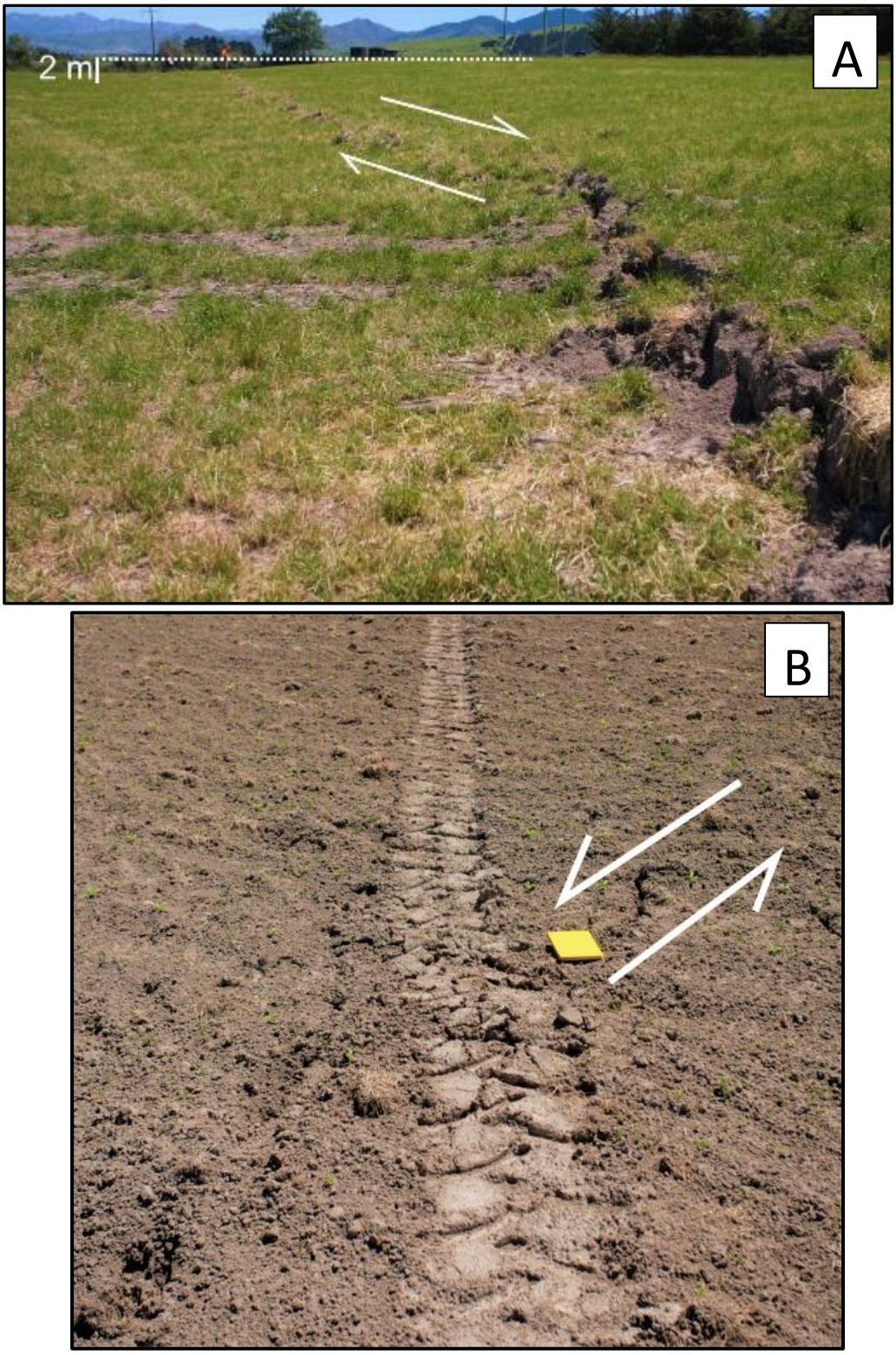

Figure 2.13: Fault ruptures on the Stackhouses section. (A) The primary right lateral segment of the section, where a 2 m high fault scarp existed prior to 2016. (B) A left lateral segment of fault scarp, with a much smaller displacement than the primary right lateral segment. Photographs courtesy of Jarg Pettinga.

Figure 2.14: Pre- and post-earthquake fault scarp presence in the Stackhouses Road section, revealed by a difference in grass density and health, possibly due to varying soil depth and moisture content of associated silts across the fault. (A) Aerial photograph taken in 2005. (B) Aerial photograph image with the same extent as (A), taken post-earthquake with the fault rupture highlighted in red.

2.3.7 Lottery Section

The Lottery section begins in the middle of the Lottery River, with a total length of 2.4 km before it crosses the Mason River and exits the study area (Fig. 2.0). The strike of the dominant fault strands lies between 050 - 060°. This fault section is aligned with ruptures on the Stackhouses Road section, and the missing connection between the two segments may be lost in the poorly consolidated material of the Lottery River (Fig. 2.0). However, the two sections exhibit markedly different strikes and rupture patterns, with the Lottery section lacking the large left lateral strands of the Stackhouses section justifying their separation into distinct sections.

From the southwest, two branching segments of fault ruptures converge to form the main trace, meeting on the Inland Road (Fig. 2.5). Between these two converging segments, a small graben formed during the earthquake (Fig. 2.15), with vertical displacements on the segments increasing towards the intersection from 0.1 m at the tips, to 0.5 m at the intersection on the Inland Road. Both segments show right lateral displacement, with a cumulative horizontal displacement of 1.75 m at the junction. Across the Inland Road, the fault crosses a large fault scarp, 9 m in height (Fig. 2.16), before entering the Mason River. As the 2016 rupture vertical displacement on this strand was 0.5 m, approximately 8.5 m of this scarp was present before the 2016 earthquake. Where the fault meets the Mason River it bifurcates, with a branch retaining the original strike, and a branch stepping 250 m north across Chaffeys Road and striking at 070° (Fig. 2.0, Fig. 2.16).

Figure 2.15: A small graben in the convergence of two fault strands of the Lottery Section on the Inland Road. Photograph courtesy of Jarg Pettinga.

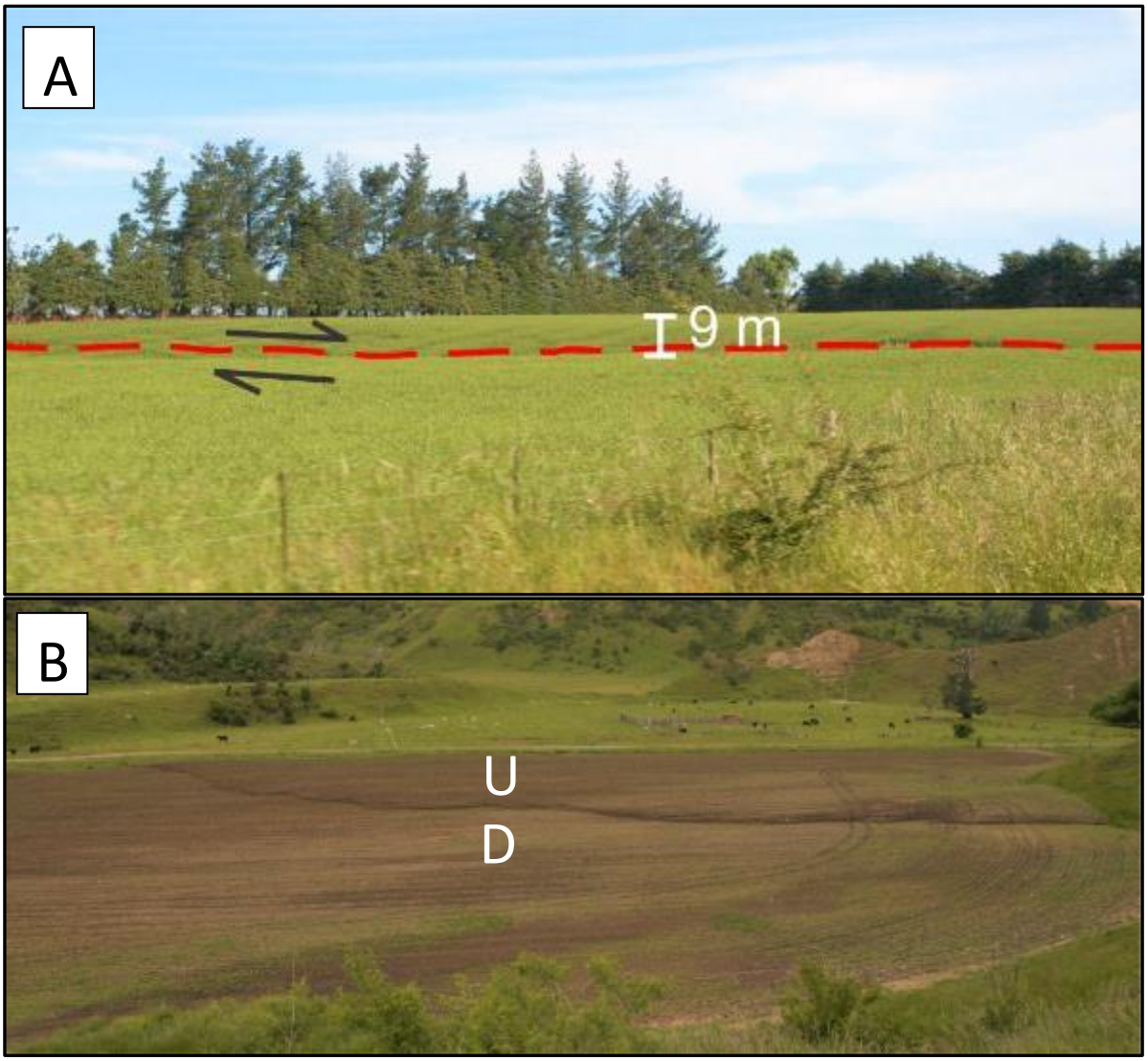

Figure 2.16: Ground ruptures on the Lottery River section. (A) Ruptures at the base of a 9 m high fault scarp near the Inland Road. (B) Small thrust fault through Chaffeys Road.

2.4 Previously unidentified faults not ruptured in 2016

Sections of The Humps Fault zone not identified by Barrell and Townsend (2012), and did not rupture during the 2016 Kaikōura earthquake, are described here. Non-rupturing fault scarps can be identified as prominent continuous linear disruptions or offsets of Quaternary geological deposits. Linear breaks in topography on the fan surfaces of the Emu Plains that cut across channels and/or go against the flow direction of the fan surface can be confidently mapped as active fault traces.

2.4.1 Highfield Cluster

South of the Mason section on the bank of the Mason River is a cluster of parallel fault traces (Fig. 2.0) on the S6-S7 surfaces. The scarps are oriented NNE-SSW at approximately 030°. The average scarp has a height of 1 m, but the horizontal sense of motion is difficult to establish without offset landforms. These fault scarps were present prior to the 2016 Kaikōura earthquake (Fig. 2.17), and upon examination in the field and from LiDAR imagery show no ground rupture during the earthquake (Fig 2.17). These fault scarps are expressed on some of the youngest surfaces on the plains and can be traced into the floodplain of the Mason River. These surfaces have not been age dated, but given the low elevation above the Mason River, could be inferred to be much younger than the surfaces dated in chapter 3 (e.g. younger than 15.1 – 7.7 ka). Unfortunately, these faults are no longer visible in the field due to large scale re-contouring of the agricultural surface by the land owner.

A large fault scarp belonging to the cluster is also visible on the S3b surface (Fig 2.17). This fault scarp is prominent in the 2013 LiDAR, and has a vertical surface offset of 14 m.

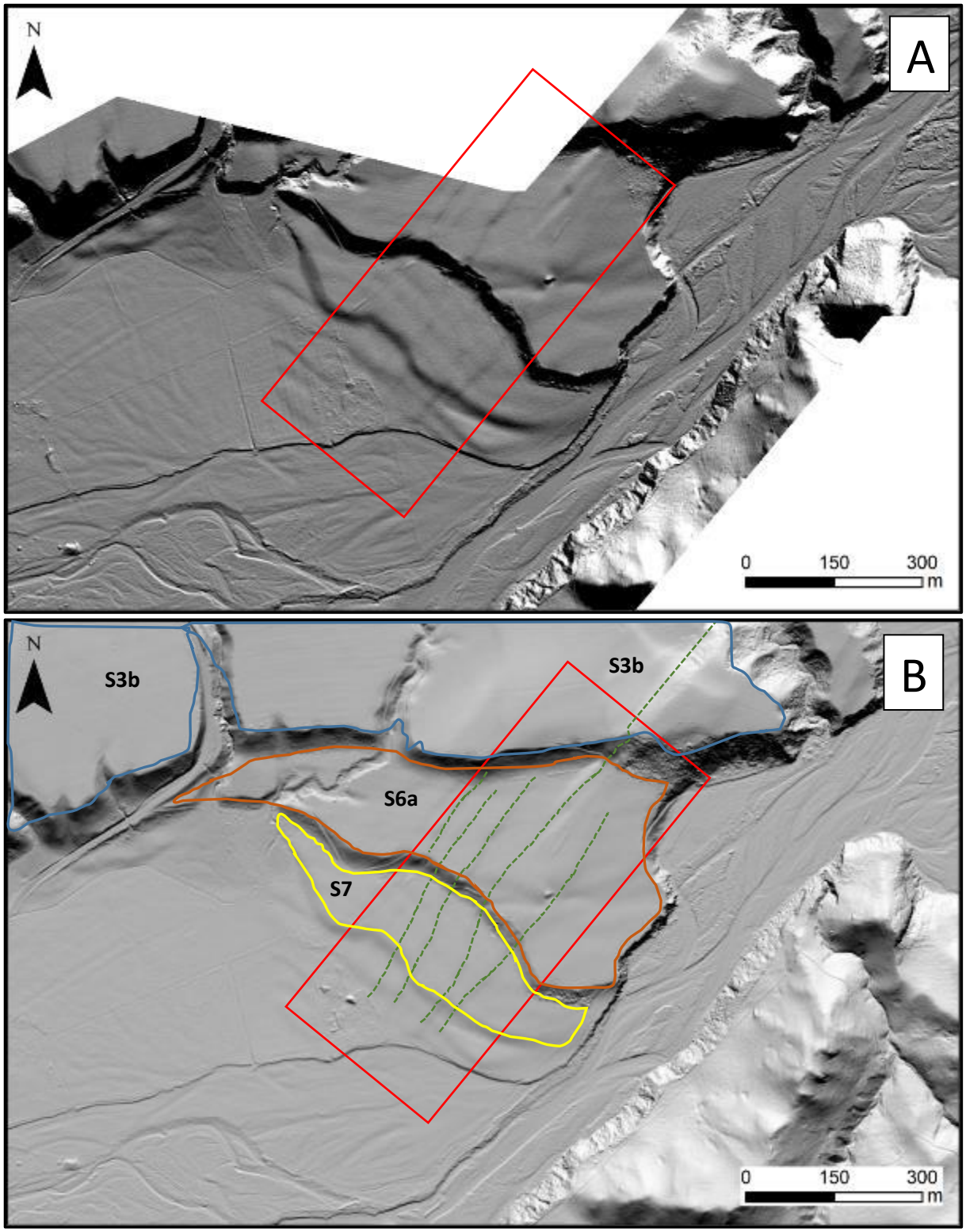

Figure 2.17: Hillshade image of fault scarps (outlined in red square) exposed in the Highfield Cluster. (A) Hillshade image taken in 2013. (B) Hillshade image taken post-earthquake with interpreted fault scarps in green dashed lines on interpreted geomorphic surfaces.

2.4.2 Sherwood Scarp

A 3 m high fault scarp crosses the S3b surface between Sherwood Road and the Lottery River (Fig.2.18). The scarp runs NE-SW at a strike of 053° for two kilometres beginning at the tip of the Leslie Hills Road section. Over this length the trace disrupts numerous channels and terrace risers formed by the Lottery River, crossing the river near the Lottery River Bridge on the Inland Road (Fig. 2.8). No offset or ruptures were recorded on this section of the fault in the 2016 earthquake. On the east bank of the Lottery River, multiple abandoned river channels with the same orientation as the scarp make identification of a continuation of the riser with any meaningful certainty impossible.

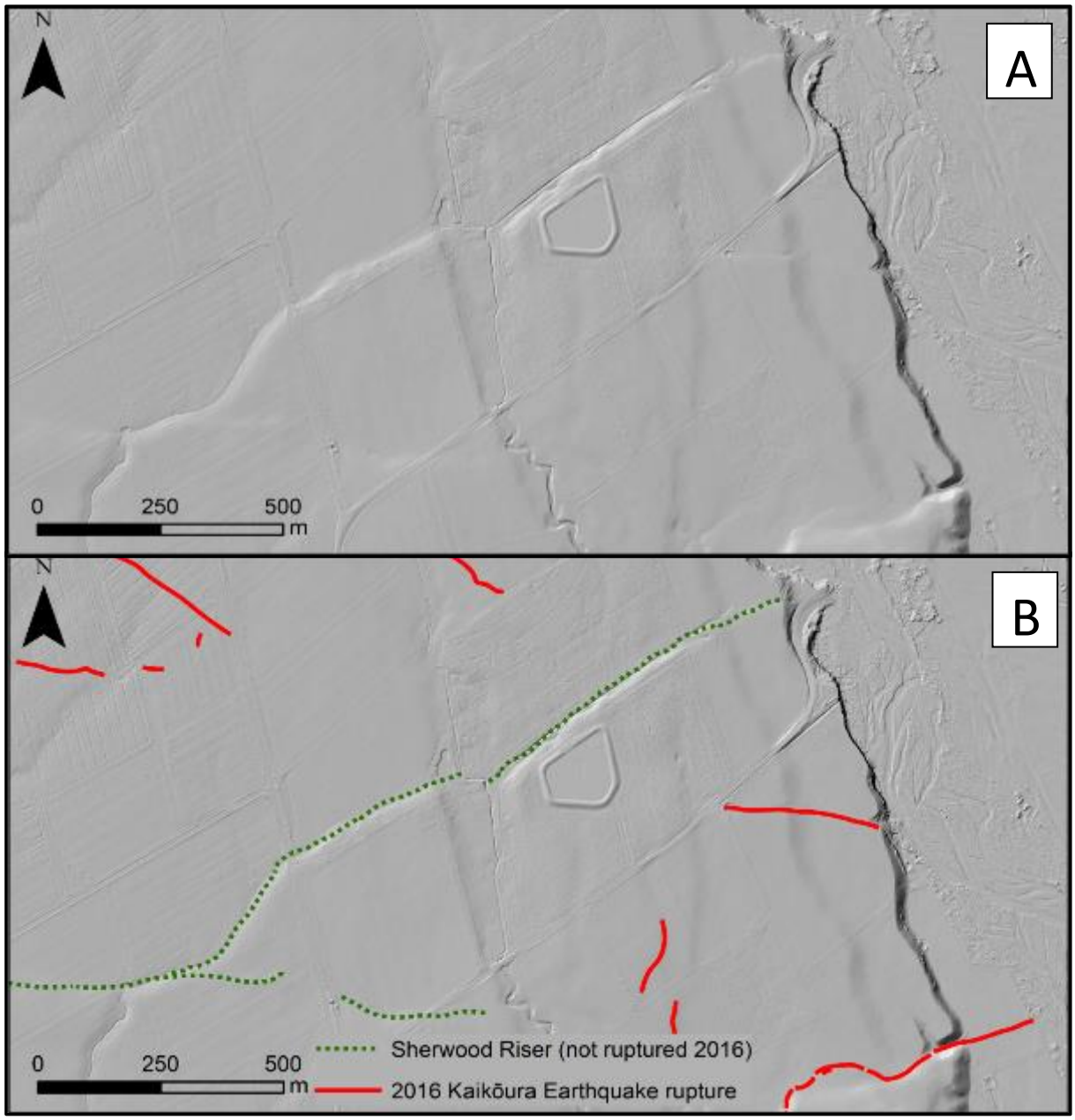

Figure 2.18: Hillshade image of the Sherwood Scarp. (A) Pre-interpretation image of the riser. (B) Interpreted riser with 2016 ruptures shown. The riser clearly intersects and displaces surfaces and paleo-channels over its length.

2.5 Discussion

2.5.1 Kinematic model of The Humps Fault

The overall kinematic behaviours of all Humps fault sections were modelled using average fault strike, inferred (after Nicol *et al.* 2018) or measured dip and net slip from field measurements (Fig. 2.19). While ruptures on sections of The Humps Fault are dominated by oblique dextral slip, the slip vector orientation varies with fault strike. Sections with strikes between 50°- 90° show predominantly right lateral displacements, while strands and sections with strikes in the range of 120° -180° are showing left lateral slip (Fig. 2.19). The Stackhouses left-lateral strands are consistent with R' shears within the overall dextral shear zone of The Humps Fault (Fig. 2.20). In comparison the Druids section helps accommodate displacement transfer within a large 1 km stepover zone towards the end of the fault and accommodates a much higher proportion of vertical slip (Fig. 2.19). Right-lateral sections appear to fit the Nicol *et al.* (2018) model as R shears within the zone of dextral shear of The Humps Fault. These observations neatly fit into the transpressional model of faulting of Nicol *et al.* (2018), where a Principal Horizontal Shortening (PHS) is accommodated by both sets of faults (Fig. 2.20).

The P-axes calculated from a moment tensor inversion in figure 2.19 appear to be clustering closely around the regional PHS of 122 ± 17° of Nicol and Wise (1992) and is similar in orientation to other faults involved in the southern ruptures of the Kaikōura earthquake which have been derived from fault slip orientations (Nicol *et al.* 2018, Williams *et al.* 2018). This is consistent with the regional contraction calculation of 116 ± 9° presented from geodetic data (Pearson *et al.* 1995). The moment tensor solution calculated (Fig. 2.19) reveals a predominantly strike slip mechanism, with a small thrust component. This overall solution seems congruous with published seismic data for the event (first motion mechanism of figure 2.21). The solution is incongruous in that the fault plane defined in the kinematic solution shows a north dipping fault plane, compared to the seismic data of Nicol *et al.* (2018) and Cesca *et al.* (2017) who indicate a south dipping fault plane. This inconsistency may be due to poor expression of the fault plane dips at the surface, caused by the high angle of fault dips measured in the field, coupled with the propagation of the rupture through loosely consolidated Quaternary deposits which have poorly preserved fault planes at the surface.

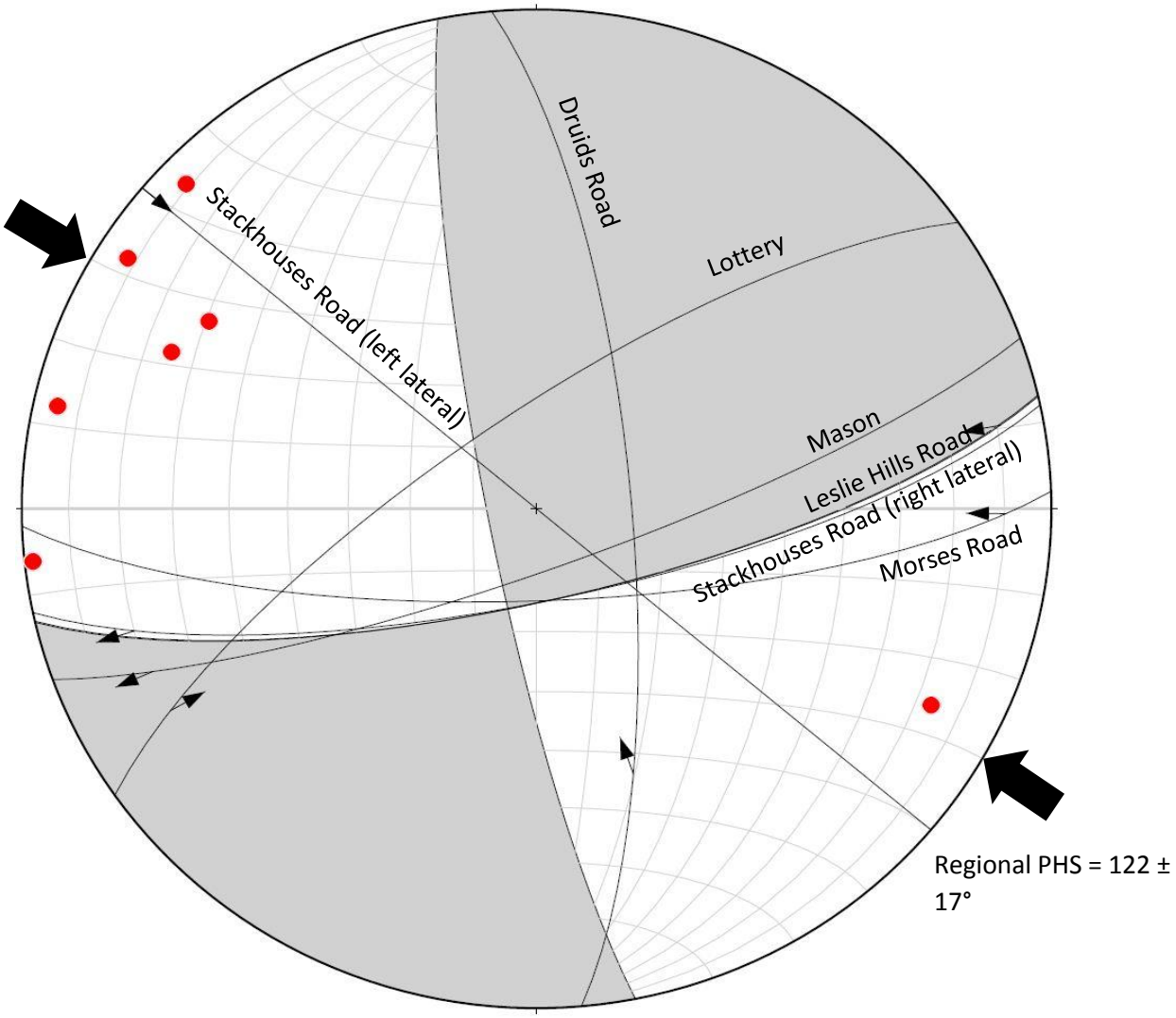

Figure 2.19: Fault plane solution for ruptured sections of The Humps Fault based on fault kinematic data (plotted using FaultKin8). P axis are in red, while black arrows represent hanging wall slip directions in the orientation of striations on the fault planes. Beach ball indicates the moment tensor solution based on a summation of the fault sections kinematic behaviour, weighted by section length. PHS orientation in black arrows after Nicol & Wise (1992).

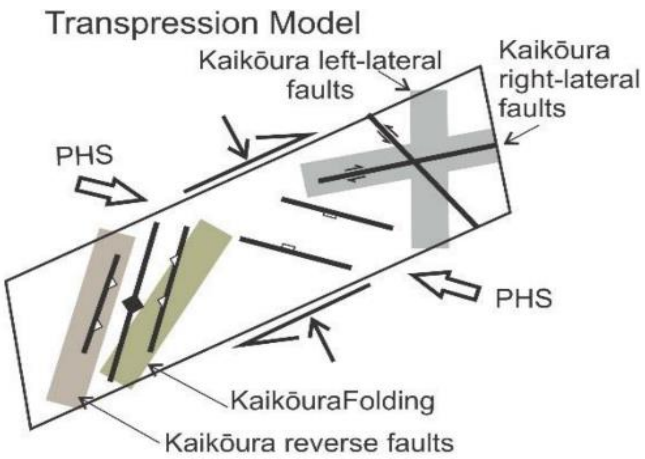

Figure 2.20: Transpressional model of faulting in the Kaikōura earthquake. Adapted from Nicol *et al.* (2018)

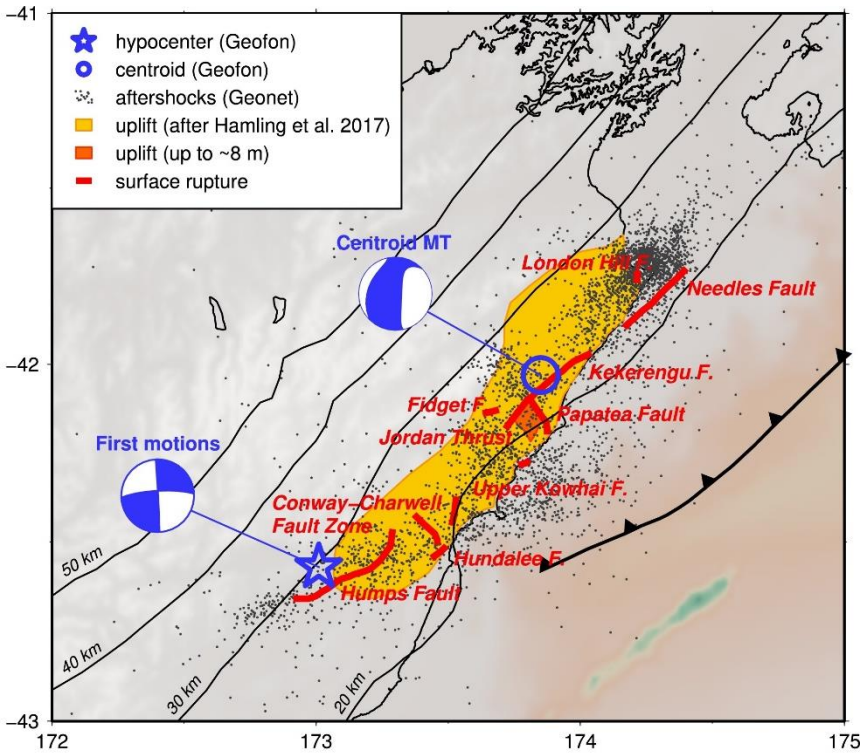

Figure 2.21: Moment tensor solution for the Kaikōura Earthquake derived from seismic data. Modified figure from Cesca *et al.* (2017).

2.5.2 Overall surface expression of faulting

Fault ruptures on the eastern Emu Plains are separated by up to 3 km normal to fault strike, with ruptures jumping across 1 km to the Mason and Stackhouses sections. This apparent discontinuous geometry of the fault strands of The Humps Fault could be attributed to two main factors: (i) the role of thick and/or poorly consolidated Quaternary deposits of the North Culverden Basin in distributing deformation (Khajavi *et al.* 2014) or (ii) the structural immaturity of The Humps Fault, i.e. that it has not produced enough cumulative displacement to produce an idealised single fault plane (e.g. Wesnousky 1988, Manighetti *et al.* 2007, Zinke *et al.* 2015). Further investigations into the deeper structure of The Humps Fault and thickness of Quaternary fill may help answer questions of why up to 3 km separates strands of The Humps Fault, and why cumulative displacements across the gaps between rupture sections appear to be missing in Nicol *et al.* (2018).

2.5.2 Temporal surface evolution of active fault structures on the Emu Plains

There is substantial evidence for repeated long-term deformation on the Emu Plains being accommodated by The Humps Fault. The pre-existing fault scarp heights vary along the length of the fault from the overall lack of expression on the modern floodplain of the Waiau River, to the 9 m high scarps of the S3a surface (Fig. 2.16). The expression of the pre-earthquake fault scarps is most likely controlled by surface age, with older surfaces having experienced more deformation from surface ruptures.

Sections of The Humps Fault that did not rupture during the 2016 earthquake show well-formed fault scarps and are prominent in the landscape. Two of these sections, which were not identified in Barrell and Townsend (2012), are the Highfield cluster and Sherwood scarp sections (Fig. 2.0, Fig. 2.17, Fig. 2.18). These sections demonstrate that the Humps Fault likely ruptured with a different configuration in the past. The exact kinematic conditions and timing of these events that caused these sections of faults to rupture is unknown, although in the case of the Highfield cluster the timing of ruptures can be constrained by the age of the low-lying terraces on the Mason River. These terraces have been interpreted here as some of the youngest in the Emu Plains, due to their elevation relative to the level of the Mason River, and the lack of erosion or modification of the surface by weathering (Fig. 2.17). The continuation of one of these fault traces onto the higher S3b surface as a 14 m high fault scarp indicates this may be a frequently ruptured trace.

The differential LiDAR reveal a strong correlation between the distribution of deformation experienced in 2016 and pre-existing fault scarps generated in past earthquakes. This is demonstrated at a large scale within the Home Stream stepover, where the 2016 rupture re-used the majority of identifiable pre-earthquake fault traces within the stepover. Small scale evidence of the persistence of deformation is preserved in the sag ponds of the Leslie Hills Road section. The Druids Road section shows a fold scarp consistent with deformation in the 2016 event. The Differential LiDAR in these sites shows fault ruptures closely matching pre-existing fault scarps.

Chapter 3. Paleoseismology of The Humps Fault zone within the Emu Plains, North Culverden Basin.

3.1 Introduction

Investigations of fault surface rupture histories are important avenues of research in active tectonics, as they provide hazard and risk information for a wide range of stakeholders in both the scientific and wider community. For the scientific community, fault paleoseismicity provides constraints on slip rates and return periods on fault surface rupture. This information, in turn, may provide insights into how faults evolve over short and intermediate timescales, and how they interact with other fault systems.

A combination of paleoseismic slip-rates, GPS velocity fields and seismological datasets are used to produce models of strain budget partitioning within tectonically active areas throughout the North Canterbury region and New Zealand (Wallace 2007). Paleoseismic trenches across fault zones yield paleoseismic slip rates and recurrence intervals of individual fault traces, providing constraints on the kinematics of regional tectonic deformation over 100-100,000 years timescales. Deformed terraces and geomorphic features are useful tools in evaluating time-integrated slip-rates, giving long-term information about the geometry and rates of faulting, but do not record the recurrence interval of faulting or dates for individual events.

One of the major questions stemming the Kaikōura earthquake was whether the 2016 Kaikōura multi-fault earthquake represents a standard rupture pattern for the faults involved. A detailed paleoseismic history of each of the 20 faults involved (Litchfield *et al.,* 2018) could provide answers as to how often a 2016 style event occurs.

Prior to 2016, the slip-rate and return period of The Humps fault zone was estimated to have a vertical slip rate of 0.2 mm/yr. with a recurrence interval of approximately 13 ka (Barrel & Townsend, 2007). Further paleoseismic studies on the Humps Fault zone since the 2016 earthquake included trenching by Hyland-Brook (2018) and an unpublished trench at the “Chaffey” site on the Emu Plains (Fig. 3.0 & Appendix 1). Hyland-Brook (2018) found two events, including the 2016 rupture, during the Holocene on the eastern-most section of The Humps fault zone. The Chaffey trench revealed evidence for two events since 52.9 ± 5.5 ka, with the penultimate event having occurred at approximately 5 - 6 ka (K. Pedley pers. comm., April 10, 2019).

Surface ages on The Humps Fault prior to the investigations on the Chaffey trench have been investigated previously, with surface ages correlated to glacial advances and climatic forcing in Gregg (1965) and Clayton (1968). Rattenbury *et al.* (2006) gives the surfaces an age of less than 71 ka.

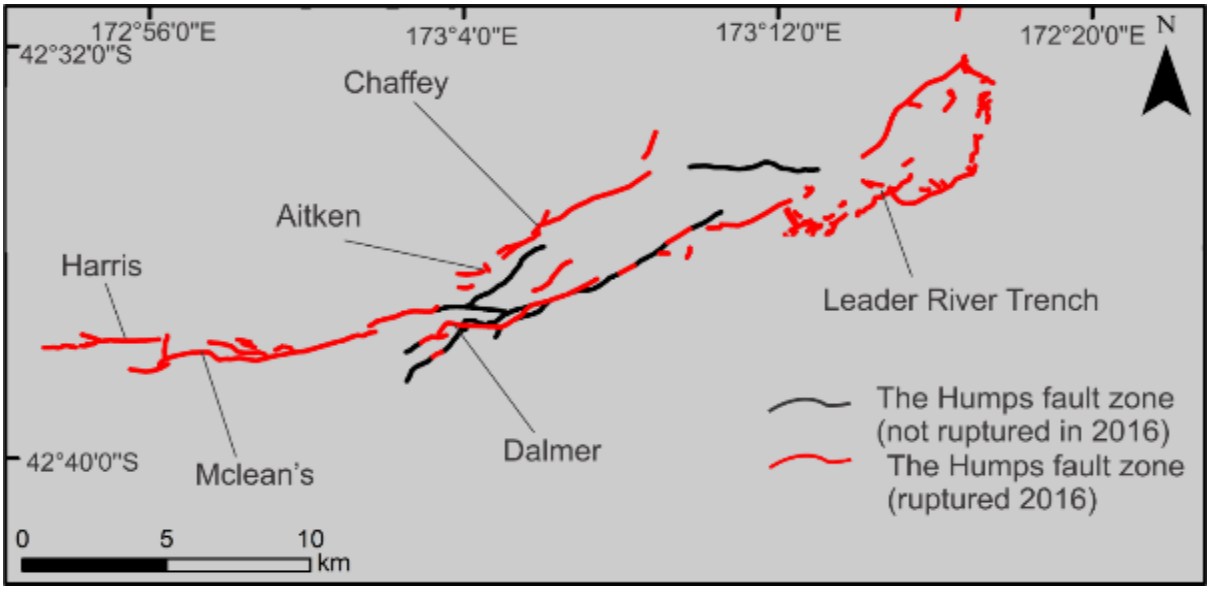

Figure 3.0: Overview of ongoing and completed paleoseismic studies on The Humps fault zone. This study encompasses the following sites: Harris, McLean's, Aitken, Dalmer and Chaffey but excludes the Leader River trench site, see Hyland-Brooks (2018).

The objectives of this chapter are as follows:

- Identify the timing and return period of paleoseismic events on The Humps fault
- Provide age constraints for surfaces on The Emu Plains
- Quantify the paleo-slip and slip-rate of The Humps fault

To meet these objectives and identify the timing and pattern of past surface rupturing earthquakes, paleoseismic trenching was undertaken. While this paleoseismic project is limited in geographic scope, it does provide further input into the understanding of the overall accommodation and transfer of slip between faults respectively associated with the southern Hikurangi Margin active subduction zone and the Alpine Fault. It provides new information on the behaviour of The Humps fault zone in the Emu Plains and complements ongoing paleoseismic studies in the southern ruptures of the 2016 Kaikōura earthquake.

3.2 Background and Methods

3.2.1 Selection of McLean's trench site and excavation

Trench site location was critical towards ensuring observations of a long record of faulting with meaningful results. Previous paleoseismic investigations in the Canterbury region targeted sites with the potential to actively deposit and trap sediments against the fault scarp, such that sites would produce recognisable, progressive deformation of strata through time. Sites that encapsulate the full width of the fault zone were preferred, such that the majority of on-fault displacement would be recorded. Sites with potentially dateable material using radiocarbon or Optically Stimulated Luminescence (OSL) techniques were prioritised. Locations near the middle of the fault zone were preferable to the western end segment, as during the 2016 earthquake surface ruptures near the western tip of the fault strand experienced less displacement (Nicol *et al.* 2018), such that measurements in these locations may run the risk of producing offsets so small such that they were not detectable in the paleoseismic record.

The McLean's site is located on a relatively narrow section of ground surface deformation along Leslie Hills Road Section (Fig 3.1 & Appendix 1), where the fault zone has transitioned from the wide complex zone of deformation on the Home Stream step-over, to a 1-2 m wide furrow of Riedel shear interactions characteristic of strike-slip faulting (Appendix 1). The fault motion during the 2016 Kaikōura Earthquake at the McLean's site was expressed as East-West striking right-lateral slip with a minor reverse slip component. The maximum vertical throw was 0.35 ± 0.05 m and maximum dextral component 2 ± 0.2 m as measured on a fence crossing the fault (Fig. 3.1, 3.2). Moving west in Figure 3.1, the fault zone comprises a narrowing zone of discrete shears, with the ground surface strain accommodated by an en-echelon array of left-stepping synthetic Riedel shears and sub-ordinate antithetic Riedel shears orientated at 30-40° to the overall fault strike.

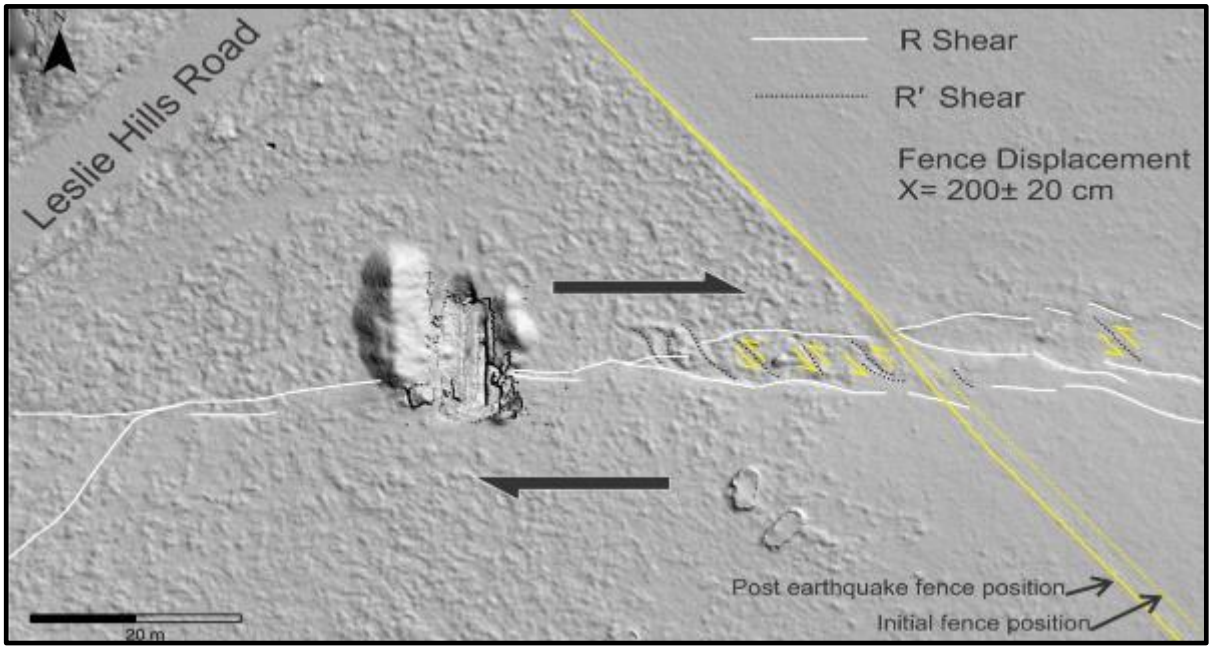

Figure 3.1: McLean's trench surface ruptures and fence offset. Location indicated in Figure 3.0.

As part of the scouting process for a trench site, an OSL sample named MP1 was collected by Dr. Narges Khajavi in late 2017. The sample was sourced from the lowest silt unit available atop the gravel fan in a stream cut bank, 200 m from the 2018 McLean's site (Fig 3.3). Results showed an age of 9.7 ± 0.5 ka (Table 3.1, Appendix 2), indicating a possible early Holocene age for the S4 surface.

This site was selected for trenching because (i) the zone of deformation is confined to a narrow zone (1-2 m) narrowing further to a single trace of negligible width (Fig. 3.1); (ii) the pre-earthquake LiDAR indicated a well-expressed, 10 cm high fault scarp demonstrating prior movement on the fault at this position (Fig. 3.2); (iii) the orientation of the fault scarp relative to the general fan surface morphology of the Emu plains indicates that the scarp may have previously ponded sediments on the downthrown (north) side of the fault (Fig. 3.2 & Appendix 1).

The McLean's trench was excavated in January of 2018 using an 8-tonne wheeled excavator, with the orientation of the trench normal to the local strike of the Humps fault (Fig. 3.4 B). The 4 m wide trench was excavated to a maximum depth of ~4 m and was benched at ~2 m depth (Fig. 3.4 A). Both trench walls were scraped clean and set up for face-logging with a 1 x 1 m string line grid. Prior to any logging or sampling commencing, the trench walls were photographed. Faults, stratigraphy, benches, clasts, ground surface, and sample locations were logged in detail on graph paper at 1:20 scale (Fig. 3.5 & 3.6). Sedimentary and soil units were described using standard geologic and New Zealand Geotechnical Society Soil descriptions (Williams *et al.* 2005) and delineated by changes in soil material (Table 3.1). Three points in the trench floor were hand-augured to ascertain the depth of the lowest trench unit on the downthrown side of the fault. These auger holes were augured using a 76 mm wide bit and dug until refusal at 3 m below the trench floor on gravel.

After trench cleaning, gridding, and logging, fourteen samples were collected for luminescence dating. Samples were collected exclusively from the east wall of the trench to maintain stratigraphic relativity. Stainless steel sample tubes measuring 60 mm wide by 200 mm long were hammered into the walls of the trench into the middle of silt-rich horizons using a sledgehammer. Samples were carefully wrapped in plastic and sealed to conserve moisture content. Four infrared stimulated luminescence (IRSL) samples were selected for analysis at the University of Victoria Wellington Luminescence Laboratory, with results being received in June of 2018, and a further three (Samples 1-B, 3 and 7 see Fig. 3.5) were sent to be independently dated using single-grain OSL, at Utah State University Luminescence laboratory. Four < 5 mm charcoal fragments samples were collected from units in the East Wall of the trench (see Fig. 3.5). One sample 'RC-1' was selected to be analysed at the University of Waikato Radiocarbon dating laboratory, with results received in April 2018 (Appendix 4).

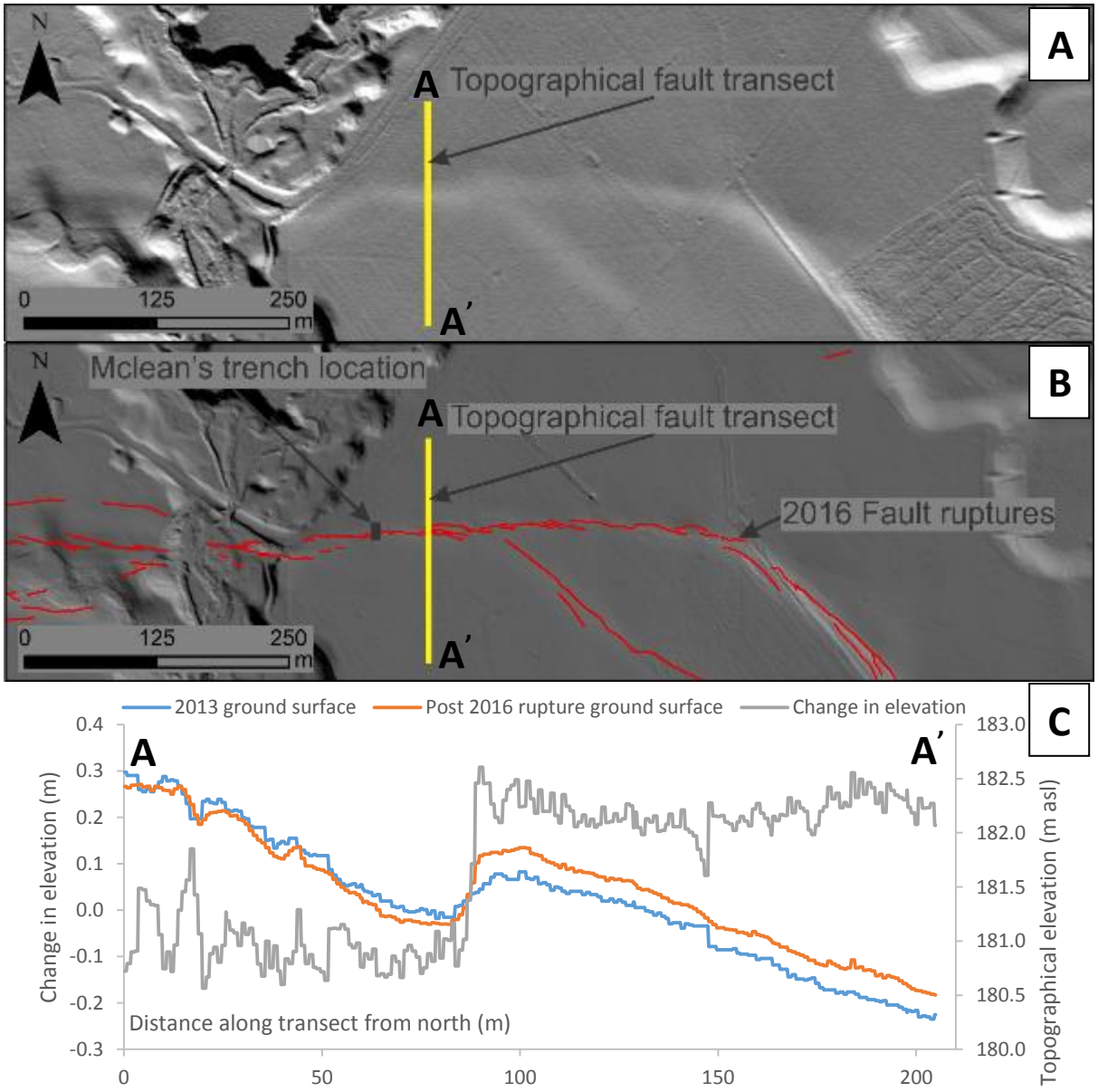

Figure 3.2: The re-occupation of paleo fault scarps at the McLean's trench location. (A) LiDAR hill-shade image taken in 2013. (B) LiDAR hill-shade image taken after the 2016 earthquake, with annotated fault ruptures. (C) Change in elevation over the McLean's trench site section of The Humps fault along transect A-A′.

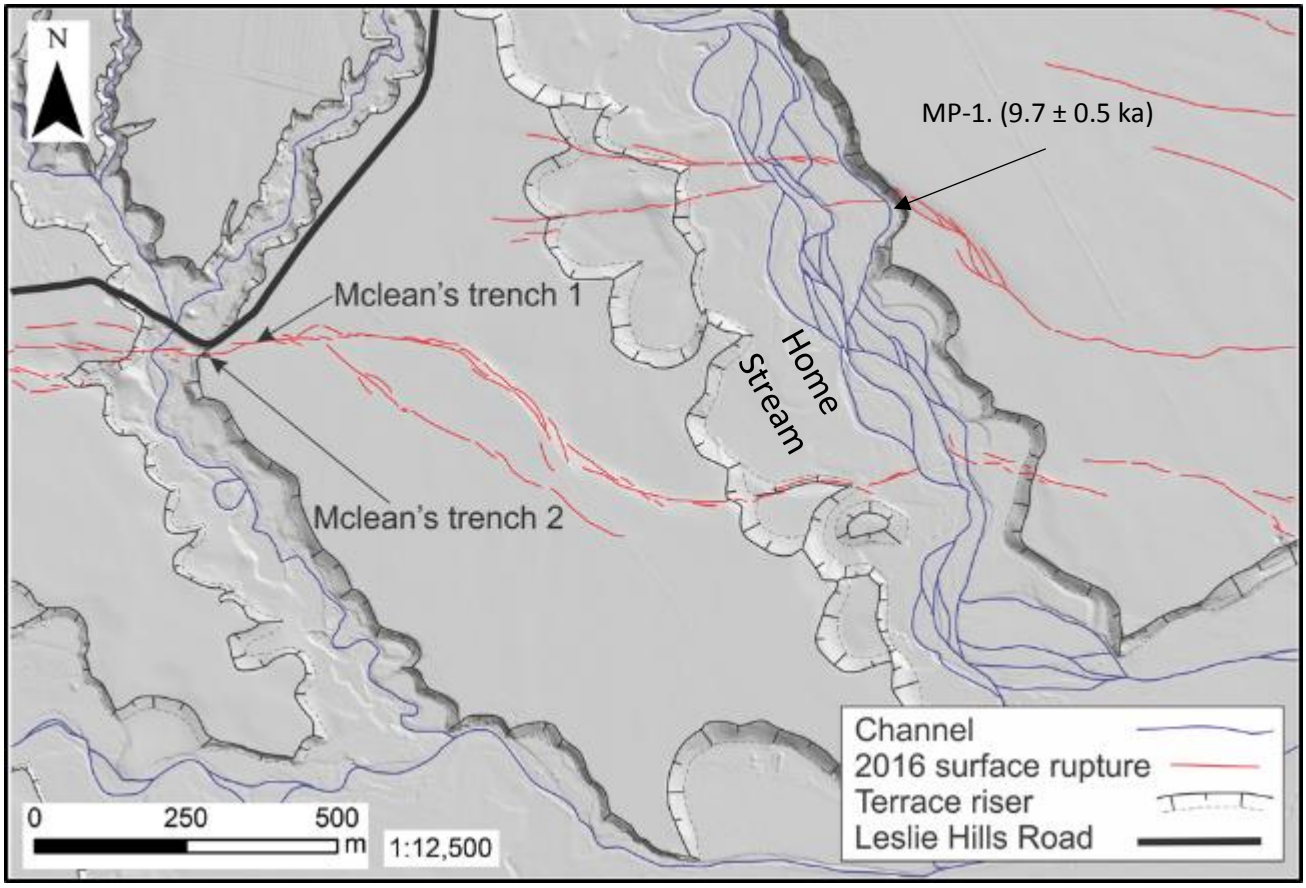

Figure 3.3: Location of OSL sample MP-1 relative to McLean's trenching sites.

Fig 3.4: (A) Bench layout of McLean's trench with white reference strings laid out in 1 m x 1 m grid pattern. OSL sample locations are numbered, and clearly circled in orange (photo taken facing east). (B) Alignment of fault rupture leading into McLean's trench (photo taken facing west).

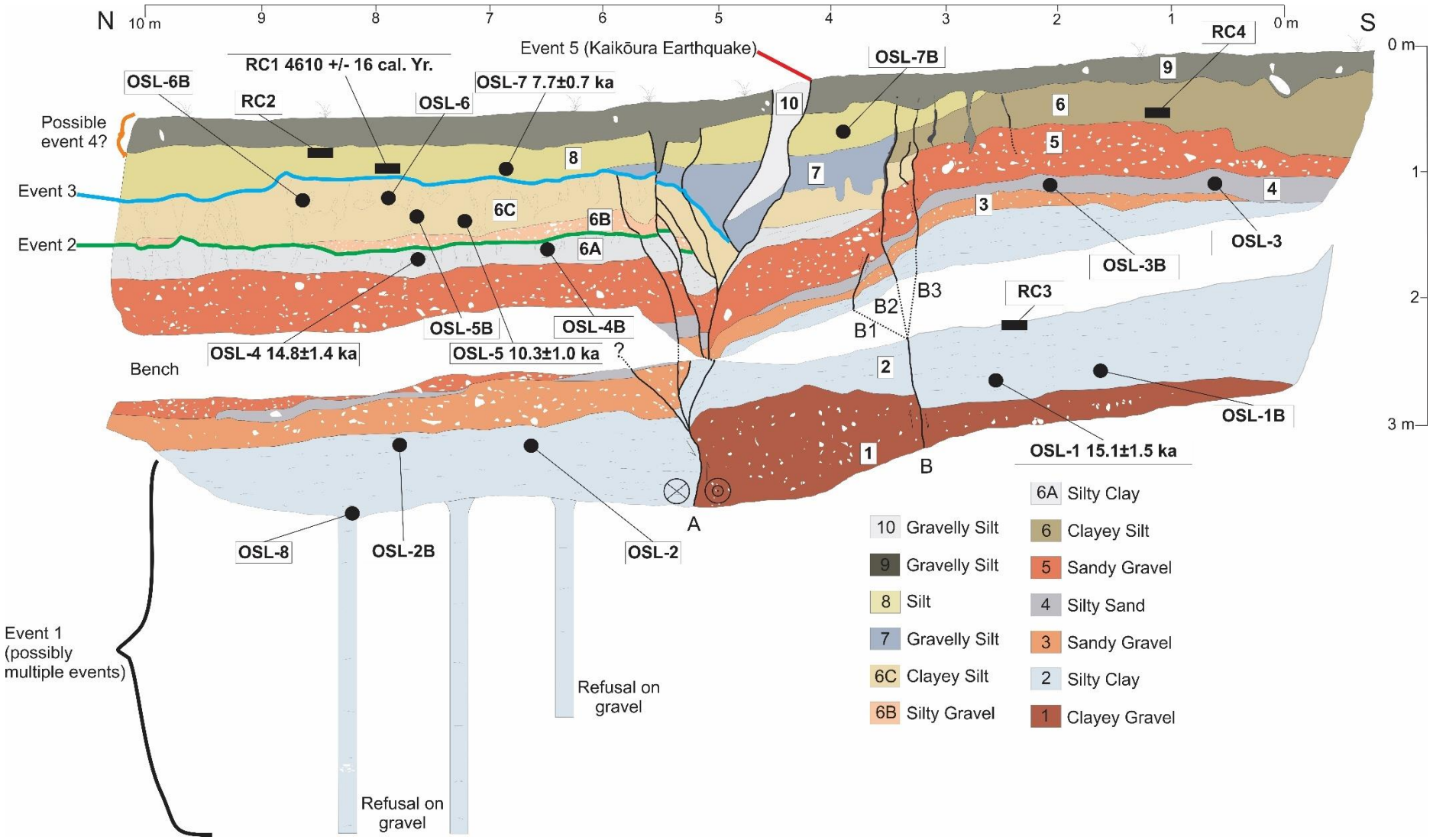

Figure 3.5: McLean's Trench log, east wall. Samples labelled OSL are optically stimulated luminescence samples, while samples labelled RC are radiocarbon samples. Samples OSL-1B, 3 and 7 have been sent for dating purposes, with results expected around June 2019. Separation of the trench log is formed by a bench cut 1 m wide to maintain structural stability of the site and provide access to the upper layers. The log matches across the bench, with further excavation into the bench at the fault zone to provide detail. Appendix 5 shows a photo mosaic of the trench.

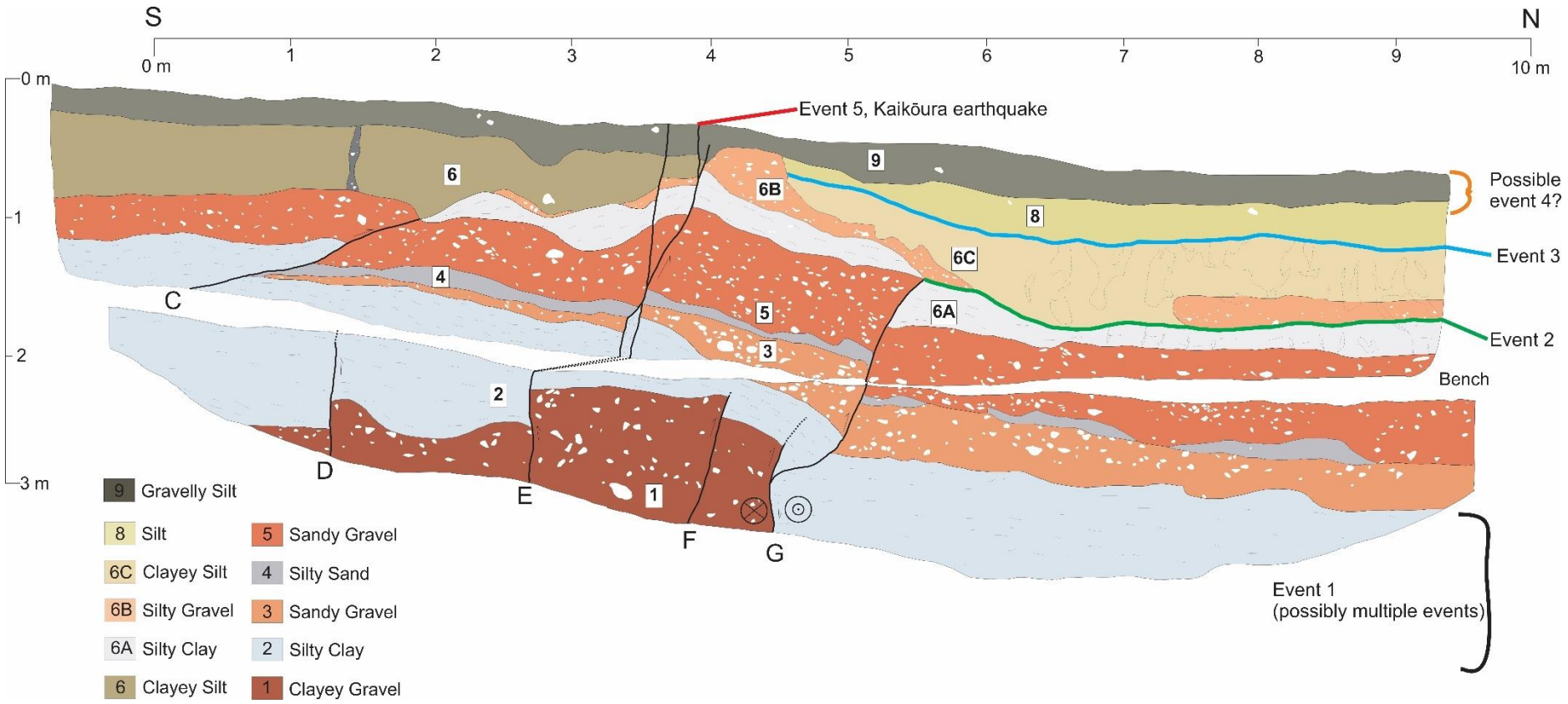

Figure 3.6: McLean's Trench log, west wall. A bench 1 m wide was cut into the west wall, units correlate across the bench. Appendix 5 shows a photo mosaic of the trench.

3.3 McLean's trench results

3.3.1 McLean's paleoseismic trenching observations

Excavation revealed five main faults in the west wall and two in the east wall of the trench, with cumulative vertical displacements ranging from 3.25 m to 0.3 m (Figs. 3.5 & 3.6). Most faults show north- side-down reverse slip. Fault B, which can be correlated across the trench on both walls, shows a normal sense of slip. Fault E is a thrust fault with much shallower than the other faults in the trench. The faults on the east side of the trench are arranged in a flower structure towards the surface, whereas faults converge on the western side of the trench into a simpler, narrow fault zone. Faults within the trench dip steeply and their dip angle varies with depth.

Trench stratigraphy is described in detail in Table 3.1, using the classification system set out by the New Zealand Geotechnical Society Soil and Rock field guide (Williams *et al.* 2005). Stratigraphy in the trench consists of a thick Clayey Gravel unit base (Unit 1) underlying a ~ 1 m thick Silty Clay (unit 2). The Silty Clay of unit 2 is thicker on the downthrown side of the fault by ~2.25 m. A 0.1 m thick Sandy Gravel (unit 3) overlays unit 2 and pinches out in thickness to the south and is thicker on the downthrown side by 0.2 m. Unit 4 consists of a 0.1 m thick Silty Sand, sits atop unit 3, with an irregular thickness, pinching in and out along its exposure. Unit 4 shows little thickness change across the fault zone. Unit 5 is a 0.4 m thick Silty Gravel, with some thickening over the fault zone.

Unit 6 is a 0.5 m thick Clayey Silt, which on the downthrown side of the fault becomes an expanded unit, with multiple facies. These units include: 6A, a Silty Clay, 6B a Silty Gravel and 6C, a Clayey Silt which are not expressed on the upthrown side of the fault. Units 6A and 6C show different patterns of grey-orange gleying. Gleying is restricted to these two units in the trench and the pattern and spacing of gleying is distinct to each unit. The gleying in unit 6A shows thin 0.05 m patches spaced at 0.1 m, while gleying in unit 6C is 0.3-0.1 m wide, spaced at 0.2 m. Because unit 6B is the highest gravel unit within the trench, it likely represents the final activity of the alluvial fan at the trench site, with silt units above being overbank flood deposits or earthquake related deposits.

Unit 7 is a Gravelly Silt wedge shaped layer localised to the main fault zone in the middle of the trench. Unit 8 is a 0.35 m thick Silt unit expressed only on the downthrown side of the fault. Soil development at the top of the trench (unit 9) comprises a Gravelly Silt, is 0.2 – 0.3 m thick and has been ploughed to ~0.15 m depth. A further Gravelly Silt (unit 10) of much lighter colour than unit 7 but with a very similar composition is fault bound, exposed to the surface with some loose topsoil coverage.

Table 3.1: McLean's trench unit descriptions. (Using conventions laid out in Williams *et al.* 2005)

Unit	Age constraints	Unit Descriptions	Observations
10	None	Light grey, gravelly SILT. Matrix supported, clasts sub rounded to well rounded, clasts <2 cm. Top is light yellow brown SILT very similar to 9 with 1% fine pebbles.	Identical material to what can be observed on ground surface along length of fault rupture, with bleached light grey topsoil and some pebbles mixed in.
9	N/A	Topsoil. Gravelly SILT.	Some shattered cobbles. Inferred plough interaction to 0.15 m depth within unit.
8	RC1 (4610 ± 16 cal. yr.) OSL7 (7.7±0.7ka) Unused: OSL7B, RC2	Firm-moderately firm light yellowish brown SILT, with some gravel. Gravel clasts are slightly weathered, subrounded-rounded, rare (1 sample) to 8 cm, typically < 2 cm, 5%.	Onlaps onto unit 6, although boundary definition near fault zone is difficult. Unit has one fault terminate in its lower boundary (East wall) although fault at this point is poorly defined.
7	None	Slightly compact-loose yellowish grey gravelly SILT. Matrix supported, slightly weathered clasts, subrounded-rounded up to 4 cm, although typically <1-2 cm. Ranges to gravelly SILT, same characteristics with finer gravel as unit 8, largest clasts = 2 cm.	Similar material to units 8 and 6 (but with a higher gravel content). Low strength. Uneven morphology of base of unit. Wedge shaped geometry confined to fault zone.
6	Unused: RC4	Firm, medium yellowish-brown to light brownish yellow at top, clayey SILT at base, SILT at top with rare rounded pebbles 1-2%.	Incorporates 6A-C in downthrown side.
6C	OSL5 (10.3±1.0ka) Unused: OSL5B, OSL6, OSL6B	Firm, light yellow brown clayey SILT with rare fine pebbles (<<1%), largest 1.5 cm. Gleying 20 cm spaced; 1-30 cm thick. In general, gleying in 6C is thicker and more widely spaced, mottling is less pronounced than 6A.	Gleying extensive throughout on downthrown side. Gleying terminates at upper boundary of the unit.
6B	None	Slightly compact greyish brown silty GRAVEL, with some clay and sand. Clasts are slightly weathered, subrounded to rounded, ranging in size up to 4 cm, typically <1.5 cm. Clast supported, massive.	Not present on upthrown side of fault on East face. Thinly present on the east face upthrown side.
6A	OSL4 (14.8±1.4ka) Unused: OSL4B	Stiff light brown silty CLAY. Vertical gleying spaced at 10 cm, 1-5 cm thick, dense orange mottling rare medium pebbles < 1% max clast size 1 cm.	Gleying present. Over-thickened on both walls on the downthrown side of fault zone. Two faults (C and G) terminate on this unit in the West wall.
5	None	Slightly compact-loose greyish brown with occasional light organic brown staining silty sandy GRAVEL. Slightly weathered, subrounded-	No change in thickness of unit across the fault zone.

		rounded up to 18cm, typically < 4cm. Clast supported, some crude bedding-massive on whole.	
4	Unused: OSL3, OSL3B	Firm, light to medium yellowish brown. Silty, fine SAND. Horizontal iron banded stain at base. Massive inside.	No change in overall thickness across the fault scarp. Unit pinches in and out throughout unit.
3	None	Moderately compact light grey, pervasively orange-red stained, silty, sandy GRAVEL, with some clay. Clasts are sub-rounded to rounded. Moderately weathered to slightly weathered. Up to 18 cm (long axis) typically < 3 cm clast supported. Crude horizontal bedding.	Slight over-thickening (0.1 m) on down thrown side.
2	OSL1 (15.1±1.5 ka), Unused: OSL1B, RC3, OSL8, OSL2, OSL2B	Very compact, very firm-firm, light grey silty CLAY. Iron stained in places throughout. Massive.	Over-thickened on downthrown side by 2.25 m. Three faults (D, F and G) terminate within the upthrown side in the unit. (West face)
1	None available	Compact, medium grey with pervasive orange-red stained Silty, sandy, clayey GRAVEL. Clasts are weathered to slightly weathered, predominantly subrounded to rounded, range in size from up to 14 cm, typically less than 2 cm. Clast supported, massive.	Three holes hand augured to find base of this unit on downthrown side of fault.

3.3.2 Luminescence and radiocarbon results

Luminescence samples were taken from the units as specified in Table 3.1. The OSL sample lab results received are in stratigraphic order, with the oldest date being at the bottom of the stratigraphic sequence and the youngest at the top (Table 3.2). The ^{14}C age of 4610 ± 16 cal. Yr. taken from the top of unit 8 (Fig. 3.5) fits into this profile. RC-1 (4610 ± 16 cal. Yr.) is slightly stratigraphically higher than OSL-7 (7.7 ± 0.7 ka) within unit 8 and provides the youngest ages within the trench.

Table 3.2: OSL Results from McLean's trench, in addition MP-1 sample is shown.

Sample Name	Deposit	Water content (%)	U(ppm) from: ^{234}Th	U(ppm) from: ^{226}Ra, ^{214}Pb, ^{214}Bi	U(ppm) From: ^{210}Pb	Th(ppm) from: ^{208}Tl ^{212}Pb ^{228}Ac	K (%)	a-value	De(Gy)	Dose Rate (Gy/ka)	Luminescence Age (ka)
Mclean OSL 1	Unit 2	19.3	2.89±0.34	3.15±0.17	3.07±0.27	10.53±0.12	1.89±0.04	0.06±0.03	55.96±0.80	3.71±0.37	**15.1±1.5**
Mclean OSL 4	Unit 6A	20.3	2.47±0.32	2.42±0.16	2.94±0.27	10.12±0.12	1.89±0.04	0.06±0.03	51.20±0.41	3.46±0.32	**14.8±1.4**
Mclean OSL 5	Unit 6C	19.2	2.85±0.34	2.87±0.17	2.12±0.25	9.50±0.12	1.95±0.04	0.06±0.03	37.48±0.24	3.64±0.34	**10.3±1.0**
Mclean OSL 7	Unit 7	15.6	2.05±0.31	2.24±0.16	1.91±0.24	7.93±0.10	1.86±0.04	0.06±0.03	25.81±0.15	3.34±0.28	**7.7±0.7**
MP-1	See Fig. 3.3	12.5	-	-	-	-	1.85±0.05	0.06±0.02	29.31±0.23	3.02±0.16	**9.7±0.5**

3.4 Interpretation of McLean's trench faulting

Excavation of the McLean's trench, and subsequent hand auguring revealed evidence for 3.3 m of vertical offset of the top of unit 1 (Fig 3.5). This offset is along the major fault revealed in the trench, fault A, and indicates repeated earthquake movements at the McLean's site. The lithology of unit 1 is consistent with a small braided river deposit. The small gravel clast size (primarily > 2 cm) and location on a large alluvial fan 30 m above the Waiau River floodplain (Appendix 1) makes the river an unlikely source for the material, with the fan S4d the most likely source.

Unit 2, a silty clay, has a lithology which is consistent with ponding against the fault scarp. This may be a result of overbank flooding sourced from the alluvial fan, or a stream actively depositing into a pond on the fault scarp. The unit shows iron staining, with little organic material present (Fig. 3.7B). Because the unit is present on the upthrown side of the fault, at some point the sediment must have infilled the fault scarp and produced a flat surface. OSL-1 near the base of the unit on the upthrown side of the scarp gives an age of 15.1 ± 1.5 ka, while OSL-4 gives an age of 14.8 ± 1.4 ka (Fig. 3.5). Given the over thickening of Unit 2 by 2.5 m (Table 3.1, Fig. 3.5), it is highly likely that multiple events contributed to the creation of accommodation space for Unit 2. The age of 15.1 ± 1.5 ka represents the age of the unit at the top of unit 1 on the upthrown side of the fault and is unlikely to be the same age as the same unit at the base of the downthrown side of the fault. Given that there is no bedding in unit 2, it is currently impossible to separate out individual events or constrain the possible timing of these events. Therefore, it is inferred that although multiple rupture episodes contributed to the offset of unit 1 and will be referred to as Event 1 (Fig. 3.5, 3.6).

Unit 3 is lithologically similar in makeup to unit 1 (Table 3.1) but is much thinner and has thin sand lenses bedded into the unit. The depositional environment may be a resumption of the same small braided river which deposited unit 1.

Unit 4 shows a much more consistent thickness across the fault scarp in both walls of the trench, indicating that a large topographic scarp was probably not present during deposition (Fig. 3.5, 3.6). The relative thinness of the layer (compared to unit 3 and other units within the trench) and silty sand composition indicates this unit was most likely an overbank flood deposit.

The top boundary of units 3, 4 and 5 are all equally offset by fault G in the west face of the trench (Fig. 3.6, 3.8). Fault G itself is capped by the base of unit 6B, which constrains the timing of the rupturing of this fault between after the start of deposition of unit 6A, and before deposition of 6B (Fig. 3.6, Fig. 3.8). The same relationship can be seen with fault C (Fig. 3.8). This paleo-earthquake is referred to as Event 2 (Fig. 3.5, 3.6).

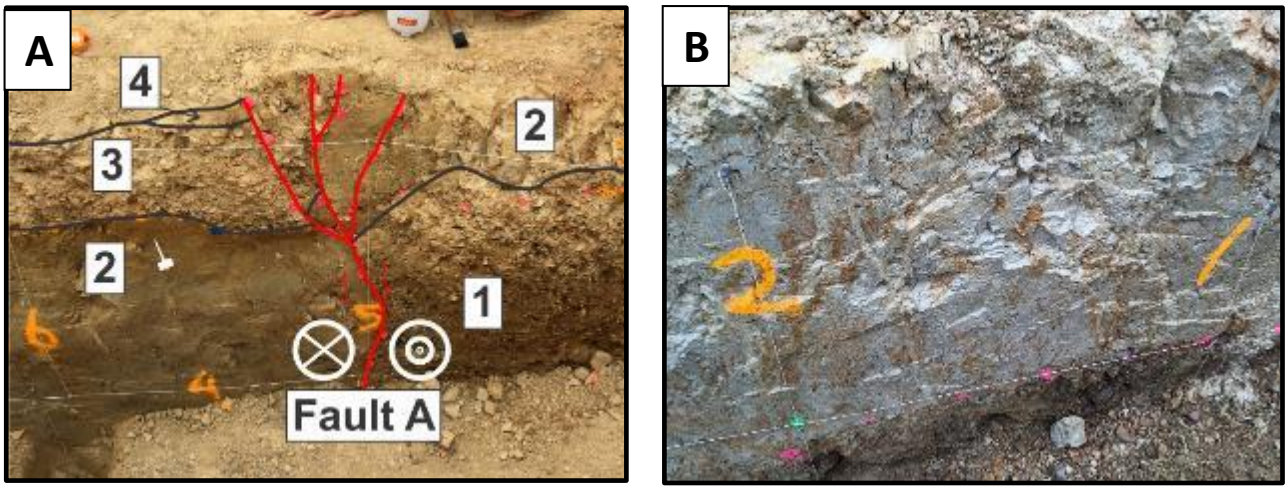

Fig 3.7: Unit photos below the bench of McLean's trench. (A) The main fault splay in the east wall, unit numbers are as labelled, fault trace in red. (B) Orange-brown staining and lack of bedding structures in unit 2 on the east wall. The boundary between unit 1 and 2 is very well defined, with little mixing across the unit boundary.

The age of the upper-most gravel unit (unit 6B) represents the final activity of the fan's active deposition of gravels on this surface (surface S4d of Appendix 1). OSL-5 and OSL-4 constrain the age of this resurfacing between 14.8 ± 1.4 ka and 10.3 ± 1.0 ka respectively. Sample MP-1 also dates the age of the highest gravel at 9.7 ± 0.5 ka in the Home Stream approximately 1 km away (Fig 3.3). This places a final small-scale resurfacing of this area of the fan between approximately 14.8 - 10.3 ka at McLean's and 9.7 ka at the Home Stream, although the last major building of the fan at McLean's is likely better represented by the thick basal gravels of unit 1 at pre – 15.1 ka.

Unit 7 is confined to the fault zone, and is characterised by low cohesive strength, higher gravel content than units 8 and 6C. The offset on the top of unit 6C on fault B2 is not reflected at the base of unit 7. Unit 7 is interpreted to be a colluvial wedge derived from unit 6 and surface debris infill. This is based on its confinement to the fault zone, its distinctive cohesion compared to the lithology surrounding it and the offset of the base of the unit on fault B2 compared to the base of unit 7 (Fig. 3.5), The timing of an earthquake which formed the unit can be constrained as having occurred partway through deposition of unit 6C, most likely the last stages of unit 6C deposition as the thickness of the unit beneath 8 is close to the total thickness of the unit away from the fault. The earthquake occurred before deposition of unit 8, as evinced by the continuity of unit 8 capping unit 7 (Fig 3.8B) and is named here the event 3 (Fig. 3.5).

Unit 8 is found only on the downthrown side of the fault, and is the youngest sedimentary package deposited of the excavated alluvial fan surface. The incidence and geometry of the deposit is evidence of deposition against a fault scarp, with no deposition occurring on the upthrown side of the fault. The top of unit 8 is within the zone of active soil processes, and has experienced anthropogenic agricultural

resurfacing to an estimated depth of 20 cm based on interviews with the land owner. Unit 8 shows several major offsets into the soil horizon, some of which have no surface expression as a result of the 2016 Kaikōura earthquake. This is most likely the result of fault movement which ruptured during 2016 but did not break the surface. This interpretation is supported by the infill of these faults by what appears to be modern organic soil material.

Deposition on the fan surface at the trench site after unit 8 and soil (unit 9) development has not occurred at the McLean's site. Evidence for a penultimate earthquake on the McLean's trench can be seen in pre-earthquake LiDAR, with a clear ~10 cm high fault scarp present in the same location as the 2016 surface rupture (Fig. 3.2). The relationship of this fault to unit 8 is not clear, as the 2016 rupture occurred in the same location as the paleo-scarp, creating a fissure which has removed much of the material on the east wall. The west wall shows a very different relationship of unit 8, with 6B being

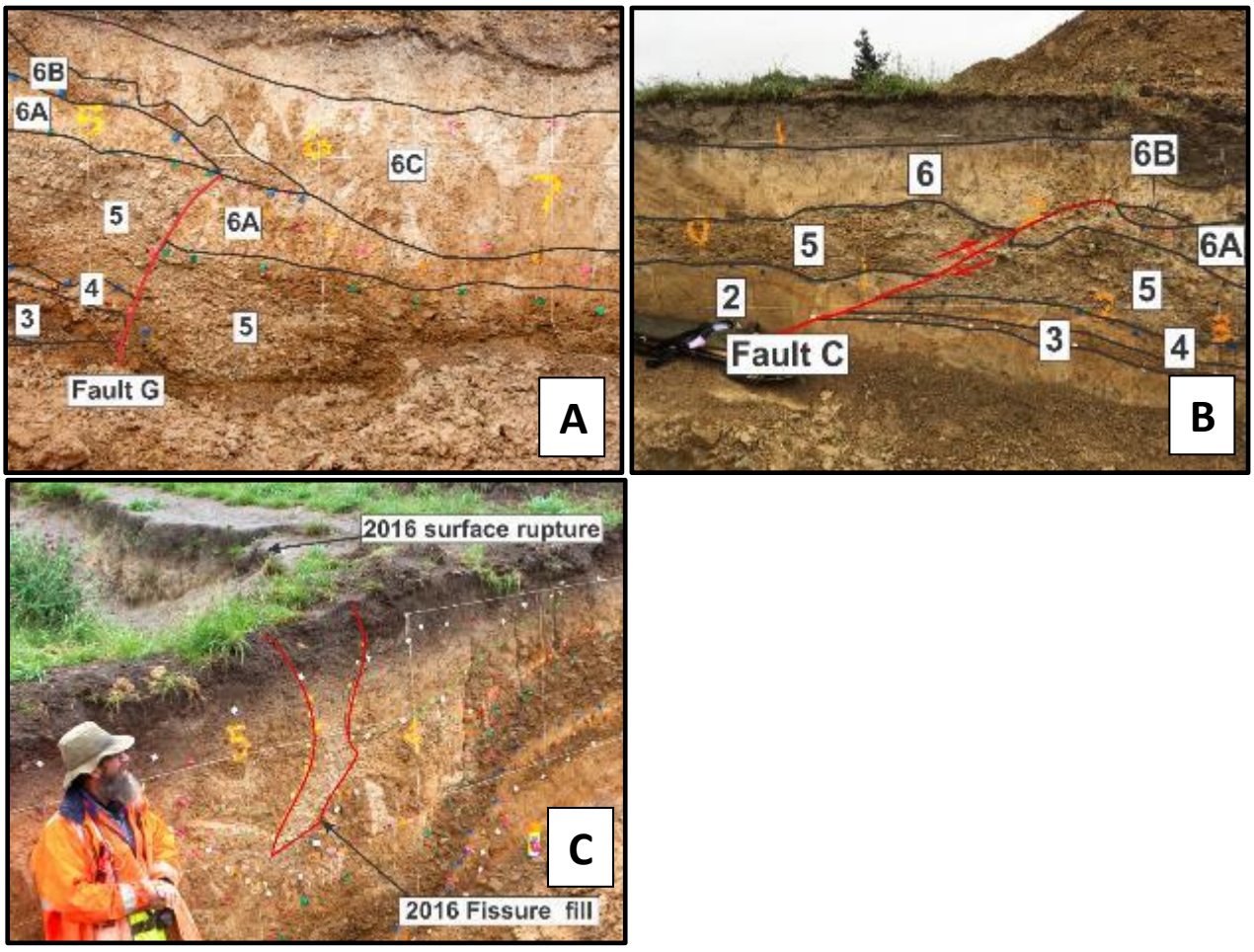

Figure 3.8: Annotated photographs of selected features in the McLean's trench. (A) Fault G termination and capping by gravel unit 6 in the west wall. (B) Fault C termination in the west wall. Deformation can be seen in unit 5, if the orientation of the fault is continued (dotted line), then a similar relationship to fault G can be inferred. (C) The fissure and associated fill (unit 10) aligned to the surface rupture of 2016.

thrust over the unit, possibly in relation to 2016, a penultimate event or event 3 which formed unit 7. If a penultimate event occurred after deposition of unit 8, it would be very difficult to see in the trench given the lack of deposited material on the surface to record deformation. Thus, a posited possible 4th event is put forward, post-dating the ^{14}C sample RC-1 of 4610 ± 16 years, and prior to European settlement of the area in 1850 (Fig. 3.5). Given the lack of evidence within the trench walls for the event, and the presence of a fault scarp in the pre-earthquake LiDAR, confidence for this event is mixed and put forward as a possible event.

The rupture of 2016 is present in the eastern wall of the trench as a large infilled fissure. This fissure is typical of strike-slip faulting on The Humps fault and similar fissures were observed to be up to 2 m deep, and 0.5 m wide immediately after the earthquake along the fault trace (Fig. 3.9) (Nicol *et al*. 2018). The fissure has been infilled with a light grey gravelly silt (unit 10) which is akin to current day loose material present on the paddock surface, with the edges of the fissure aligning to the 2016 surface rupture (see Fig 3.8C).

Figure 3.9: Fissures on The Humps Fault. (A) Typical open fissure taken days after the earthquake on a surface rupture. (B) Fault scarp leading into McLean's trench.

3.4.1 Event chronology summary

The interpreted sequence of events and faulting are as follows:

i. Deposition of small braided river on alluvial fan produces thick unit of gravel unit 1.
ii. One or more earthquake events occur, producing a large fault scarp through unit 1 (Fig. 3.5, 3.6) **(Event 1)**.
iii. Deposition of unit 2 (Silty Clay) against the now present fault scarp through stream action. Because unit 2 is over-thickened against the fault scarp by 2.25 m relative to the upthrown side of the fault, this may indicate that **Event 1** was actually multiple fault ruptures through time or may have been a large single event displacement.
iv. Deposition of unit 3 (Sandy Gravel) during resumption of alluvial fan sedimentation. Unit 3 is 0.2 m thicker on downthrown side, indicating that a small fault scarp is still present during its deposition. This scarp is likely caused by **Event 1.**
v. Deposition of unit 4 (Silty Sand) as an overbank flooding event. Unit is of a constant thickness across fault, indicating no significant fault scarp is present during deposition.
vi. Deposition of unit 5 (Sandy Gravel) as resumption of alluvial fan sedimentation.
vii. Unit 6A (Clayey Silt) deposits. Towards the end of 6A deposition an earthquake **(Event 2)** displaces existing stratigraphy: fault C, and fault G rupture, creating an offset of 6A, which is capped by unit 6B (Fig. 3.5, 3.6).
viii. Unit 6B (Silty gravel) deposits as fan material. Unit only deposits on the downthrown side of the fault, as a fault scarp ponds material against the flow of the fan, entrapping the silts with the gravel.
ix. Unit 6C (Clayey Silt) deposits, ponding against the fault scarp.
x. Unit 6 (Clayey Silt) deposits, during 6A-6C time and is stratigraphically equivalent to these three units.
xi. Earthquake occurs, creating a fissure **(Event 3)**. Unit 6 is eroded, and deposited into the fissure as a colluvial wedge, forming unit 7 (gravelly silt) (Fig. 3.5, 3.6).
xii. Unit 8 (gravelly Silt) is deposited and covers the colluvium, depositing only on the downthrown side of the fault due to the fault scarp produced by **Event 3**.
xiii. Biological development and chemical weathering of unit 8 and unit 6 to form a topsoil (unit 9) takes place over time.
xiv. Possible earthquake **(Event 4)** occurs. Creates 10 cm fault scarp visible on pre-existing LiDAR on site (Fig. 3.2). This scarp is reworked by ploughing and agricultural activity.

xv. **Event 5** occurs on the 14th November 2016. A fissure opens, and takes several months to infill with surface material, forming unit 10 (Fig. 3.5, 3.6). The rupture creates several offsets in unit 8 which do not break the surface and are infilled by unit 9 (organic soil material) (Fig. 3.5, 3.6).

3.5 Paleo-slip near McLean's trench site

A gravel paleo-channel within silt was identified in a road cutting 80 m west of the McLean's trench (Fig 3.10A) and is referred to as McLean's trench 2. This channel appeared to be intersecting the fault at a high angle and have potential as a piercing point for a slip-rate measurement. A trench parallel to the fault to a depth of 2 m and length 7 m was excavated utilising the same excavator used on the McLean's trench (Fig 3.10B).

The channel size and shape in the road cutting and in the trench was measured found to be similar in orientation and geometry (Fig. 3.11, table 3.3). The road cutting and trench gravel fill is described as a compact greyish brown silty, sandy GRAVEL, with slightly weathered sub-rounded clasts. Clasts are up to 20 cm in length, typically smaller than 3 cm. The underlying silt is described as a very compact, very firm, light grey silty CLAY, with iron staining, with no bedding or changes in grain size apparent.

The gravel surface in the trench and in the road cutting is similar in composition and description to units 3 and 5 in the McLean's trench, while the underlying silt package is also similar to unit 2 in the McLean's trench (table 3.1). Given that the sites are 80 m apart and are on the same fan surface, it is likely that the gravel unit is equivalent in age to units 3 and 5.

The road cutting has removed the portion of the channel which would have met the fault. To make an offset measurement, a projection of the channel to the fault was made with a length to fault from the channel in the cutting of 2 m (Fig 3.10B). The projection is established using the measured strike of the channel (036°). The uncertainty of the projection in the field is estimated at 15°, giving a measurement of 7.2 ± 0.5 m.

Using the age data from the McLean's trench, the age of the gravel fill is interpreted to be the same age as unit 5 and 3, which is between 15.1 ± 1.5 ka – 14.8 ± 1.4 ka. The silt package forming the channel walls is equivalent to unit 2, with an age of 15.1 ± 1.5 ka. The channel is therefore between 14.8 ± 1.4 ka and 15.1 ± 1.5 ka in age, with a total offset of 7.2 ± 0.5 m. This gives a horizontal slip-rate of 0.49 ± 0.1 mm/year for this strand of The Humps Fault.

Table 3.3: Channel measurements at road cutting and road cutting trench.

Feature:	Road cutting	Trench
Channel base width (m)	0.22	0.25
Channel top width (m)	0.78	0.63
Channel depth (m)	0.39	0.43
Orientation axis	036°	040°

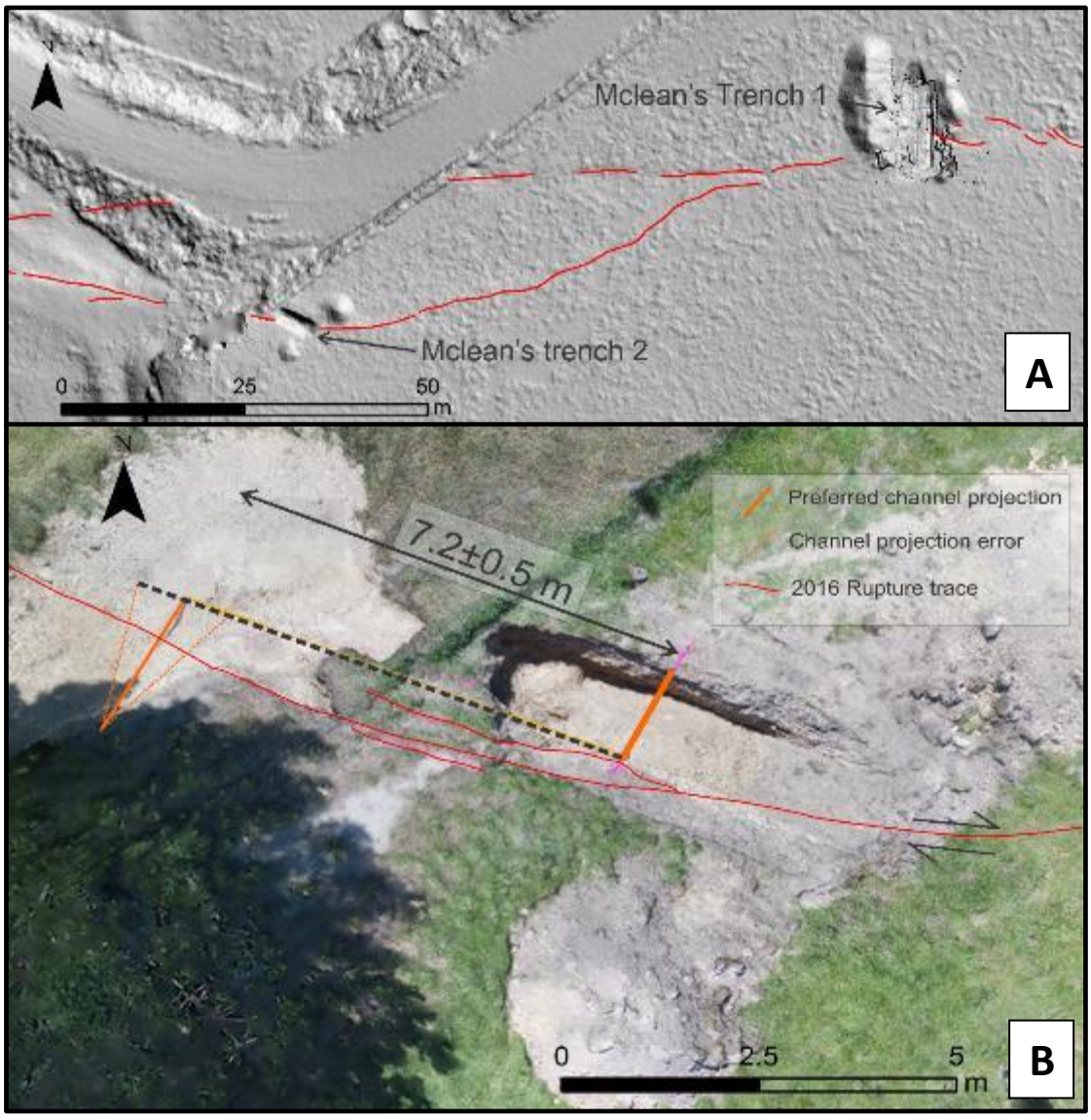

Figure 3.10: (A) Piercing point measurement on McLean's trench 2. (B) Location of McLean's 2 trench in relation to McLean's trench 1.

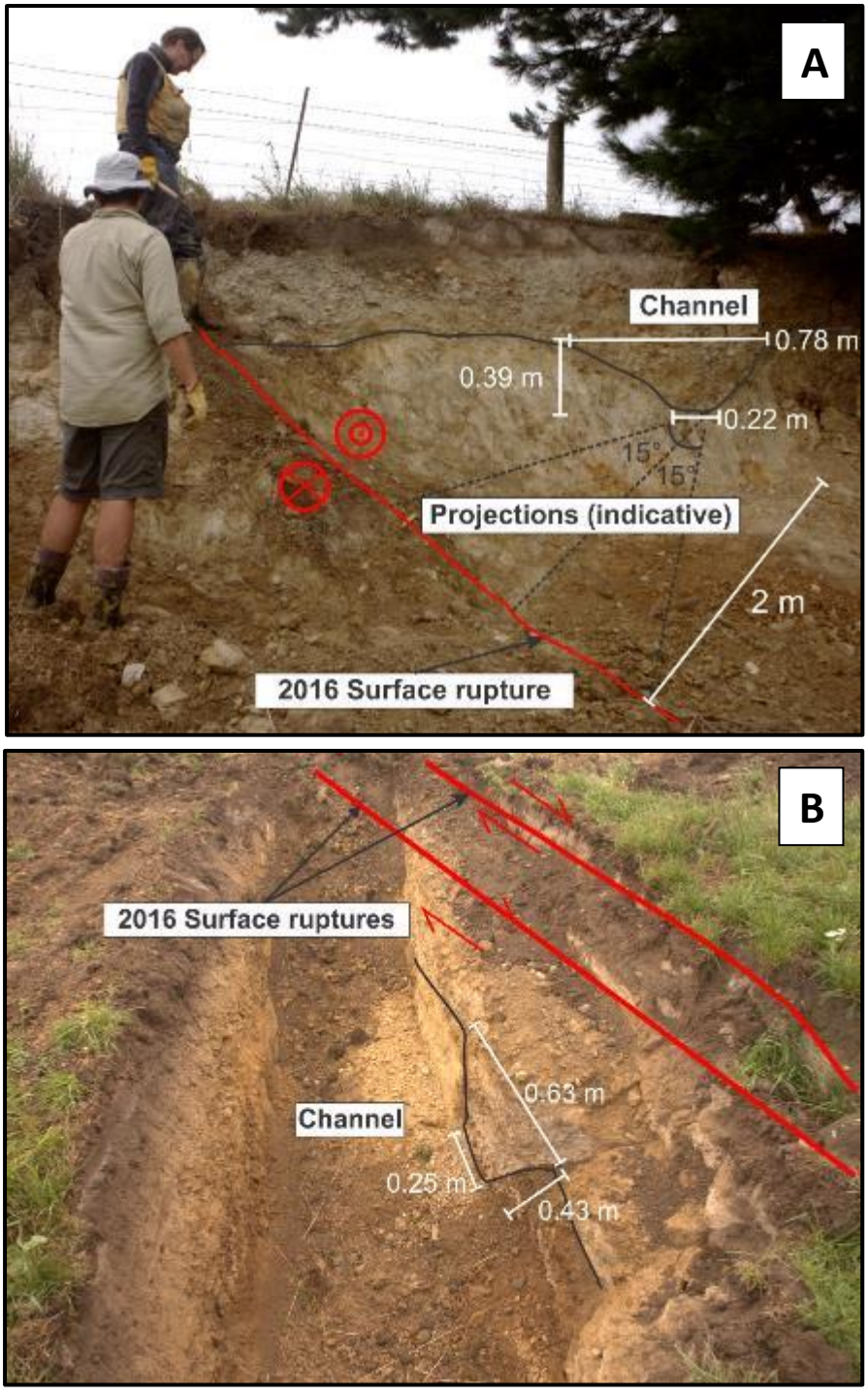

Figure 3.11: Channel measurements at both the road cutting (A) and trenched location (B).

3.6 Slip-rate estimates from offset landforms

Time-averaged slip rates were also calculated from select landforms from the map in Appendix 1. The geomorphic features were selected, and their offsets measured, using the post-earthquake 2016 LINZ LiDAR DEM. Landforms on the Emu Plains including channels, fans and terrace risers were considered for evaluation. Criteria for selection included:

- Evidence for post-formational erosion or modification of the feature
- Clear evidence of a pre-2016 fault scarp on the feature
- Cleanly offset features, at a high angle to the fault trace
- Dateable sediments to allow age-dating of the geomorphic features

Based on these criteria, two geomorphic features on the Emu plains were investigated for slip rate measurements. The features were displaced during the 2016 rupture of The Humps fault and exhibit more cumulative offset in total than recorded in the 2016 earthquake. Horizontal and vertical components of displacement were measured on these deformed geomorphic features as described below.

3.6.1 Slip-rate measurement methods

Several components of the displaced features were considered for measurement. For terraces, the crest and base of the riser, as well as cross-sections through the riser, were used to measure offset. Riser crest and base projections are identified as the point at which the slope changes orientation. To measure offset on channels, the alignment of the centre and edge of the channel was identified on both the up and downthrown side of the fault. There are several important sources of inaccuracy involved in measuring the offset of geomorphic features, this includes: (i) the resolution of the DEM used (1 m); (ii) post-deposition erosion and slope modification after deposition, especially regarding erosion of the fault scarp over time; (iii) the precision of picking the geomorphic feature. These were incorporated into the total uncertainty in the slip-rate calculations.

3.6.2 Aitken Site

A large paleo-channel cuts through a large fan surface on the north branch of The Humps Fault on the Emu Plains near Sherwood Road where it intersects the Stackhouses Road section of fault and is referred to here as Aitken site (Fig. 3.0 and Appendix 1). In this section of the fault, The Humps Fault is split into two parallel arms with slip distributed unevenly between them (Nicol et al. 2018). Where the channel intersects the fault, it is approximately 240 m wide and 3 m deep at its lowest point. The

2016 surface rupture at the site is a well-defined trace following the pre-existing fault scarp along the western margin of the channel. Where the fault crosses the eastern channel riser, the magnitude of surface displacement is almost imperceptible in the field and is best picked using the LiDAR DEM (Fig 3.12). In the centre of the channel, a 170°-striking, sinistral surface rupture trace intersects the main fault branch (which strikes at 071°). Here, the 2016 rupture produced a 0.4 m vertical offset and a 0.55 m horizontal dextral offset, measured on a fence line to the east of the channel.

Using the LiDAR model, offset of the base of the riser from across the fault is measured at 6 m horizontally (Fig. 3.13A). The surfaces at the site are vertically offset by 1.5 m, with the south side of the fault being displaced downward (Fig. 3.13B). The crest and base of the riser measurements are in agreement with each other at c. 6 m. Given the resolution of the DEM and ease of picking this offset feature, an uncertainty of ± 1 m is assigned at this location.

The surface has no age constraints as of yet; however, in February of 2019, two OSL samples were taken to age date the surface and results are pending. The expected age of the surface, based on its position in the landscape and my mapping (Appendix 1), is younger than the surface age taken from the 2018 Chaffey trench (52.9 ± 5.5 ka) and older than the McLean's surface age of 15.1 ± 1.5 ka (using the basal gravel age of McLean's) due to its position in the fan stratigraphy of the Emu Plains (Appendix 1). This places the age of the fan in the range of 15-53 ka old, giving a horizontal slip-rate range of between 0.1 - 0.4 mm/yr. and a vertical slip-rate between 0.02 - 0.10 mm/yr.

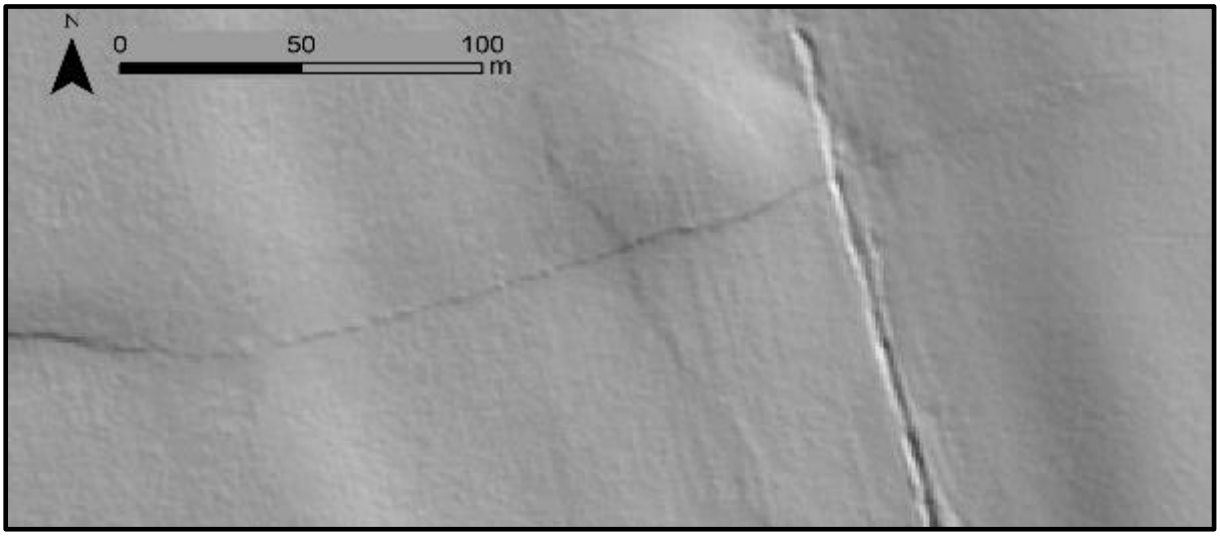

Figure 3.12: Hillshade image derived from LiDAR of The Humps Fault rupture crossing the Aitken offset channel risers. See Figure 3.13 for interpretation.

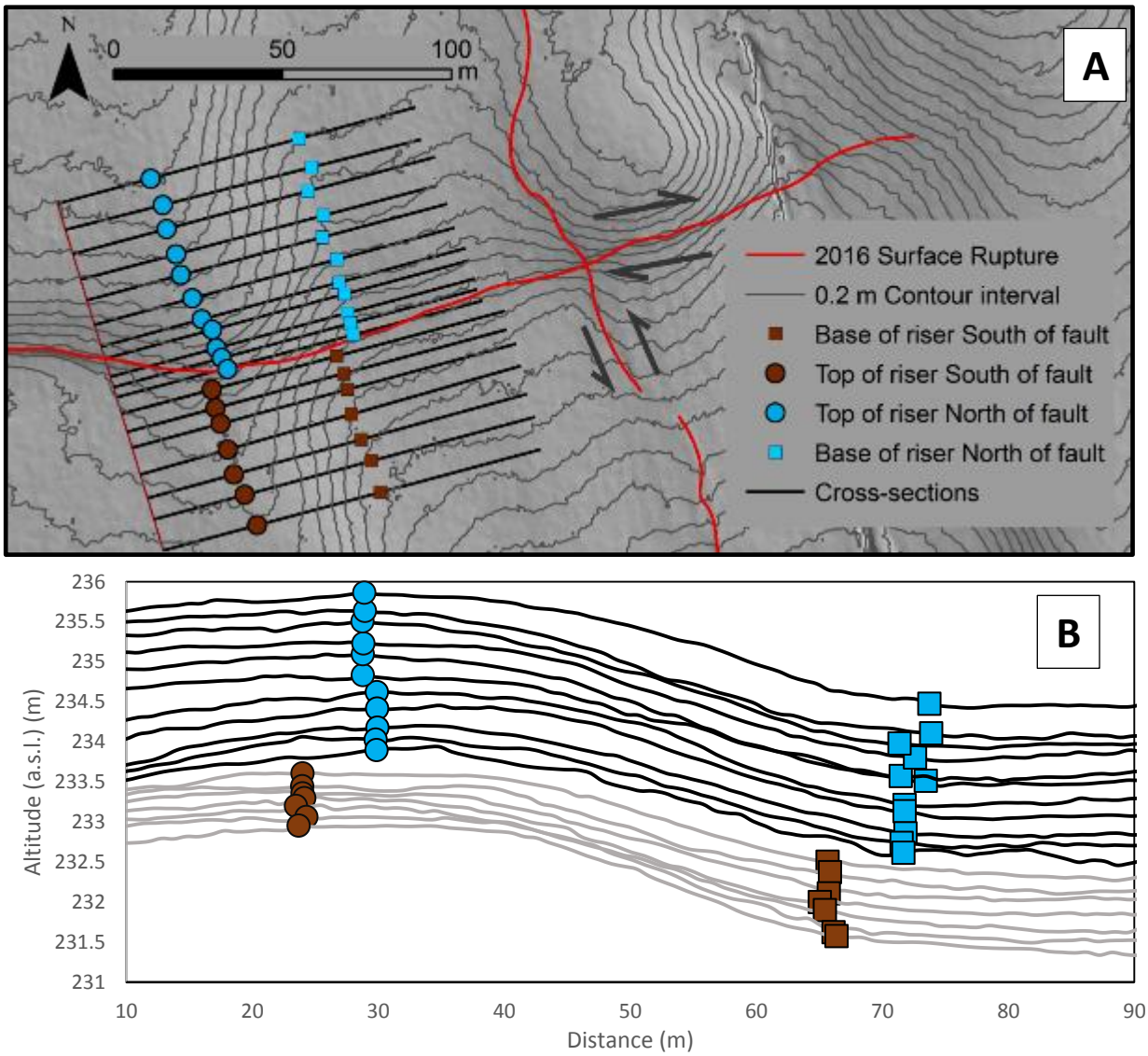

Figure 3.13: Piercing point offset at the Aitken Site on the Emu Plains. (A) Offset interpretation of riser base and top. (B) Cross-sections of riser using black lines on (A), showing vertical change and horizontal change in alignment across the fault.

3.6.4 Harris location slip-rate measurement

A small paleochannel is present near Druids Road and is referred to here as the Harris site (see Fig. 3.0 and Appendix 1). The channel is within the Morses Road section, the fault here striking at 090°, intersects this channel at a 45° angle, with the channel orientation at approximately 135°, flowing NW to SE. The channel depth ranges from 0.5 m to 1 m (Fig 3.14, 3.15), and due to its shallow nature is difficult to pick out with the naked eye in the field. The 2016 rupture produced a dextral offset of 1 m, and vertical offset of 0.2 m, which was measured on a fence 30 m away from the channel riser.

The riser crest and base show an offset of 6 m. When resolved onto the fault considering the angle of intersection, this gives an offset of 8.5 with a calculated uncertainty of ± 1 m (Fig. 3.15). There is no apparent vertical offset between the north and south parts of the fault – the measured 0.2 m offset on the fence is imperceptible on the ground surface. This surface is estimated to be equivalent in age to the McLean's trench age, giving a preliminary age of approximately 15.1 ± 1.5 ka, equivalent to the unit 2 gravel of McLean's trench. Given a total slip of 8.5 ± 1 m, this would equate to a horizontal slip-rate of 0.57 ± 0.1 mm/yr. for this section of The Humps Fault. OSL samples of the silts overlying the gravels forming the channel were taken in February of 2019, with results expected in August of 2019 to confirm the age of the channel.

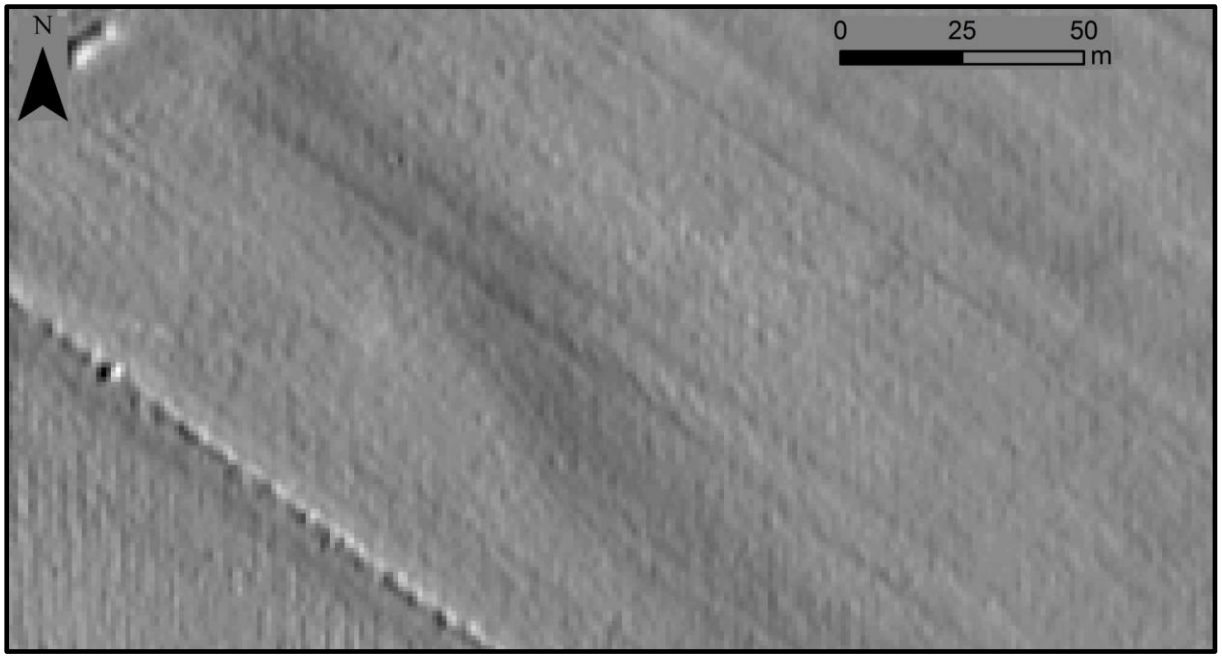

Figure 3.14: Offset riser before interpretations. Image is illuminated 045° from north.

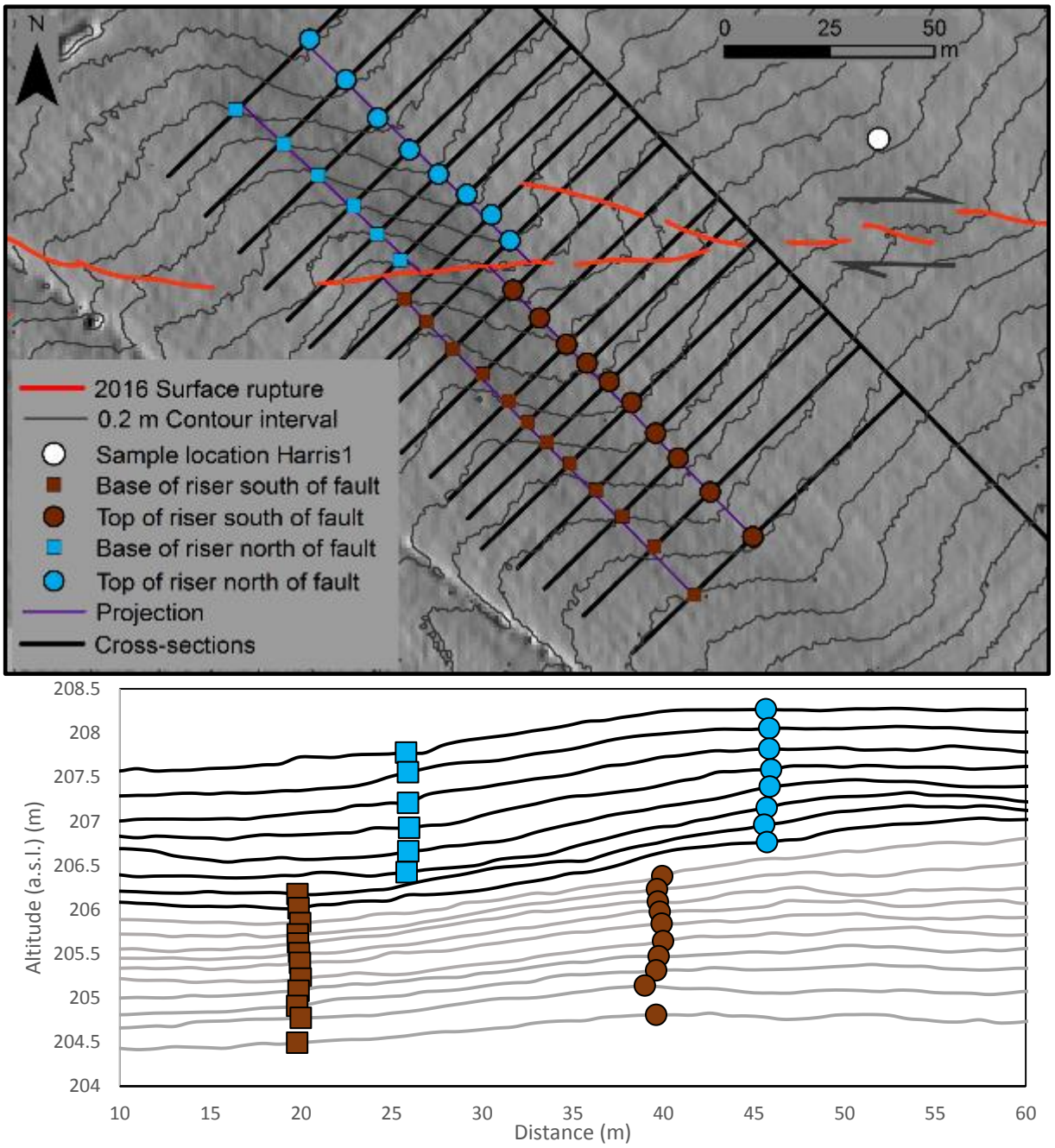

Figure 3.15: Harris site offset terrace. (A) Interpretation of offset terrace, showing interpreted riser and riser base projections. (B) Cross-sections of riser interpretations, corresponding to black lines in (B).

3.7 Discussion

3.7.1 McLean's Trench

The OSL and ^{14}C dates produced are some of the first geologic age constraints on paleoseismic activity for the Emu Plains section of The Humps Fault. The five dated OSL samples within the McLean's trench range in age from 7.7 ± 0.7 ka to 15.1 ± 1.5 ka (Table 3.2; see appendices 2, 3 for full OSL lab report). The ages also provide numerical age constraints on the associated fan surface of the Emu Plains. These ages can be correlated to a ^{14}C sample taken at the top of the sequence (Fig. 3.5; see appendices for lab report) which constrains the minimum age of sediment deposition to 4610 ± 18 years, and an additional OSL sample taken (MP-1) taken from the top of the gravel layer in a stream cut bank nearby which dated the fan surface at 9.7 ± 0.5 ka (Table 3.2, also see appendix 1, 2). Sample MP-1 was taken 0.6 m below the surface, approximately the same depth as the McLean's trench sample OSL-5 which had a dated age of 10.3 ± 1.0 ka. This supports the reliability of the McLean's trench OSL ages.

The 3 ka age gap between the two samples (OSL 7 and RC1) within the same unit may indicate that either sample may not be the representative of the age of the unit. For example, the younger age of the ^{14}C sample could be explained with the origin of the charcoal being bioturbated down the sequence. Alternatively, the older OSL age could be the result of partial bleaching of the material, which is possible given that the material is likely to be locally-derived, and therefore may have had a relatively lower chance of full exposure to light to fully reset its luminescence signal.

Given the lower inherent uncertainty of the ^{14}C result and the lack of burrows or evidence of bioturbation in unit 8, the ^{14}C age of 4610 ± 16 cal. Yr. is preferred over the OSL age of 7.7 ± 0.7 ka for unit 8. This may imply that all of the OSL ages taken from silts in McLean's trench are partially bleached, given they likely share a common path from source to sink. However, given a lack of alternative dating methods, the current OSL ages are the only timing constraints of unit and event ages in the trench.

Samples sent to the Utah State University Luminescence laboratory (OSL samples 1B, 3 and 7 Fig. 3.5) are not expected to be received in time before the publication of this thesis. It is expected that these dates will verify results which have already been received and help further narrow the age ranges of paleo-earthquakes in the McLean's trench. They may also help clarify the difference in age between the ages of OSL-7 and RC-1.

The basal gravel of the McLean's trench represents the last major fan aggradation event, and as such is the best estimate of the S4 surface age mapped in chapter 2 (appendix 1). The later OSL ages obtained above these gravels probably reflect localised overbank flooding events from streams on the fans, and not major fan building episodes. These ages are on the younger end of the previously mapped < 71 ka age (i.e. Q4-Q2 ages from Rattenbury *et al.,* 2006).

Based on evidence for five earthquake events in the McLean's trench on The Humps fault, age constraints above and a recorded history of earthquakes in the area since 1850, the events can be age-bracketed in Table 3.4.

Table 3.4: Event history of McLean's Trench

Event number	Minimum age	Maximum age
5 (Kaikōura Earthquake)	Modern	Modern
4 ? (Possible Event) (penultimate)	1850	4610 ± 16 cal. Yr.
3	4610 ± 16 cal. Yr.	10.3 ± 1.0 ka
2	10.3 ± 1.0 ka	14.8 ± 1.4 ka
1 (multiple events)	15.1 ± 1.5 ka	Unknown

The frequency and consistency of paleoseismic events in the McLean's trench indicates a firmly established trend of faulting on this strand of The Humps Fault in the last 15 ka. Additionally, based on the uncertainty of the number of faults in event 1, there is probable evidence of faulting before 15.1 ka. Because of the epistemic and aleatory uncertainty in constraining event ages, it is difficult to say whether the recurrence interval of faulting has varied significantly through time. While Barrel & Townsend (2012) place the recurrence of The Humps Fault at approximately 13 ka, the results of the McLean's trench indicate a late Pleistocene to Holocene recurrence interval of at closer to half that value. Hyland-Brook (2018) indicates 2 events during the Holocene on the western-most tip of The Humps Fault, which appears to be consistent with these findings. Initial findings on the Chaffey trench indicate a penultimate event at ~5 ka (K. Pedley pers. comm., April 10, 2019) which would also be consistent with these findings of a possible event at McLean's trench between 1850 CE to 7.7 ± 0.7 ka.

3.7.2 Slip-rates on The Humps Fault

The fault sense of movement appears to have been consistent within the trench, and has produced a 3.5 m offset of the lowest gravel unit over a minimum of 15.1 ± 1.5 ka, suggesting a maximum vertical slip-rate of around 0.2 ± 0.02 mm/yr. The Harris site vertical slip-rate is negligible, this is possibly due to the sites position closer to the tip of the fault (Appendix 1) and additionally in the 2016 rupture the

site recorded no measurable vertical displacement. This may indicate the site does not usually produce a vertical offset during fault rupture, possibly an artefact of fault strike, or that anthropomorphic re-working of the site during farming operations has removed the fault scarp. The Aitken site vertical slip-rate was calculated to be between 0.02 - 0.10 mm/yr., which would place the McLean's site at a possibly higher vertical slip-rate. The McLean's site is on a single fault trace, with no parallel traces on which to divide slip, whereas the Aitken site is one of at least two branches of The Humps Fault (Appendix 1), meaning Aitkens may not be representative of the full vertical slip-rate. This number is close to the previously indicated number of 0.2 mm/yr. vertical slip-rate in literature (Barrell & Townsend 2012) and the slip-rate appears to be consistent with the slip-rates other faults in the region (Pettinga *et al.* 2001, Stirling *et al.* 2008, Barrell & Townsend 2012).

Horizontal slip-rates produced in this chapter include; the Harris slip-rate of 0.57 ± 0.1 mm/yr., at McLean's a rate of 0.49 ± 0.1 mm/yr. and at Aitken's between 0.1 - 0.4 mm/yr. The Aitken result is not representative of the whole fault, as it is a branch of the fault with at least one other parallel rupture in 2016, (appendix 1), and thus is a minimum for this section of the fault zone, which explains the lower value produced. Both the Harris and Aitken results are estimates based on inferred surface ages, these results will be substantially improved in accuracy when OSL results from February 2019 sampling are produced. Overall, horizontal slip-rates converge in the range of 0.6 – 0.4 mm/yr. over the late Pleistocene to Holocene. This low slip-rate combined with active Holocene deposition on the Emu Plains may help explain the underestimate of The Humps fault slip rate in geological surveys prior to 2016.

3.7.3 Wider implications of paleoseismic results

With over 20 faults rupturing in the November 2016 Kaikōura earthquake over two tectonic domains, one of the major questions that remains is how often Kaikōura-style events have occurred in the past— was the event a 'normal' earthquake for the faults involved, or a unique event in those faults' histories (Langridge *et al.* 2018). The answer to this question will be solved by producing paleoseismic histories of the faults involved in the Kaikōura earthquake and examining them to assess the probabilities of faults co-rupturing in the past.

Thus far, paleoseismic studies have not been completed for the majority of faults involved; however, the highly variable slip-rates and recurrence intervals of the faults ruptured based on geomorphic markers and landscape data would imply the exact fault make-up of the Kaikōura earthquake is not a regular occurrence through geological time (e.g. Litchfield et al., 2018). For example, one of the faults

near the northern tip of the rupture sequence, the Kekerengu fault, has been shown to have a Holocene recurrence interval of 376 ± 32 years (Little *et al.* 2018), which is at least an order of magnitude greater than the recurrence interval of The Humps Fault in this study. This lends further weight to the hypothesis that the exact sequence of faults is a rarity, however this does not preclude that ruptures on The Humps may have been historically linked to Kaikōura style multi-fault ruptures in the past.

Chapter 4. Conclusions

4.1.1 Summary of results

This thesis investigated the paleoseismicity on The Humps Fault and furthers our current understanding of active tectonics in the North Canterbury Tectonic Domain. Paleoseismic trenching, geomorphological mapping and differential LiDAR contribute to a more complete understanding of the history and nature of The Humps Fault and the Emu Plains.

Detailed fault mapping on multi-temporal LiDAR and aerial imagery revealed a series of distinct fault rupture sections across 18 km of the Emu Plains, approximately 2 km of which were mapped prior to 2016. Changes in fault geometry and style of deformation show six fault sections, of which four are dominantly right-lateral (Morses Road, Leslie Hills Road, Mason, Lottery), one left-lateral with a significant reverse component (Druids Road), and one shows a complex zone of intersecting Riedel shears and a primary dextral fault strand (Stackhouses Road). All of these sections of fault show evidence for past ground surface rupturing earthquakes, with LiDAR and aerial photography revealing fault scarps on the sites of the 2016 ruptures. Detailed surface mapping using higher resolution LiDAR reveals further refinements of surface age stratigraphy on the Emu Plains.

Paleoseismic trenching revealed a >15 ka chronology of faulting on The Humps Fault. A minimum of three pre-2016 event ages were constrained by OSL and ^{14}C ages and contribute to the first paleoseismic data on this fault. Future refinements to the model are expected, with three additional OSL samples currently being analysed. Slip-rates were calculated based on displaced geomorphic features of known age, based on geomorphic mapping of the Emu Plains. The slip rates from two separate sites are within the expected range for the North Canterbury Tectonic Domain.

4.1.2 Key findings

- Surface correlation and correlative stratigraphy results define seven Quaternary geomorphic surfaces on the Emu Plains based on high resolution topographic maps derived from LiDAR.
- Prior to the Kaikōura earthquake there is evidence for pre-existing fault scarps along much of the length of The Humps Fault within the Emu Plains. Fault scarps ranging in height from 0.1 m to 9 m were re-ruptured as part of the 2016 event. These fault scarps indicate multiple, recurring surface ruptures on The Humps Fault.

- Six fault Kaikōura earthquake rupture sections are defined on the Emu Plains, with displacements and sense of slip of these sections being dependent on their orientation relative to a regional PHS of approximately 120°.
- Paleoseismic trenching reveals evidence for a minimum of three past events on The Humps Fault prior to 2016, with some evidence for a possible fourth event as a penultimate event. These events can be constrained as having occurred at 1850 C.E. - 4610 ± 16 cal. Yr. (possible penultimate), an event between 4610 ± 16 cal. Yr. - 10.3 ± 1.0 ka, an event between 10.3 ± 1.0 - 14.8 ± 1.4 ka and an event (most likely multiple events) older than 15.1 ± 1.5 ka.
- Horizontal slip-rate results on the eastern half of The Humps Fault at studied sites include 0.57 ± 0.1 mm/year at Harris, 0.49 ± 0.1 mm/year at McLean's and between 0.1 - 0.4 mm/year at Aitken's (Appendix 1).
- Vertical slip-rate results on the eastern half of The Humps Fault at studied sites include a maximum of 0.2 ± 0.02 mm/year at McLean's and between 0.02 and 0.1 mm/year at Aitkens (Appendix 1)

4.1.3 Future work

Currently very little is known about the cumulative basement offset of The Humps Fault, and how the surface expression of the fault in the Culverden Basin may be tied to subsurface basement expression of the fault. Basement offset may reveal The Humps relationship and initiation timing to the bounding faults of the Culverden Basin, and how it has interacted with the Leader Fault in the uplift of Mt. Stewart.

Pending OSL results from the McLean's Trench (Fig. 3.5) will help narrow the age and recurrence of earthquake events. Pending OSL sample results from the Aitken and Harris slip-rate investigation sites will reduce the uncertainty of the slip-rate results significantly and produce further refinements to surface age dating of the Emu Plains. Future work might focus on (i) producing slip-rate through time models for The Humps Fault and (ii) producing along-strike or along-segment variability in slip rates.

Further investigations on The Humps Fault are underway within the University of Canterbury, with a paleoseismic trench excavated in the February of 2019 at the "Dalmer" site (Appendix 1). These findings will be complimented by results from the "Chaffey" trench (location shown in Appendix 1). Further confirmation and refinement of the slip-rate results is expected, with OSL samples taken in February of 2019 to constrain the ages of the geomorphic features in question.

To assess how often Kaikōura style events have occurred in the past, more data is required on the paleoseismicity of all faults involved in the 2016 earthquake and perhaps peripheral North Canterbury

faults, which may have co-ruptured in the past. This overarching dataset could help forward knowledge of multi-fault ruptures, and the role they play in collisional tectonic zones, as well as how often they might be under- or over-represented in the paleoseismic record.

References

Armstrong, M. 2000: Geomorphological and geophysical investigation of the effects of active tectonic deformation on the hydrogeology of north Culverden Basin, North Canterbury. PhD thesis, Department of Geological Sciences, University of Canterbury, Christchurch.

Barnes, P.M., Mercier de Lépinay B., Collot J.Y., Delteil J., Audru J.C. 1998: Strain partitioning in the transition area between oblique subduction and continental collision, Hikurangi margin, New Zealand. Tectonics, 17, 534–557.

Barrell, D.J.A. and Townsend, D.B. 2012. General distribution and characteristics of active faults and folds in the Hurunui District, North Canterbury. *GNS Science Consultancy Report* 2012/113.

Buchanan, J. 1868: Kaikōura district. New Zealand Geological Survery report of geological explorations 4: 24-41.

Cesca, S., Zhang, Y., Mouslopoulou, V., Wang, R., Saul, J., Savage, M., Heimann, S., Kufner, S., Oncken, O., Dahm, T. 2017: Complex rupture process of the Mw 7.8, 2016, Kaikoura earthquake, New Zealand, and its aftershock sequence. Earth and planetary science letters. 478: 110-120.

Clayton, L. 1968: Late Pleistocene glaciations of the Waiau Valleys, North Canterbury. New Zealand Journal of Geology and Geophysics. 11. 753-767.

Cowan, H.A. 1989: An Evaluation of the Late Quaternary Displacements and Seismic Hazard Associated with The Hope and Kakapo Faults, Amuri District, North Canterbury. Master of Science (Geology). University of Canterbury.

Cowan, H.A. 1990: Late Quaternary displacements on the Hope Fault at Glynn Wye, North Canterbury. New Zealand Journal of Geology and Geophysics 33: 285–293.

Cowan, H.A. 1992: 'Structure, seismicity and tectonics of the Porter's Pass-Amberley fault zone, North Canterbury, New Zealand'. PhD thesis, University of Canterbury, Christchurch.

Cox, S.C., Stirling, M.W., Herman, F., Gerstenberger, M., Ristau, J. 2012: Potentially active faults in the rapidly eroding landscape adjacent to the Alpine Fault, central Southern Alps, New Zealand. Tectonics, 31.

Cubrinovski, M., Bray, J.D., de la Torre, C., Olsen, M., Bradley, B., Chiaro, G., Krall, T. 2018: Liquefaction-Induced Damage and CPT Characterization of the Reclamations at CentrePort, Wellington. Bulletin of the Seismological Society of America, 108(3B), 1695-1708.

DeMets, C., Gordon R.G., Argus D.F. 2010: Geologically current plate motions. Geophysical Journal International 181, 1-80.

Endharto, M.A. 1987: Upper Cretaceous-tertiary geology of the Wandle river-Whales Back area, Northern Waiau, North Canterbury. Masters thesis, University of Canterbury, Christchurch.

Freund, R. 1971: The Hope Fault, a strike slip fault in New Zealand. New Zealand Geological Survey bulletin, 1971. Volume 86.

Gregg, R.C. 1965: The pre-Quaternary geology of an area around Waiau, North Canterbury. Masters thesis, University of Canterbury, Christchurch.

Hamling, I.J., Hreinsdóttir, S., Clark, K., Elliott, J., Liang, C., Fielding, E., Litchfield, N., Villamor, P., Wallace, T., Wright, J. 2017: Complex multifault rupture during the 2016 Mw 7.8 Kaikōura earthquake, New Zealand. Science, 356 no. 6334

Holt, W.E., and Haines A.J. 1995: The kinematics of northern South Island, New Zealand, determined from geological strain rates. Journal of Geophysical Research, vol 100(B9), 17,991–918,010.

Kaiser A., Balfour, N., Fry B., Holden C., Litchfield N., Gerstenberger M., D'Anastasio E., Horspool N., McVerry G., Ristau J., Bannister S., Christophersen A., Clark K., Power W., Rhoades D., Massey C., Hamling I., Wallace L., Mountjoy J., Kaneko Y., Benites R., Van Houtte C., Dellow S., Wotherspoon L., Elwood K., Gledhill K. 2017: The 2016 Kaikōura, New Zealand, Earthquake: Preliminary Seismological Report. Seismological Research Letters, vol 88(3), 727-739.

Kearse, J., Little, T.A., Van Dissen, R.J., Barnes, P., Langridge, R., Mountjoy, J., Ries, Villamor, P., Clark, K.J., Benson, A., Lamarche, G., Hill, M., Hemphill-Haley, M. 2018: Onshore to Offshore Ground-Surface and Seabed Rupture of the Jordan–Kekerengu–Needles Fault Network during the 2016 Mw 7.8 Kaikōura Earthquake, New Zealand. Bulletin of the Seismological Society of America, 108(3B), 1573-1595.

Khajavi, N., Quigley, M., Langridge R. 2014: Influence of topography and basement depth on surface rupture morphology revealed from LiDAR and field mapping, Hope fault, New Zealand. Tectonophysics V 630, 265–284.

Khajavi, N., Nicol, A., Quigley, M.C., Langridge, R.M. 2018: Temporal slip-rate stability and variations on the Hope Fault, New Zealand, during the late Quaternary. Tectonophysics, 738-739, 112-123.

Langridge, R., Campbell, J., Hill, N., Pere, V., Pope, J., Pettinga, J., Estrada, E., Berryman K. 2003: Paleoseismology and slip rate of the Conway segment of the Hope fault at Greenburn Stream, South Island, New Zealand, Ann. Geophys. 46, 1119–1139.

Langridge, R., Ries, W.F., Litchfield, N., Villamor, P., Van Dissen, R.J., Barrell, D.J.A., Rattenbury, M.S., Heron, D.W., Haubrock, S., Townsend, D.B., Lee, J.M., Berryman, K.R., Nicol, A., Cox, S.C., Stirling, M.W., 2016: The New Zealand Active Faults Database. New Zealand Journal of Geology and Geophysics, 59(1), 86-96.

Langridge, R., Van Dissen, R.J., Nicol, A., Pettinga, J., Stirling, M., Barrell, D., Almond, P., Williams, J., Stahl, T., Pedley, K., Brough, T., 2018: Paleoseismicity of 2016 Mw 7.8 Kaikōura Earthquake faults: Was this event the Norm or one "out of the park"? In: Sagar M, Prebble J ed. Abstract Volume: Geosciences 2018, Napier, New Zealand. Geoscience Society of New Zealand Miscellaneous Publication 151A. p 123.

Litchfield, N.J., Van Dissen, R., Sutherland, R., Barnes, P.M., Cox, S.C., Norris, R., Beavan, R., Langridge, R.,P., Villamor, P. 2014: A model of active faulting in New Zealand. New Zeal. J. Geol. Geophys., 57, 32-56.

Litchfield N.J., Villamor, P., Van Dissen, R.J., Nicol, A., Barnes, P.M., Barrell, D.J.A., Pettinga, J.R., Langridge R.M., Little T.A., Mountjoy J.J., Ries W.F., Rowland J., Fenton C., Stirling M.W., Kearse J., Berryman K.R., Cochran U.A., Clark K.J., Hemphill-Haley M., Khajavi N., Jones K.E., Archibald G., Upton P., Asher C., Benson A., Cox S.C., Gasston C., Hale D., Hall B., Hatem A.E., Heron D.W., Howarth J., Kane T.J., Lamarche G., Lawson S., Lukovic B., McColl S.T., Madugo C., Manousakis J., Noble D., Pedley K., Sauer K., Stahl T., Strong D.T., Townsend D.B., Toy V., Williams J., Woelz S., Zinke R. 2018: Surface Rupture of Multiple Crustal Faults in the 2016 Mw 7.8 Kaikōura, New Zealand, Bulletin of the Seismological Society of America, 108(3B), 1496-1520.

Little, T.A., Van Dissen, R., Kearse, J., Norton, K., Benson, A., Wang, N., 2018: Kekerengu Fault, New Zealand: Timing and Size of Late Holocene Surface Ruptures. Bulletin of the Seismological Society of America. 108 (3B): 1556–1572.

Manighetti, I., Campillo, M., Bouley, S., Cotton, F., 2007: Earthquake scaling, fault segmentation, and structural maturity. Earth Planet. Science Letters. 253, 429–438.

Mason, B.H. 1949: The geology of the Mandamus-Pahau District, North Canterbury. Transactions of the Royal Society of New Zealand. 77, 403–428.

Massey, C., Townsend D.B., Rathje Y., Kaneko B., Lukovic N., Horspool B., Bradley I., Hamling J., Wartman K., Allstadt J. *et al.* 2018: Landslides triggered by the Mw 7.8 14 November 2016 Kaikōura Earthquake, New Zealand. Bulletin Seismolological Society America.

McKay, A., 1888: Remarks on the earthquakes in the Amuri. Transactions of the NZ. lnstitute 21: 508- 509.

McMorran, T.J. 1991: The Hope Fault at Hossack Station east of Hanmer Basin, North Canterbury. Master of Science (Engineering Geology). University of Canterbury.

Ministry of Transport. 2017: Economic impact of the 2016 Kaikōura earthquake: A report prepared for the Ministry of Transport. Internal report prepared by the ministry, Auckland, New Zealand.

Mould, R. 1992: Structure and Kinematics of Late Cenozoic Deformation along the Western Margin of the Culverden Basin, North Canterbury, New Zealand. Masters thesis, University of Canterbury, Christchurch.

Nicol A. and Wise, D.U. 1992: Paleostress adjacent to the Alpine Fault of New Zealand: vein and stylolite data from the Doctors Dome area. Journal of Geophysics Research 97.

Nicol, A. 1993: Haumurian (c 66–80 Ma) half graben, Mid Waipara, North Canterbury and its implication for Late Cretaceous deformation in New Zealand. New Zealand Journal of Geology and Geophysics, 36, 127–130.

Nicol A., Brent, A., Tonkin P. 1994: Rates of deformation, uplift and landscape development associated with active folding in the Waipara area of North Canterbury, New Zealand. Tectonics, 13, 1327–1344.

Nicol A., Pettinga J.R., Fenton C., Stahl T., Bannister S., Pedley K., Hyland-Brook N., Bushell T., Hamling I., Ristau J., Noble D., McColl S.T. 2018: Preliminary Geometry, Displacement, and Kinematics of Fault Ruptures in the Epicentral Region of the 2016 Mw 7.8 Kaikōura, New Zealand, Earthquake. Bulletin of the Seismological Society of America, 108(3B), 1521-1539.

Noble, D.P. 2011: Tectonic geomorphology and paleoseismicity of the Northern Esk Fault, North Canterbury, New Zealand. Masters thesis, University of Canterbury, Christchurch.

Pearson, C.F., Beavan, J., Darby, D.J., Blick, G.H., Walcott, R.I. 1995: Strain distribution across the Australian-Pacific plate boundary in the central South Island, New Zealand, from 1992 GPS and earlier terrestrial observations. J. Geophys. Res. 100, no. B11. 22071–22081.

Pettinga, J.R., Yetton, M.D., Van Dissen, R.J., Downes, G.L. 2001: Earthquake source identification and characterisation for the Canterbury region, South Island, New Zealand. Bulletin of the New Zealand Society for Earthquake Engineering 34: 282–317.

Pondard, N., and P. M. Barnes. 2010: Structure and paleoearthquake records of active submarine faults, Cook Strait, New Zealand: Implications for fault interactions, stress loading, and seismic hazard. J. Geophys. Res., 115(B12320).

Rattenbury, M.S., Townsend, D.B. and Johnston, M.R. 2006: Geology of the Kaikōura area. Institute & Geological and Nuclear Sciences 1:250,000 Geological Map. Lower Hutt, New Zealand

Stirling, M., Gerstenberger, M., Litchfield, N., McVerry, G., Smith, W., Pettinga, J., Barnes, P. 2008: Seismic hazard of the Canterbury Region, New Zealand: new earthquake source model and methodology. Bulletin of the New Zealand Society for Earthquake Engineering 41: 51–67.

Stirling, M., Litchfield, N., Villamor, P., Van Dissen, R.J., Nicol, A., Pettinga, J., Barnes, P., Langridge, R.M., Little, T., Barrell D.J.A., *et al.* 2017: The Mw 7.8 2016 Kaikōura earthquake: Surface fault rupture and seismic hazard context. Bull. New Zeal. Soc. Earthquake Eng., 50(2), 73–84.

Speight, R. 1918: Structure and Glacial Features of the Hurunui Valley. Transactions of the New Zealand Institute, 50, 93–105.

Timm, C., Davy, B., Haase, K., Hoernle, K., Graham, I., de Ronde, Cornel., Woodhead, J., Bassett, D., Hauff, F., Mortimer, N., Seebeck, H., Wysoczanski, R., Caratori-Tontini, F., Gamble, J., 2014: Subduction of the oceanic Hikurangi Plateau and its impact on the Kermadec arc. Nature Communications volume 5, Article number: 4923.

Wallace, L.M., Barnes, P., Beavan, J., Van Dissen, R., Litchfield, N., Mountjoy, J., Langridge R., Lamarche G., Pondard, N. 2012: The kinematics of a transition from subduction to strike-slip: An example from the central New Zealand plate boundary. Journal of Geophysical Research, 117.

Wallace, L.M., Barnes P., Beavan J., Van Dissen R., Litchfield N., Mountjoy J., Langridge R., Lamarche G., Pondard, N. 2012: The kinematics of a transition from subduction to strike-slip: An example from the central New Zealand plate boundary. J. Geophysical Research, 117(B02405).

Wallace, L.M., Beaven, J., McCaffrey, R., Berryman, K., Denys, P. 2007: Balancing the plate motion budget in the South Island, New Zealand using GPS, geological and seismological data. Geophysical Journal International, 168(1), 332-352.

Wesnousky, S.G. 1988: Seismological and structural evolution of strike-slip faults. Nature 335, 340–343.

Williams, A., Burns, D., Farqhuar, G., Mills, M. 2005: Field description of soil and rock. Guideline for the field classification and description of soil and rock for engineering purposes. NZ Geotechnical Society INC.

Williams, J., Barrell, D., Stirling, M., Sauer, K., Duke, G., Hao, K. 2018: Surface Rupture of the Hundalee Fault during the 2016 Mw 7.8 Kaikōura Earthquake. Bulletin of the Seismological Society of America. 108 (3B): 1540–1555

Wilson, D.D. 1963: The Geology of the Waipara Subdivison. New Zealand Geological Survey Bulletin 64.

Zinke, R., Dolan, J.F., Van Dissen, R., Grenader, J.R., Rhodes, E.J., McGuire, C.P., Langridge, R.M., Nicol, A., Hatem, A.E. 2015: Evolution and progressive geomorphic manifestation of surface faulting: A comparison of the Wairau and Awatere faults, South Island, New Zealand. Geology 43, 1019–1022.

Appendices

Appendix 1: Fault ruptures and paleoseismic investigation map of the Emu Plains

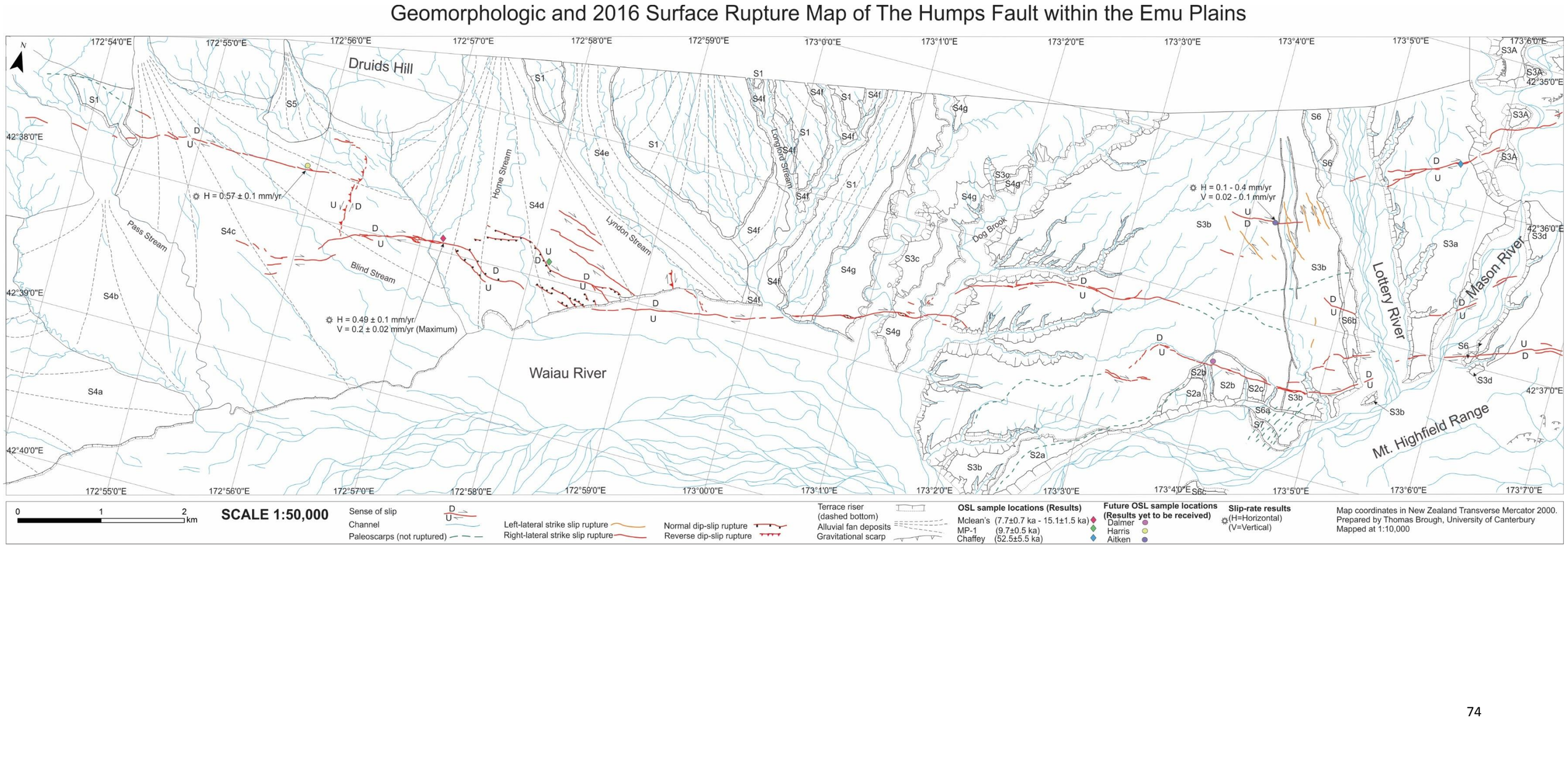

Appendix 2: OSL lab report for sample location MP-1

Report No. 5/18

Luminescence Dating Technical Report

Luminescence Dating Laboratory

School of Geography, Environment and Earth Sciences

Victoria University of Wellington

Wellington New Zealand

Reported by: Ms. Ningsheng Wang

Date of Issue: 06-04-2018

Contact: Room 414

Cotton Building

Victoria University of Wellington

Ph: (04) 463 6127

CONTENTS

1. SUMMARY

One sample (Field code: MP-1) was submitted for luminescence dating by Dr. Narges Khajavi, Department of Geology, University of Canterbury. The laboratory codes of the samples is WLL1282.

The fine grain (4-11µm) preparation technique was used. The blue luminescence was measured during infrared stimulation of fine grain feldspar. The luminescence ages were determined by Single Aliquot Regenerative method (SAR). The dose rate was determined on the basis of ICP-MS.

2. SAMPLE PREPARATION

The sample preparation consisted of two parts:

(i) Preparation for measurement of equivalent dose (equivalent to the paleodose) (ii) Preparation for measurement of dose rate

Part 1: The Preparation for Measurement of Equivalent Dose (D_e)

1. Chemical Treatment

Samples had their outer surfaces removed. Of this removed outer scrapings, 100g was weighed and dried in an oven in preparation for gamma spectrometer analysis. A plastic cube was then filled with remaining scrapings in preparation for water content measuring.

"Fresh" sample material, that had outer surfaces removed earlier (unexposed light sample material), was treated in 10% HCl. This was carried out overnight until all carbonate was removed by the reaction. Following this treatment the sample was further reacted overnight with 10% H_2O_2 in order to remove organic matter.

The next step involved 200ml CBD* solution being added to the sample for 12 hours to remove iron oxide coatings. Note, after every chemical treatment procedure distilled water was used to wash the sample several times.

*CBD solution: 71g sodium citrate, 8.5 g sodium bicarbonate, and 2g sodium dithionate per litre of distilled water

2. Fine Grain Technique (4-11μm)

After chemical treatment, calgon solution (1g sodium hexametaphosphate per litre distilled water) was added to make thick slurry. This slurry was placed into an ultrasonic bath and mechanically agitated for an hour. The sample was then placed into a 1L measuring cylinder, filled with a certain amount of distilled water to separate out the 4-11μm grains according to Stokes' Law.

The 4-11μm grains were then rinsed with ethanol and acetone and a suspension of these grains were then deposited evenly onto 70 aluminium disks.

Part 2: The Preparation of Measurement of Dose Rate

The dry, ground and homogenised sample materials were submitted to the Geochemistry Laboratory, Victoria University of Wellington for the determination of ^{238}U, ^{232}Th and ^{40}K contents by ICP-MS

3. MEASUREMENTS

Luminescence age was determined by two factors: the equivalent dose (D_e) and the dose rate.

Equivalent dose: obtained from the lab equivalents to the paleodose absorbed by samples during the burial time in the natural environment since their last exposure to the light. Dose rate: amount dose received by the sample each year.

Part 1: Determination of Equivalent Dose (D_e)

D_e was obtained by using SAR.

Single Aliquot Regenerative Method (SAR)

The Single Aliquot Regenerative Method (SAR) was used to determine the equivalent doses. This technique is described by Murray and Wintle (2000).

For the SAR method, a number of aliquots (disks) were subjected to a repetitive cycle of irradiation, preheating and measurement. Firstly, natural shining down curves was measured after preheating. Then shining down curves were measured for the next four or five cycles for different beta doses. Then from the variety of shining down curves, a luminescence growth curve (β induced luminescence versus added dose) was established. This was used to determine the equivalent dose (equivalent to the palaeodose). The measurement for the aliquots resulted in a variety of equivalent doses, so called dose distribution. D_e given in the report were used the arithmetic mean of the data.

In order to correct potential sensitivity changes from cycle to cycle, the luminescence response to a test dose was measured after preheat between cycles.

The blue luminescence of 12 aliquots of the sample were measured at 50^0C for 100s using a Riso TL-DA-20 reader with infrared diodes at 880nm used to deliver a stimulated beam. Blue luminescence centre about 410nm from feldspar was then detected by an EMI 9235QA photomultiplier fixed behind two filters consisting of a Schott BG39 and Kopp5-58. Beta irradiation were done on the Riso TL-DA-20

^{90}Sr/Y β irradiator, calibrated against ^{60}Co gamma source, SFU, Vancouver, Canada with about 3% uncertainty. Preheat and cut heat temperature was 260 ^{o}C for 10 seconds.

Luminescence growth curve (β induced luminescence intensity versus added dose) was constructed by using the initial the first a few seconds of the shine down curves and subtracting the average of the last 20 seconds, along with the so called late light which was thought to be a mixture of background and hardly bleachable components. Interpolation of this growth curve to the dose axis was yielded the equivalent dose D_e which was used as a paleodose. The measurements of 12 aliquots obtained 12 D_e's, the D_e's were accepted within max recapture ratio 10%. Recycling ratio has to increase to 40%. Due to the high recycling ratio, the experiment of the recovering the dose was tested and the value of the given dose can be recovered, so D_e is considered to be reliable. D_e used for the age determination was used for the arithmetic means of the data. A dose recovery test and a zero dose were checked no anomalies.

Fading was checked, no fading tendency was observed.

a-value a-value is measured by comparing the luminescence induced by alpha irradiation with that induced by beta or gamma irradiation. The a-value was for dose rate calculation. For this study, a-value was estimated.

Part 2: Determination of Dose Rate

Dose rate consisted of two parts.

(i) Dose rate from sample's burial environment (ii) Dose rate from cosmic rays.

(i) Dose rate from burial environment

Dose rate from sample's burial environment was determined by radionuclide contents of ^{238}U, ^{232}Th and ^{40}K, and water content.

Determination of Contents of ^{238}U, ^{232}Th and ^{40}K by the Thermo Finnigan Element 2 ICP-MS

Contents of ^{238}U, ^{232}Th and ^{40}K were measured at the Geochemical Laboratory, Victoria University of Wellington. It was assumed that these samples are homogenise and radionuclide are equilibrium. The dose rate calculation was based on the activity concentration of the nuclides ^{238}U, ^{232}Th and ^{40}K, and using dose rate conversion factors published by Guérin, G., Mercier, N., Adamiec, G. (2011).

Measurement of Water Contents

Water content was measured as weight of water divided by dry weight of the sample taking into account a 25% uncertainty.

(ii) Dose rate from cosmic rays

Dose rate from cosmic rays were determined by the depth of sample below the surface along with its longitude, latitude and altitude, convention formula and factors published by Prescott, J.R. & Hutton, J.T. (1994).

4. RESULTS

Table 1 Cosmic dose rates

Table 2 Water contents, radionuclide contents

Table 3 a- Values, equivalent doses, dose rates and luminescence ages

Table 1: Cosmic Dose Rates

Laboratory Code	Depth Below the Surface(m)	Cosmic Dose Rate (Gy/ka)	Field Code
WLL1282	0.60	0.1977±0.0099	MP1

Table 2: Water Contents, Radionuclide Contents

Laboratory Code	Water Content (%)	^{238}U(ppm)	^{232}Th(ppm)	K(%)	Field Code
WLL1282	12.5	1.59±0.02	5.89±0.05	1.85±0.05	MP1

Table 3: a-Values, Equivalent Doses, Dose Rates and Luminescence Ages

Laboratory Code	a-value*	D_e(Gy)	Dose Rate(Gy/ka)	Luminescence Age(ka)	Field Code
WLL1282	0.06±0.02	29.31±0.23	3.02±0.16	9.7±0.5	MP1

*a-value was estimated.

5. REFERENCES

Guérin, G., Mercier, N., Adamiec, G. 2011: Dose- rate conversion factors: update.

Ancient TL, Vol.29, No.1, 5-8.

Murray, A.S. & Wintle, A.G. 2000: Luminescence dating of quartz using an improved single aliquot regenerative dose protocol. Radiation Measurements 32, 57-73.

Prescott, J.R. & Hutton, J.T. 1994: Cosmic ray contributions to dose rates for luminescence and ESR dating: Large depths and long-term time variations.

Radiation Measurements. Vol.23,Nos.2/3, 497-500.

Appendix 3: OSL lab report for McLean's trench

Report No. 9/18

Luminescence Dating Technical Report

Luminescence Dating Laboratory

School of Geography, Environment and Earth Sciences

Victoria University of Wellington

Wellington New Zealand

Reported by: Ms. Ningsheng Wang

Date of Issue: 21-06-2018

Contact: Room 414

Cotton Building

Victoria University of Wellington

Ph: (04) 463 6127

CONTENTS

1. SUMMARY

Seven samples (Field code: Mclean OSL Sample1, Mclean OSL Sample 4, Mclean OSL Sample 5, Mclean OSL Sample 7, Chaffey OSL Sample 2, Chaffey OSL Sample 4 and Chaffey OSL Sample 8) were submitted for luminescence dating by Professor Andy Nicol, University of Canterbury. The laboratory codes of the samples are WLL1297-WLL1303 respectively.

The fine grain (4-11μm) preparation technique was used. The blue luminescence was measured during infrared stimulation of fine grain feldspar. The luminescence ages were determined by Single Aliquot Regenerative method (SAR). The dose rate was determined on the basis of gamma spectrometry measurements.

2. SAMPLE PREPARATION

The sample preparation consisted of two parts:

(i) Preparation for measurement of equivalent dose (equivalent to the paleodose) (ii) Preparation for measurement of dose rate

Part 1: The Preparation for Measurement of Equivalent Dose (D_e)

1. Chemical Treatment

Samples had their outer surfaces removed. Of this removed outer scrapings, 100g was weighed and dried in an oven in preparation for gamma spectrometer analysis. A plastic cube was then filled with remaining scrapings in preparation for water content measuring.

"Fresh" sample material, that had outer surfaces removed earlier (unexposed light sample material), was treated in 10% HCl. This was carried out overnight until all carbonate was removed by the reaction. Following this treatment the sample was further reacted overnight with 10% H_2O_2 in order to remove organic matter.

The next step involved 200ml CBD* solution being added to the sample for 12 hours to remove iron oxide coatings. Note, after every chemical treatment procedure distilled water was used to wash the sample several times.

*CBD solution: 71g sodium citrate, 8.5 g sodium bicarbonate, and 2g sodium dithionate per litre of distilled water

2. Fine Grain Technique (4-11µm)

After chemical treatment, calgon solution (1g sodium hexametaphosphate per litre distilled water) was added to make thick slurry. This slurry was placed into an ultrasonic bath and mechanically agitated for an hour. The sample was then placed into a 1L measuring cylinder, filled with a certain amount of distilled water to separate out the 4-11µm grains according to Stokes' Law.

The 4-11µm grains were then rinsed with ethanol and acetone and a suspension of these grains were then deposited evenly onto 70 aluminium disks.

Part 2: The Preparation of Measurement of Dose Rate

The dry, ground and homogenised sample material were weighed and sealed in air tight perspex containers and stored for at least four weeks. This storage time minimizes the loss of the short lived noble gas ^{222} Rn and allows ^{226}Ra to reach equilibrium with its daughters ^{214} Pb and ^{214} Bi.

3. MEASUREMENTS

Luminescence age was determined by two factors: the equivalent dose (D_e) and the dose rate.

Equivalent dose: obtained from the lab equivalents to the paleodose absorbed by samples during the burial time in the natural environment since their last exposure to the light. Dose rate: amount dose received by the sample each year.

Part 1: Determination of Equivalent Dose (D_e)

D_e was obtained by using SAR.

Single Aliquot Regenerative Method (SAR)

The Single Aliquot Regenerative Method (SAR) was used to determine the equivalent doses. This technique is described by Murray and Wintle (2000).

For the SAR method, a number of aliquots (disks) were subjected to a repetitive cycle of irradiation, preheating and measurement. Firstly, natural shining down curves was measured after preheating. Then shining down curves were measured for the next four or five cycles for different beta doses. Then from the variety of shining down curves, a luminescence growth curve (β induced luminescence versus added dose) was established. This was used to determine the equivalent dose (equivalent to the palaeodose). The measurement for the aliquots resulted in a variety of equivalent doses, so called dose distribution. D_e given in the report were used the arithmetic mean of the data with standard error.

In order to correct potential sensitivity changes from cycle to cycle, the luminescence response to a test dose was measured after preheat between cycles.

The blue luminescence of 12 aliquots of each sample were measured at 50^0C for 100s using a Riso TL-DA-20 reader with infrared diodes at 880nm used to deliver a stimulated beam. Blue luminescence centre about 410nm from feldspar was then detected by an EMI 9235QA photomultiplier fixed behind two filters consisting of a Schott BG39 and Kopp5-58. Beta irradiation were done on the Riso TL-DA-20

^{90}Sr/Y β irradiator, calibrated against ^{60}Co gamma source, SFU, Vancouver, Canada with about 3% uncertainty. Preheat and cut heat temperature was 260 ^{o}C for 10 seconds.

Luminescence growth curve (β induced luminescence intensity versus added dose) was constructed by using the initial the first a few seconds of the shine down curves and subtracting the average of the last 20 seconds, along with the so called late light which was thought to be a mixture of background and hardly bleachable components. Interpolation of this growth curve to the dose axis was yielded the equivalent dose D_e which was used as a paleodose. The measurements of 12 aliquots obtained 12 D_e's, the D_e's were accepted within 10% recycling ratio. D_e used for the age determination was used the arithmetic means of the data. A dose recovery test and a zero dose were checked no anomalies.

Fading was tested, fading is not observed.

a-value a-value is measured by comparing the luminescence induced by alpha irradiation with that induced by beta or gamma irradiation. The a-value was for dose rate calculation. For this study, a-value was estimated.

Part 2: Determination of Dose Rate

Dose rate consisted of two parts.

(i) Dose rate from sample's burial environment (ii) Dose rate from cosmic rays.

(i) Dose rate from burial environment

Dose rate from sample's burial environment was determined by radionuclide contents of ^{238}U, ^{232}Th and ^{40}K, a-value and water content.

Determination of Contents of U, Th and K by Gamma spectrometry

Gamma rays produced from sample material was counted for a minimum time of 24 hours by a high resolution and broad energy gamma spectrometer. The spectra were then analysed using GENIE2000 software. The contents of U, Th and K were obtained by comparison with standard samples. The dose rate calculation was based on the activity concentration of the nuclides ^{40} K, ^{208}Tl, ^{212}Pb, ^{228} Ac, ^{214} Bi, ^{214}Pb, ^{226} Ra, using dose rate conversion factors published by Guérin, G., Mercier, N., Adamiec, G. 2011.

Measurement of Water Contents

Water content was measured as weight of water divided by dry weight of the sample taking into account a 25% uncertainty.

(ii) Dose rate from cosmic rays

Dose rate from cosmic rays were determined by the depth of sample below the surface along with its longitude, latitude and altitude, convention formula and factors published by Prescott, J.R. & Hutton, J.T. (1994).

4. RESULTS

Table 1 Cosmic dose rates

Table 2 Water contents, radionuclide contents

Table 3 a- Values, equivalent doses, dose rates and luminescence ages

Table 1: Cosmic Dose Rates

Laboratory Code	Depth Below the Surface(m)	Cosmic Dose Rate (Gy/ka)	Field Code
WLL1297	3.3	0.1377±0.0069	Mclean OSL Sample 1
WLL1298	1.3	0.1794±0.0090	Mclean OSL Sample 4
WLL1299	1.0	0.1870±0.0093	Mclean OSL Sample 5
WLL1300	0.6	0.1977±0.0099	Mclean OSL Sample 7
WLL1301	2.0	0.1662±0.0083	Chaffey OSL Sample 2
WLL1302	1.3	0.1827±0.0091	Chaffey OSL Sample 4
WLL1303	0.4	0.2070±0.0103	Chaffey OSL Sample 8

Table 2: Water Contents, Radionuclide Contents

Laboratory Code	Water Content (%)	U(ppm) from ^{234}Th	U(ppm) from ^{226}Ra, ^{214}Pb, ^{214} Bi	U(ppm) from ^{210}Pb	Th(ppm) From ^{208}Tl ^{212} Pb ^{228} Ac	K(%)	Field Code
WLL1297	19.3	2.89±0.34	3.15±0.17	3.07±0.27	10.53±0.12	1.89±0.04	Mclean OSL Sample 1
WLL1298	20.3	2.47±0.32	2.42±0.16	2.94±0.27	10.12±0.12	1.89±0.04	Mclean OSL Sample 4
WLL1299	19.2	2.85±0.34	2.87±0.17	2.12±0.25	9.50±0.12	1.95±0.04	Mclean OSL Sample 5
WLL1300	15.6	2.05±0.31	2.24±0.16	1.91±0.24	7.93±0.10	1.86±0.04	Mclean OSL Sample 7
WLL1301	23.1	2.19±0.30	2.58±0.16	2.74±0.26	8.96±0.11	1.40±0.03	Chaffey OSL Sample 2
WLL1302	24.3	2.93±0.36	3.28±0.19	3.22±0.30	11.46±0.14	1.59±0.03	Chaffey OSL Sample 4
WLL1303	16.7	2.87±0.33	2.81±0.17	2.66±0.26	8.77±0.11	1.33±0.03	Chaffey OSL Sample 8

Table 3: a-Values, Equivalent Doses, Dose Rates and Luminescence Ages

Laboratory Code	*a-value	D_e(Gy)	Dose Rate(Gy/ka)	Luminescence Age(ka)	Field Code
WLL1297	0.06±0.03	55.96±0.80	3.71±0.37	15.1±1.5	Mclean OSL Sample 1
WLL1298	0.06±0.03	51.20±0.41	3.46±0.32	14.8±1.4	Mclean OSL Sample 4
WLL1299	0.06±0.03	37.48±0.24	3.64±0.34	10.3±1.0	Mclean OSL Sample 5
WLL1300	0.06±0.03	25.81±0.15	3.34±0.28	7.7±0.7	Mclean OSL Sample 7
WLL1301	0.06±0.03	152.87±0.99	2.89±0.30	52.9±5.5	Chaffey OSL Sample 2
WLL1302	0.06±0.03	142.68±1.51	3.46±0.37	41.2±4.5	Chaffey OSL Sample 4
WLL1303	0.06±0.03	23.51±0.17	3.11±0.31	7.6±0.8	Chaffey OSL Sample 8

*a-value was estimated.

5. REFERENCES

Guérin, G., Mercier, N., Adamiec, G. 2011: Dose- rate conversion factors: update.

Ancient TL, Vol.29, No.1, 5-8.

Murray, A.S. & Wintle, A.G. 2000: Luminescence dating of quartz using an improved single aliquot regenerative dose protocol. Radiation Measurements 32, 57-73.

Prescott, J.R. & Hutton, J.T. 1994: Cosmic ray contributions to dose rates for luminescence and ESR dating: Large depths and long-term time variations.

Radiation Measurements. Vol.23,Nos.2/3, 497-500.

THE UNIVERSITY OF
WAIKATO
Te Whare Wānanga o Waikato

Private Bag 3105
Hamilton,
New Zealand.
Ph +64 7 838 4278
email c14@waikato.ac.nz

Tuesday, 24 April 2018

Radiocarbon Dating Laboratory

Report on Radiocarbon Age Determination for Wk- 47373

Submitter	A Nicol
Submitter's Code	McClean MC-1
Site & Location	McClean trench, Leslie Hills Road, New Zealand
Sample Material	Charcoal
Physical Pretreatment	Sample cleaned.
Chemical Pretreatment	Sample washed in hot HCl, rinsed and treated with multiple hot NaOH washes. The NaOH insoluble fraction was treated with hot HCl, filtered, rinsed and dried.

$D^{14}C$	-400.2 ± 1.2 ‰
$F^{14}C$%	60.0 ± 0.1 %
Result	**4106 ± 16 BP**

(AMS measurement)

Comments

Please note: The Carbon-13 stable isotope value ($\delta^{13}C$) was measured on prepared graphite using the AMS spectrometer. The radiocarbon date has therefore been corrected for isotopic fractionation. However the AMS-measured $\delta^{13}C$ value can differ from the $\delta^{13}C$ of the original material and it is therefore not shown.

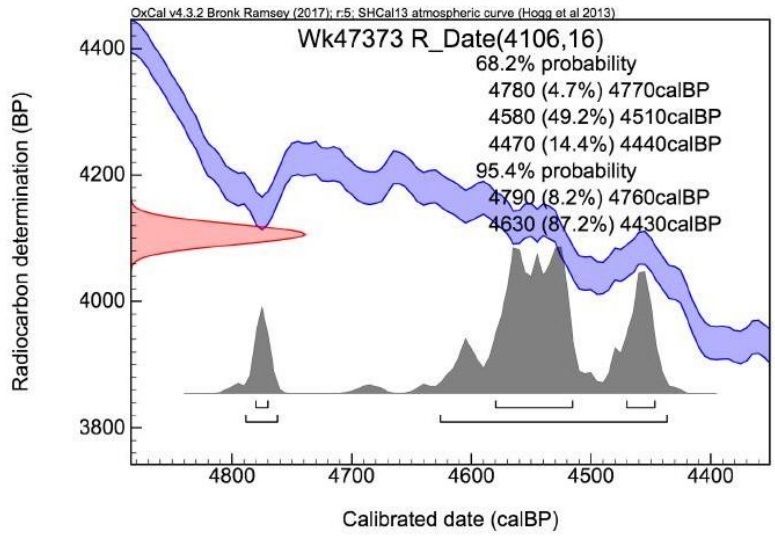

- Explanation of the calibrated Oxcal plots can be found at the Oxford Radiocarbon Accelerator Unit's calibration web pages (http://c14.arch.ox.ac.uk/embed.php?File=explanation.php)
- Result is *Conventional Age or Percent Modern Carbon (pMC)* following Stuiver and Polach, 1977, Radiocarbon 19, 355-363. This is based on the Libby half-life of 5568 yr with correction for isotopic fractionation applied. This age is normally quoted in publications and must include the appropriate error term and Wk number.
- Quoted errors are 1 standard deviation due to counting statistics multiplied by an experimentally determined Laboratory Error Multiplier.
- The isotopic fractionation, $\delta^{13}C$, is expressed as ‰ wrt PDB and is measured on sample CO_2.
- $F^{14}C$% is also known as *Percent Modern Carbon (pMC)*.

Appendix 5: Photo-mosaics of McLean's trench.

Appendix 4. Photo-mosaic images of McLean's trench walls, showing the west wall (top, camera perspective facing west) and east wall (bottom, camera perspective facing east). Some distortion of physical shape and distances in the mosaic are inherent due to the process of producing the image, so should not be used to scale.